FIU-ARC-2015-M1202-04b-011

# Development of a Two-fluid Drag Law for Clustered Particles using Direct Numerical Simulation and Validation through Experiments

Award Number: DE-FE0007260


Recipient: Florida International University

1200 SW 8$^{TH}$ ST

Sponsored Research Office MARC 430

Miami, FL, 33199-0000

DUNS #: 071298814


## Final Report

Project Period : 10/1/2011 – 12/31/2014


Principal Investigator: Seckin Gokaltun, Ph.D. (Florida International University)
Research Scientist,
gokaltun@fiu.edu, (305) 348-6340

Co-Principal Investigators: Norman Munroe, Ph.D. (Florida International University)
Shankar Subramaniam, Ph.D. (Iowa State University)


Prepared for:

U.S. Department of Energy
National Energy Technology Laboratory

March 18, 2015

# Abstract

This study presents a new drag model, based on the cohesive inter-particle forces, implemented in the MFIX code. This new drag model combines an existing standard model in MFIX with a particle-based drag model based on a switching principle. Switches between the models in the computational domain occur where strong particle-to-particle cohesion potential is detected. Three versions of the new model were obtained by using one standard drag model in each version. Later, performance of each version was compared against available experimental data for a fluidized bed, published in the literature and used extensively by other researchers for validation purposes.

In our analysis of the results, we first observed that standard models used in this research were incapable of producing closely matching results. Then, we showed for a simple case that a threshold is needed to be set on the solid volume fraction. This modification was applied to avoid non-physical results for the clustering predictions, when governing equation of the solid granular temperate was solved. Later, we used our hybrid technique and observed the capability of our approach in improving the numerical results significantly; however, improvement of the results depended on the threshold of the cohesive index, which was used in the switching procedure. Our results showed that small values of the threshold for the cohesive index could result in significant reduction of the computational error for all the versions of the proposed drag model. In addition, we redesigned an existing circulating fluidized bed (CFB) test facility in order to create validation cases for clustering regime of Geldart A type particles.

# Table of Contents

# Executive Summary

The United States of America is the world's largest energy producer, consumer, and net importer. Increased demand on imported petroleum, the ongoing deregulation of the energy industry, and environmental concerns associated with the use of fossil fuel for production of electricity and transportation fuels are all contributing to an increasing interest in better utilization not only of fossil fuels available in abundance such as coal, but also in unconventional fossil fuels such as oil shale, and tar sands.

A shortage of fossil fuels for production of gasoline by new technologies and electricity demand better utilization of these fossil fuels. Attempts to use bubbling fluidized beds with internal heat exchange tubes were not successful due to severe tube erosion problems, which were unknown before the construction of the large pilot-scale and demonstration plants. Such failures and future energy goals concerning the environment necessitate an understanding of gasification, catalytic cracking, and combustion in risers and reactors. Developers of gasifiers, combustors, chemical reactors, and owners of energy power plants are looking for more timely and cost-effective methods to predict the performance of their power generation components. Therefore, they have been incorporating simulation in their design and evaluation processes. Several computational fluid dynamics (CFD) codes have been developed to simulate the hydrodynamics, heat transfer, and chemical reactions in fluidized bed gasifiers and other power generation equipment where gas-solid flow is dominant. These computer codes are based on accepted equations governing multiphase flow; however, detailed information on gas-solids flow structure, especially identification of particle cluster size and solid concentration, is needed for validation of such CFD codes.

The validation process requires comparison with sufficient experimental data obtained through advanced diagnostics in order to identify basic criteria for gas-solid systems such as particle cluster size, concentration, and granular temperature. The research includes utilization of advanced experimental approach coupled with new mathematical and statistical analysis methods to identify particle clusters based on measurements void fraction.

The experimental work presented here involved imaging of solids concentrations using shadow particle sizing to obtain measurements of particle number density and volume fraction. The shadow sizing technique was used to simultaneously measure particle velocities and void fraction.

New mathematical analysis methods have been developed to identify criteria for particle cluster size and determine the inverse solid concentration, at which granular temperature (turbulent kinetic energy of the particles) reaches its maximum and inverses its behavior. This can be accomplished by indirectly evaluating changes in granular temperature distribution, for different particle groupings, using accepted quantitative proportionality between void fraction and granular temperature.

# Literature Review

The occurrence of particle clusters in fluidized beds has been observed since Yerushalmi *et al*. (1975) presented his hypothesis. Horio *et al*. (1988) and Hartge *et al*. (1988) detected clusters in fluidized beds. Sinclair and Jackson (1989) applied the granular flow model to a fully developed gas-solid flow. Ding and Gidaspow (1990) derived an expression for solid viscosity and pressure of a dense gas-solid flow by using the Boltzmann integral-differential equation and assuming a Maxwellian frequency distribution for the particle velocity. Gidaspow (1994) extended the formulation to both dilute and dense cases by considering a non-Maxwellian velocity distribution. Gidaspow and Huilin (1998) showed that a relation exists between pressure, temperature, and solid fraction analogous to the ideal gas law. Noymer and Glicksman (1998) addressed the effect of clusters on wall heat transfer coefficients.

Lun *et al*., (1984) and Lun and Savage (1987) presented a relationship between granular temperature and void fraction. A systematic criterion for identification of particle clusters was proposed by Soong *et al*. (1993). Brereton and Grace (1993) and Dejin *et al*. (1996) proposed intermittency and heterogeneity indexes to characterize the degree of cluster formation. Spahn *et al*., (1997) provided evidence in support of the fact that granular temperature may provide the information to establish quantitative cluster criteria. Sharma *et al*. (2000) presented the parametric effects of particle size and superficial gas velocity on the cluster duration time, occurrence frequency, and solid concentration.

The existence of solid clusters characterizes mesoscopic behavior. The cluster concept evolved as a result of the recognition of a large slip velocity between the gas and solid particles in the Circulating Fluidized Bed (CFB). Particle clusters are an indication of the heterogeneity in the mesoscale. A complete characterization of the hydrodynamics of a CFB requires the determination of the voidage and velocity profiles.

To handle complicated phenomena in the vertical pneumatic transport of solids, two theoretical approaches are proposed, namely the Eulerian and the discrete particle approaches. The Eulerian model considers the particulate phase as a continuous fluid interpenetrating and interacting with the fluid phase (Gidaspow *et al*., 1989). The kinetic theory of granular flow is used in the Eulerian model to offer a theoretical framework for simulating gas–solid flow with particles of different size and/or different density (Van Wachem *et al*., 2001a, b). However, severe difficulties are encountered: first many closure laws related to the mutual interaction of particles belonging to different classes have to be formulated; moreover, the universality of the constants used is questionable (Cao and Ahmadi, 1995).

Discrete particle models have become very useful and versatile tools in studying the dynamics of gas/particle flows. In this approach, each particle is treated by solving Lagrangian equations of motion for all the particles of the system, with a prescribed set of initial conditions. Once the flow and particle properties are known, the interface quantities between both phases can be calculated. It offers a more natural way to overcome the aforementioned problems, since each individual particle is tracked in the simulation. Moreover, it provides a powerful tool to investigate the detailed phenomena at the individual particle scale and to examine local phenomena such as particle to bed (or bed to particle) heat and mass transfers.

This approach was used to simulate gas–solid fluidization in the last decade. Phenomena such as bubbling, slugging, and solid transport in a circulating fluidized bed (CFB) can be simulated (Tsuji *et al*., 1993; Hoomans *et al*., 1996, 2001; Helland *et al*., 2000; Van Wachem *et al*., 2001a, b). Some researchers simulated flow of clusters in CFB. Tanaka and Tsuji (1991) investigated the cluster formation in a vertical riser and the particle-induced instability in gas–solid flows. They showed that particle–particle interactions play an important role in cluster formation and cause flow instabilities even when the mean concentration is about 0.5%. Tanaka and Tsuji (1991) observed that change of conditions, such as gas velocity decrease and particle loading increase, result in instability and inhomogeneity. Later, The Direct Simulation Monte Carlo model (DSMC) was used by Ito *et al*. (1998) to simulate the dynamics of clusters. The individual particle behavior can only be obtained statistically, because particle collisions are described from statistics. Ouyang and Li (1999) developed a particle-motion-resolved discrete model to simulate heterogeneous structure in gas–solid fluidization. Helland *et al*. (2000) studied the cluster formation in gas-particle CFB. They studied the influence of porosity and observed a large difference in the local flow as a function of porosity.

To simulate the cluster formation, several researchers (Ito *et al*., 1998; Helland *et al*., 2000) considered that the particles were distributed uniformly in the riser as an initial condition. This assumption is not realistic for predicting the cluster formation in CFB. In the particle-motion-resolved discrete model (Ouyang and Li, 1999), the interactions forces between particle and fluid, and vice versa, were considered separately, which does not obey Newton's third law. Zhou *et al*. (2002) emphasized the influence of particle properties, porosity function, and velocity on the global particle flow structure. They investigated the same effect on formation and development of local regions of higher particle concentration, i.e., particle clusters.

The TFM approach, developed by van Deemter and van der Laan (1961), is known as an economic way of simulating multiphase flows in large-scale fluidized bed risers (Pannala et al., 2010). Formulating the solid and gas as continuous phases is the principle of the TFM method. This leads to significant reduction of memory and computational costs as compared to other widely exploited methods, such as the Particle-Resolved Direct Numerical Simulation (Hu et al., 2001 and Nomura and Hughes, 1992), Discrete Element Method (Tsuji et al. 1993 and Mikami et al 1998), and structure-based methods, such as the Discrete Bubble Model (Bokkers et al. 2006), and the Discrete Cluster Model (Liu et al., 2006 and Zou et al. 2008). One notable drawback of the TFM in MFIX is the absence of cohesive inter-particular forces, such as electrostatic and van der Waals forces between particles. These forces play a major role in fluidization of strongly cohesive particles in Geldart A and C groups by creating heterogeneous structures, called clusters. According to Li et al. (2013), clusters affect the flow significantly by changing the mass and momentum transfers between the gas and solid phases. Many researchers, such as Agrawal et al. (2001), Zhang and Vanderheyden (2002), McKeen and Pugsley (2003), Yang et al. (2003, 2004), Ye et al. (2005a,b, 2008), Qi et al. (2007), Wang et al. (2007-2009), Lu et al. (2009), Igci et al. (2012), and Li et al. (2013), believe that clusters are responsible for significant reduction of the interfacial drag forces between the gas and solid phases. Therefore, dependency of the drag forces on the nature of the attractive interparticle forces plays as important a role as the dependency on two other parameters, i.e., the Reynolds number of the flow around particles and the volume fraction of the solid phase in each computational cell.

There have been several attempts to improve the performance of the MFIX-TFM code by introducing more complex drag laws, which can consider the effect of subgrid-scale heterogeneous structures in TFM simulations, such as the filtered models of Igci et al. (2011) and Milioli et al. (2013); however, the constitutive models used in these filtered models were obtained from highly resolved simulations of kinetic theory-based TFM simulations in the absence of the cohesive interparticle forces. This gap can be filled by inclusion of cohesive interparticle forces in the MFIX-TFM code, similar to the contribution of Weber (2004) in inclusion of van der Waals in the MFIX-DEM code (MFIX-2013 Release Notes). In addition, no study has been found in the literature that has implemented the inclusion of the van der Waals forces in the drag laws within the MFIX-TFM code.

DNS has been widely used in high resolution simulation of gas-particle flows in suspension and fluidized beds by researchers such as Ma et al. (2006), Cho et al. (2005), Xiong et al (2012), and Yin and Sundaresan (2009). Ma et al. (2006) acknowledged the diversity and structural dependence of the drag force on each particle, rather than relying on the entire control volume performed in methods such as TFM. Their analysis, akin to DNS analysis of Xiong et al (2012), proved that the drag force is significantly different on particles in dilute regions compared to grouped particles.

One useful approach in DNS modeling is the analysis of the flow over fixed assemblies of particles, as practiced by Hill et al. (2001a,b), van der Hoef et al. (2005), Beetstra et al. (2007), Yin and Sundaresan (2009), and Tenneti and Subramaniam (2011). This approach increases the accuracy and relevance of the information collected. For example, information about field variables, such as the coefficient of drag, and gas and particle velocities can be obtained. Additionally, various different cluster configurations could be analyzed. Cluster differences include: shape, compactness, orientation of the cluster relative to the fluid, spinning speed of the cluster, and various flow-solid relative velocities. A combined particle or cluster resolved DNS analysis coupled with the TFM analysis of the flow could contribute to the improvement of the TFM modeling of the clustering multiphase flow systems. There is also an opportunity for a simulation of the flow on the industrial-scale, using the information obtained in particle or cluster-scale.

Presently, MFIX is a widely known, reliable, and professionally established package for simulation of heat and mass transfer. MFIX accommodates a variety of drag models that can be used in TFM simulation of gas-solid particulate flows. Yet, the direct or indirect addition of models for particle-to-particle attractive forces to the transport equations solved in TFM, or to the available drag laws, is missing. According to Ye et al. (2005 a,b) and Seville et al. (2000), the attractive force could be formulated as $\vec{F}_{ij}^{(c)} = (AR/6d_{ij}^2)\,\vec{n}_{ij}$, where $F_{ij}^{(c)}$ is the cohesive inter-particular force and A is the Hamaker constant ($\approx 10^{-19}$ J) (Israelachvili, 1991), R is the radius of the monodisperesed particles, d is the surface to surface distance between particles and $\vec{\boldsymbol{n}}$ is the normal vector pointing from the center of particles i to the center of the particle j. Further, they defined a scaling factor, $\varphi = \dfrac{|U_{min}|}{K_B\,T} = \dfrac{A\,R}{6\,z_0} \cdot \dfrac{1}{K_B\,\Theta_S}$, to find the ration between interparticle cohesive and destabilizing forces for $d \le 100$ μm. In this definition, $K_B$ is the Boltzmann constant ($K_B \approx 1$, Ye et al., 2005a), $Z_0$ is the threshold for particles to be considered as clustered ($Z_0 \approx 4$ nm, Seville et al., 2000) and, d and $\Theta_s$ are the diameter and granular temperature of the solid particles. The derivation of the equations governing the particle motion can produce a similar quantifying scaling factor, which can indicate the onset of cluster formation. In this analysis, as compared to the cohesion models available in the MFIX-DEM, the scaling factor is an additional factor to be considered for cluster formation, (in addition to the surface to surface particle distances).

Destabilizing forces in the particle-gas systems are mainly due to the particle-to-particle and particle-to-gas interactions. These interactions significantly influence the analysis of particle-gas flows, which has attracted the attention of many researchers, such as Dombrowski and Johns (1963), Gidaspow (1994), Ding and Gidaspow (1994), Cho et al. (2005), Benyahiah (2012), Karimipour and Pugsley (2012), and Syamlal et al.(2013). Special attention has been paid to this parameter in the work of Yet et al. (2005-a). The granular temperature is a measure of the particle fluctuating energy and could be used as a critical parameter to predict the coalescence of particles and break-up of clusters in numerical simulations. MFIX-TFM can solve the transport equation or the algebraic equation, in order to obtain the granular temperature.

In this study, we introduced a cohesive index into the MFIX-TFM code and implemented it as a criterion for switching between a Particle-Resolved Direct Numerical-Simulation model, the TGS model, and three existing drag models available in the MFIX code. Later, extensive DNS simulations were performed in specific solid volume fraction of the solid and for Reynolds number in the range of 0 to 60. The purpose of these simulations was to establish a dependency between the air-solid drag force and the cohesiveness of the particles. Eventually a drag function was introduced for clustered particles based on modifications to the uniform drag law. The rest of this report is organized as follows. First, modifications to the ARC-CFB and newly designed test facilities are explained. This embraces new solid feed mechanism, installation of equipment (different types of transducers, flow meter, thermometer, pressure gauge, safety valve, and end-line filtration drum), characterization tests of FCC powder, fabrication of a bubbling test setup, image processing, and data acquisition tools. Secondly, the formulations of the models are presented. This embraces the governing equations for the TFM model, the governing equations related to the model of motion of particles leading to our cohesive index, and the governing equations of the Gidaspow, Syam-O'Brien, Wen-Yu and TGS drag models. Later, the methodologies for implementation of the cohesive index, error calculations, and examination of the proposed models in numerical simulations of a fluidization flow are presented. Finally, a conclusion is drawn on the effectiveness of the proposed model and the authors' perspective of the future work.

# Experimental Set-up

## Fluidization solids

Geldart A particles was used in this project in order to investigate the cluster formations during fluidization and to formulate a drag correlation that is accurate in the case of particle clustering. These particles have a mean diameter in the range of $\bar{d}_p = 50 - 100\ \mu m$ and a low solid density ($\rho_s \leq 1500\ kg/m^3$). Geldart A particles fluidize easily and provide a homogeneous bed expansion. Fluid Catalytic Cracking (FCC) catalysts fall into this category which was used in the current study. The mean diameter of FCC particles is $\bar{d}_p = 80\ \mu m$ with solid density of $\rho_s = 1500$ kg/m$^3$.

The flow regime obtained by fluidizing the FCC particles at various superficial velocities can be estimated using the flow regime map, as given in Figure 1. Figure 1 categorizes the flow regimes in terms of a dimensionless particle size, $d_p^*$, and a dimensionless gas velocity, $u^*$, that are defined as (Kunii & Levenspiel, 1991):

$$d_p^* = d_p \left[ \frac{\rho_g \left(\rho_s - \rho_g\right) g}{\mu^2} \right]^{1/3}, \qquad \textbf{Equation 1}$$

$$u^* = u \left[ \frac{\rho_g}{\mu \left(\rho_s - \rho_g\right) g} \right]^{1/3}. \qquad \textbf{Equation 2}$$

The dimensionless particle diameter for FCC catalysts is found to be $d_p^*=3$ (Eq. 1), for which we obtain a minimum fluidization velocity of $u_{mf}=2.86\times10^{-3}$-$7.15\times10^{-3}$ m/s, a minimum bubbling velocity of $u_{mb}=5.72\times10^{-2}$-$6.87\times10^{-1}$ m/s, and a fast fluidization velocity of $u_f=1.15$-$4.5$ m/s.

FIU obtained a drum of spent FCC catalysts shown is Figure 2, from a vendor called Equilibrium Catalysts Inc. The company donated the material for free and FIU paid for the freight shipping. The MSDS sheet for the particles is provided in the Appendix A of this report.

## Particle size distribution analysis

FIU received a 5 kg sample of fresh FCC particles from the BASF® Corporation. A non-disclosure agreement was pending for 6 months to be signed by FIU and BASF in order to receive these particles. A sieving mechanism shown in Figure 3(a) was used to obtain the particle size distribution of the FCC catalysts powder. The results of this characterization test were useful in setting the mean diameter of particles in our simulations using MFIX. We repeated the sieving analysis for three samples of different weight and each for three times. According to the results, as shown in Figure 3(b and c), the mean diameter of for our FFC particle sample was 79.03 µm.

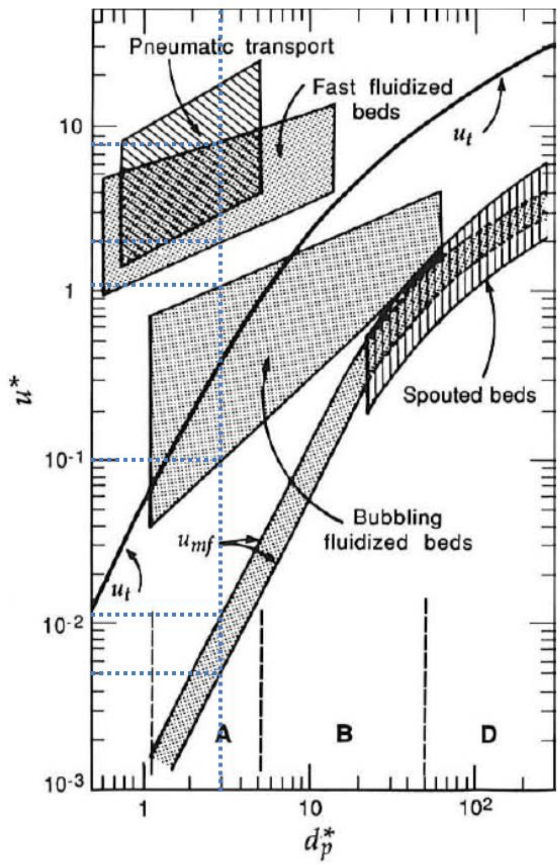


**Figure 1 . Flow regime map of gas/solid contacting (Kunii & Levenspiel, 1991)**

**Figure 2.  Spent FCC catalyst drum received at FIU**

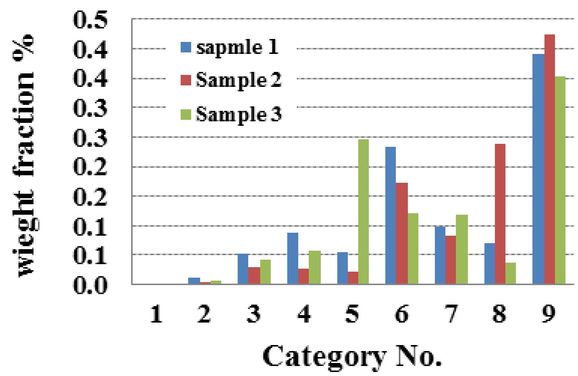


| cat# 1 : | cat# 2 : | cat# 3 : | cat# 4 : | cat# 5 : | unit |
|---|---|---|---|---|---|
| 0-20 | 20-32 | 32-45 | 45-53 | 53-63 | µm |

| cat# 6 : | cat# 7 : | cat# 8 : | cat# 9 : | unit |
|---|---|---|---|---|
| 63-75 | 75-90 | 90-106 | 106-125 | µm |

(a)

(b)

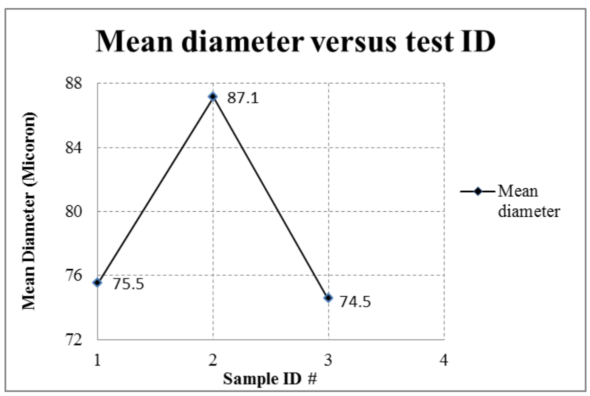


(c)

**Figure 3. Result of size analysis for the FCC catalyst**

## Power requirement

The power requirement of the compressor that was used to fluidize the particles in the riser was estimated by calculating the pressure required at the inlet section of the riser section, $P_1$:

$$P_1=\Delta P_b+\Delta P_d \qquad \textbf{Equation 3}$$

Where, $\Delta P_b$ and $\Delta P_d$ were the pressure drops across the bed and the distributor respectively. The distributor pressure drop was related to the pressure drop across the bed via $\Delta P_d=(0.2\text{-}0.4)\Delta P_b$ (Kunii & Levenspiel, 1991) and the pressure drop in the bed was calculated as:

$$\Delta P_b = L_m(1-\varepsilon_m)\left(\rho_s-\rho_g\right)g. \qquad \textbf{Equation 4}$$

For a fixed bed length of $L_m = 1m$ and void fraction of $\varepsilon_m = 0.45$, our calculation stated that the pressure at the inlet section for minimum fluidization should be $P_1 = 111.5\ kPa$. At fast fluidization regime this value was calculated to be 1.1 – 1.2 times larger. The compressor power required to attain this pressure was obtained by

$$-\dot{\omega}_s = \frac{\gamma}{\gamma-1}\frac{P_1 v_1}{\eta}\left[1-\left(\frac{P_0}{P_1}\right)^{\frac{\gamma-1}{\gamma}}\right]. \qquad \textbf{Equation 5}$$

Where, $\gamma = 1.4$, $v_1$ is the flow rate of air, $P_0$=101 kPa is the ambient pressure and $\eta$ is the compressor efficiency. For a 0.75 efficient compressor at the given flow conditions the maximum power requirement is estimated to be 1.2 kW.

## Distributor plate

One of the most important aspects of the design modifications to consider for the fluidized bed at FIU was to identify an appropriate distributor plate. The role of the distributed plate was to provide a uniform gas flow at the inlet of the riser. In the previous CFB facility at FIU, no distributor plate was used, since the particles, which were collected at the stand pipe, were being injected into the air stream vertically at a cross-flow configuration through a mechanical rotary valve.

In order to obtain a dense flow fluidization, the existing design was modified by placing a perforated plate type distributor at the bottom of the transparent riser section. At this location of the system, the compressed air was pumped into the system and solids were inputted using an L-valve design.

Perforated plate distributors were cheap and easy to fabricate and could provide even distribution of air flow through the orifices if designed properly. It was also easier to incorporate in a computational fluid dynamics model due to its simple geometry. According to the orifice theory, the fraction of open area in the distributor plate could be estimated using the Reynolds number, $Re=d_t u_o \rho_g/\mu$, which was found to vary in the range of 29 – 46,000 for the velocity values in regimes of the flow, ranging from minimum fluidization to fast fluidization. Using the corresponding orifice coefficient $C_{d,or}$ (=0.6 for Re>3000), the gas velocity at the orifice was found by

$$u_{or} = C_{d,or}\left(\frac{2\Delta p_d}{\rho_g}\right)^{0.5}. \qquad \textbf{Equation 6}$$

The orifice velocity varied in the range of 38.4 – 43.5 m/s and the corresponding $u_o/u_{or}$ varied between 0.007 % to 11.9 %. In order to achieve the pressure drop across the distributor for uniform fluidization the combination of orifice diameter, $d_{or}$, and number of orifices per unit area $N_{or}$ must be known. For the case presented in this study, a perforated plate distributor with $d_{or}$=2 mm and $N_{or}$=37962 $m^{-2}$ (692 orifices) could satisfy the design criteria in the fast fluidization regime.

A porous plate manufactured by Mott Corporation was selected for use as the distributor plate. The porous plate was received in the form of a 10” by 10” rolled stainless-steel sheet of 0.078” thickness which was cut into a circular form using a CNC machine and sandwiched between two plastic flanges as shown in Figure 4(a). The corresponding plenum region is also shown in Figure 4(b), where the connection to the plate was achieved through a flange.

(a) (b)

**Figure 4. Distributor plate and the inlet plenum designed at FIU**

The media grade of the porous plate was 40 which retained 99.9% of particles with diameter 45 µm or larger. This number reduces to 99% for particle diameter of 25 µm and 90% for 12 µm, when tested at a flux of 6 acfm/$ft^2$. The yield strength of the plate was 3.5 kpsi, which was high enough to sustain the weight of the particles in the riser. The pressure drop across the porous plate was calculated to vary in 0.912 - 3.648 psi for a flow rate range of 44.2 – 176.8 cfm.

In addition to the porous plate, Figure 5 shows two screens of 20 and 25 microns of pore size donated by Johnson Screens Inc. for testing purposes. This provision allowed a comparative study of distributor plate effects on uniform fluidization.

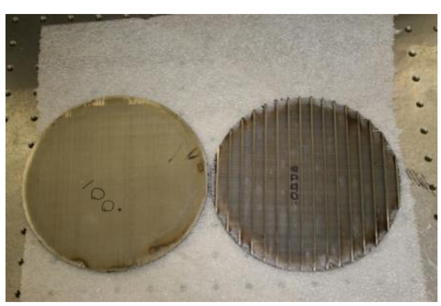

**Figure 5. Screens provided by Johnson Screens Inc**

## Air compressor/blower

The pressure requirement for the air compressor that was used to fluidize the particles in the riser was estimated by calculating the pressure required at the inlet section of the riser section for a fixed bed length of $L_m = 1m$ and void fraction of $\varepsilon_m = 0.45$. Our calculation resulted in a value of 111.5 kPa for minimum fluidization. in the fast fluidization regime, this value was 1.1 – 1.2 times larger. The flow rate required to achieve fast fluidization in the 6”-diameter riser was estimated to be in the range of 44 – 177 cfm.

FIU received a roots blower package from Dresser Industries Inc., as shown in Figure 6(a). The system included a Roots 45-URAI blower driven at 2000 rpm by a 15-hp, 1800-rpm, three-phase electric motor with adjustable motor base, 4” inlet, discharge silencers, safety guard, pressure relief valve, pressure gauge, and a table. The URAI blower performance and the schematic portray are shown in (Appendix A) for varying operating pressures.

**(a)** **(b)**

**Figure 6. Roots blower and control unit at FIU. (a) Roots blower (b) Variable Frequency Drive unit**

## Solids feeding mechanism

First, the mechanical rotary (shown in Figure 2) was replaced with an aerated L-valve configuration as shown in Figure 7. The mass flow into the riser was controlled by adjusting the air flow into the horizontal section of the L-valve.

During various conversations with Ray Cocco at PSRI and Larry Shadle at NETL, it was mentioned that the non-mechanical valves such as the L-valve configuration could work best with the particles that fall in the Geldart Groups B and D. Geldart A particles do not work well with L-valves since they defluidize relatively later compared to Geldart B and D particles which makes it difficult them to control (Knowlton, 1997). Therefore, an angled standpipe with a slide gate valve configuration was used in the current application, as recommended by PSRI. Figure 7 shows the completed CFB test facility at FIU. This system includes a 4” PVC 45° angled down comer with a slide gate valve configuration, that were manufactured at FIU. We added to this system a Wye pipe to provide access, in case the retrieval of the particles was necessary.

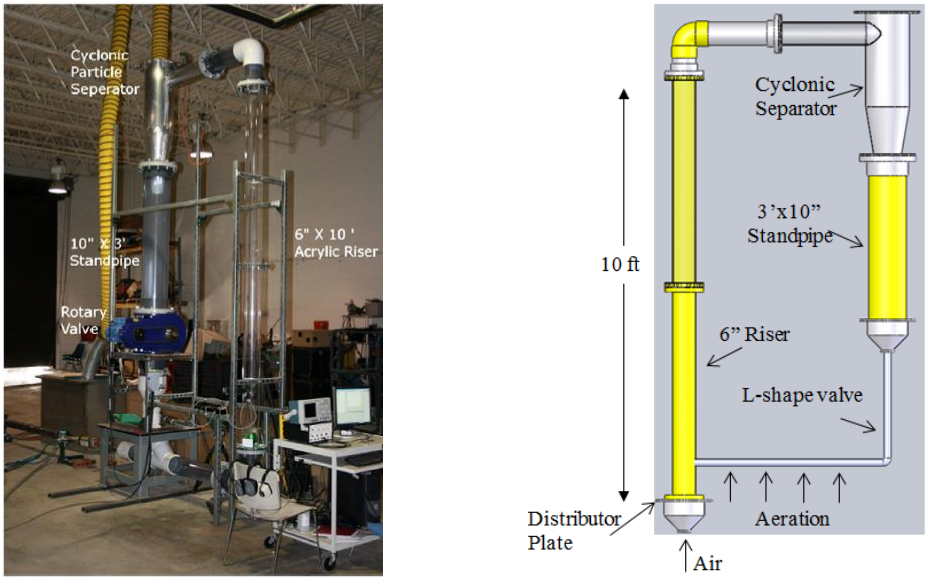


**Figure 7. Schematic of the CFB design with Rotary valve (on left) and L-shape valve (on right) at FIU-ARC**

## Addition of air flow meter to the CFB

Equation 2 was used to find the ranges for the dimensionless velocities, $u^*_{mf}$, $u^*_{mb}$, and $u^*_{f,}$ which are the minimum fluidization, minimum bubbling and the fast fluidization velocities, respectively. Table 1 shows our calculation of the pressure drop and required flow rate to fluidized a one-meter column of the FCC in the ARC-CFB facility.


**Figure 8. Completed solid feeding mechanism in the circulating fluidized bed set-up at FIU**

**Table 1 Calculation of the pressure drop in the CFB.**

| Reference parameters | | | | | |
|---|---|---|---|---|---|
| **d_p (m)** | **rho_p (kg/m3)** | **rho_g (kg/m3)** | **mu_g (kg/m.s)** | **d_riser (in)** | **d_p*** |
| 8.00E-05 | 1500.00 | 1.19 | 1.79E-05 | 6.00 | 3.03 |
| **efficiency** | **gamma** | **P0 (kPa)** | | | |
| **0.75** | 1.40 | 101.00 | | | |
| Flow rate calculations | | | | | |
| **u*_mf1** | **u*_mf2** | **u*_mb1** | **u*_mb2** | **u*_f1** | **u*_f2** |
| 0.01 | 0.01 | 0.10 | 1.20 | 2.00 | 8.00 |
| **u_mf1 (m/s)** | **u_mf2** | **u_mb1** | **u_mb2** | **u_f1** | **u_f2** |
| 0.00 | 0.01 | 0.06 | 0.69 | 1.14 | 4.58 |
| **Q_mf1 (m3/s)** | **Q_mf2 (m3/s)** | **Q_mb1 (m3/s)** | **Q_mb2 (m3/s)** | **Q_f1 (m3/s)** | **Q_f2 (m3/s)** |
| 0.00 | 0.00 | 0.00 | 0.01 | 0.02 | 0.08 |

| Pressure drop calculation | | | | | | |
|---|---|---|---|---|---|---|
| **Lm (m)** | **epsilon_m** | **delP_b (kPa)** | **delP_d (kPa)** | **P_1 (kPa)** | **P_1 (psi)** | **P_1f (psi)** |
| 1.00 | 0.45 | 8.09 | 2.43 | 111.51 | 16.17 | **19.41** |

The performance chart of the Blower (Figure 9) guided us to understand that the blower could provide 0.08 $m^3/s$ (177 scfm) air flow, at the maxim speed of 2000 rpm and at the expense of 10 psi pressure rise. Therefore considering the maximum safe pressure rise of 10 psi at the blower, an Omega® Fl45230A rotameter and a pressure relief valve, as recommended by the Dresser Industries Inc., were added to the system (Figure 10).

## Completion of the CFB at FIU

Eventually, the CFB experimental facility at the FIU-ARC was completed by regulating the weights on the pressure relief valve (Figure 11-a), purchase and installation of the safety cage on the fork lifts (Figure 11-b) and repair of the electric lift, installation of the wiring for pressure transducer and thermocouple (Figure 11-c), completion of the collection drum and filters (Figure 11-d,e), and filling the CFB inventory with FCC material (Figure 11-f).

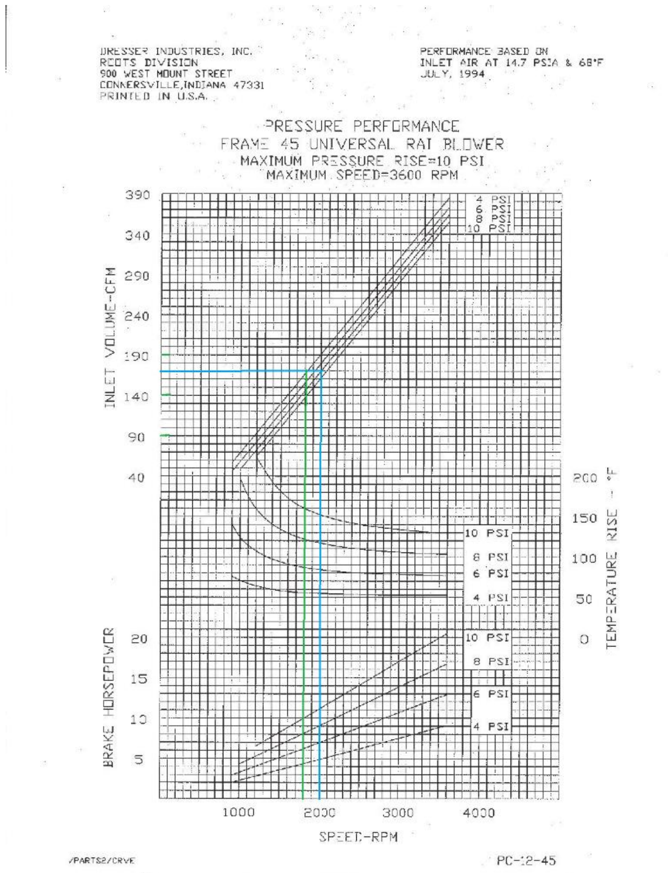


**Figure 9. Performance chart of the blower at FIU**

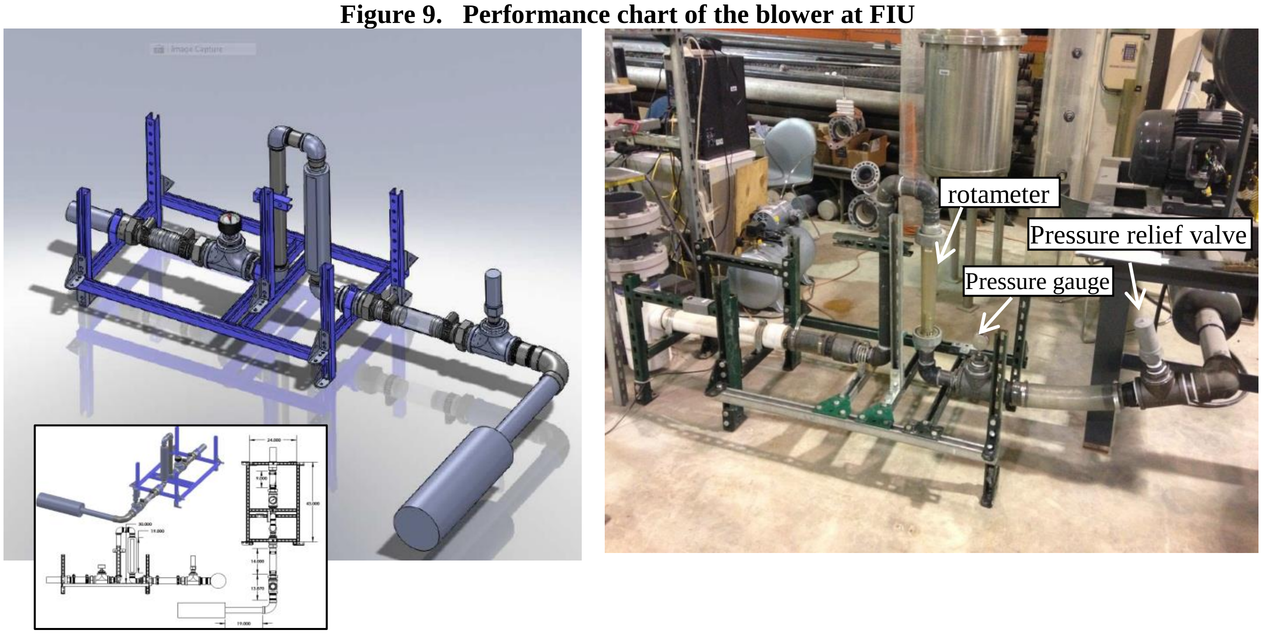


**Figure 10. Schematic and manufactured portray of the completed air supply line of the CFB at FIU**


**Figure 11. Schematic and manufactured portray of the completed air supply line of the CFB at FIU**

## Design of a bubbling bed set-up

A bubbling fluidized bed set up was designed in order to conduct imaging experiments with the existing polystyrene and FCC particles. The purpose of this effort was to obtain large number of images of particle configurations that could be used to establish a method to create the particle cluster configurations. These reconstructed configurations could be used by the collaborators to obtain drag coefficients around clusters in their direct numerical simulations. Figure 12(a and b) and Figure 13(a-c) show the initial design, final design, and the manufactured configurations, respectively.

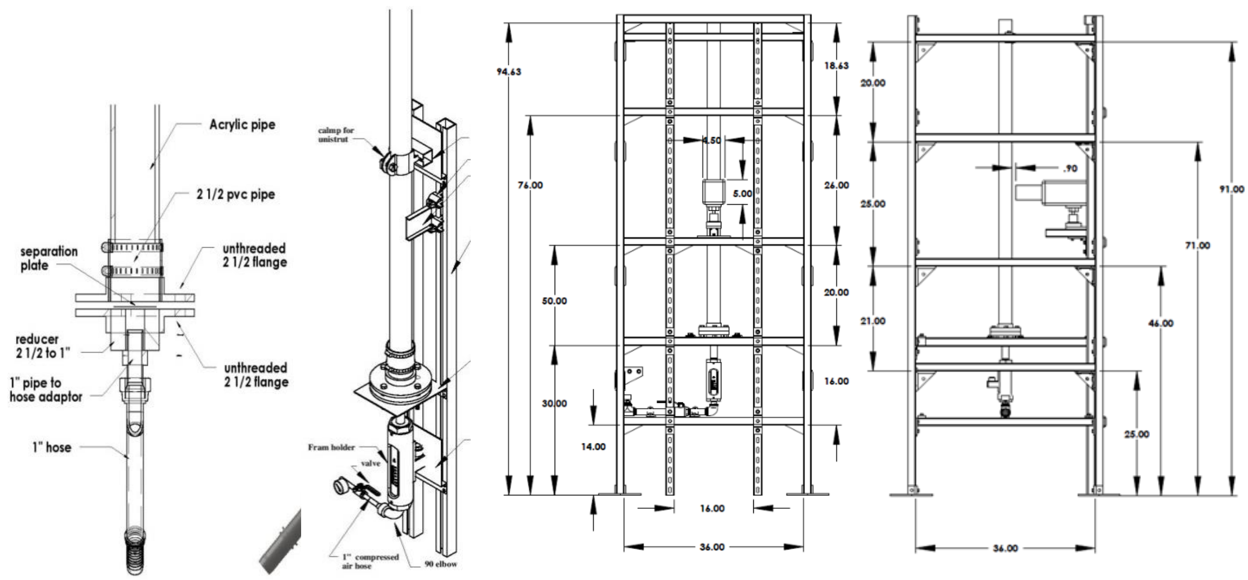


(a) (b)

**Figure 12. Bubbling bed design at FIU, (a) Initial design and (b) Final design.**

(a) (b) (c)

**Figure 13. Bubbling bed design at FIU, design of supply line (a), manufactured test rig (b), and installed supply line(c)**

Two rotameter models, OMEGA® FL-1705 with measurement range of 0.022 to 0.22 SCFM, and 5P347 KEY INSTRUMENTS® with the measurement range of 20-200 SCFH, were used for our fast and bubbling fluidization tests in the bubbling test set up, respectively.

### Filtration of entrained particles in the bubbling bed set-up

Entrainment of particles during utilization of the bubbling bed was carefully considered in this project. A high duty filter with capability of trapping particles as small as 4 microns, with 95 percent reliability, was used. This filter, shown in Figure 14, was found to be very durable and resistant to outside-high-pressure, which enabled us to apply of higher air flow rate and air pressure with the minimum leak of particulate to the ambient.

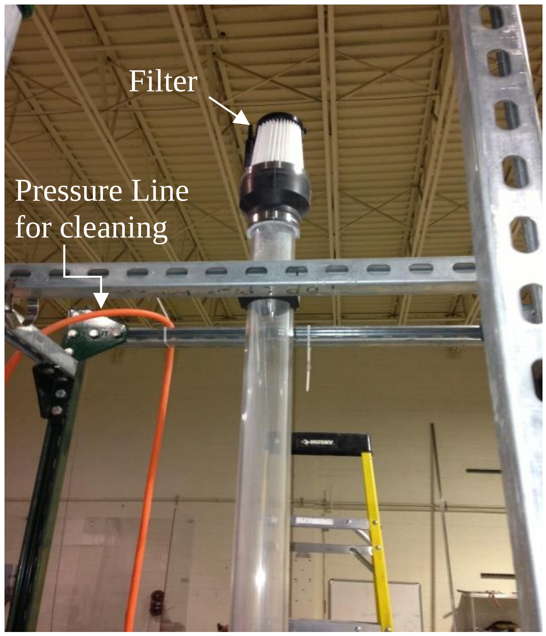


**Figure 14. Replacement of the filtering vacuum bag with a high performance filter, vacuum bag is shown on the left and high performance filter is shown on the right**

## Electrostatic charge reduction

Presence of electrostatic charge in the riser section was one of the main issues with our fluidization experiments. These static charges cause particle-to-wall and particle-to-particle sticking effect. Elimination of the particles covering the interior pipe surface was vital in improving the imaging quality.

Static charge effects that were problematic in the experiments with the polystyrene material were eliminated by spraying an agent, Fresh Cent®, inside the riser before conducting the fluidization experiments; however, this approach was found impractical for the FCC material since formations of stable sticky-paste-like structures were observed. A combination of three solutions existed in the literature to fully discharge the systems from the electro static charges, i.e., grounding the system, maintaining humidity of the system in the range of 40 to 60 percent, and introduction of static guard agents. These options were considered for the bubbling set up carefully. Unfortunately, grounding couldn't eliminate the charges in the moderate to densely solid-packed regions of the bed. Steam injection was introduced into the bed using two pressurized injection systems, i.e., a manually-controlled pulsative method shown in Fig. 13(a) and a continuous method shown in Figure 15(b-c). In these systems, we initially used the Fresh

Cent® agent in our injection procedure which was found to have very short lasting effect on the removal of the electrostatic charges. Later, we used the Larostat 264A agent which was found to condensate with a significantly higher viscosity in comparison to the Fresh Cent® agent and caused clogging in the one-way valve and associated back-leak of the material into the injection lines. This problem was later postponed using a relief mechanism which was hand-controlled using a bulb-valve in one point in the system.

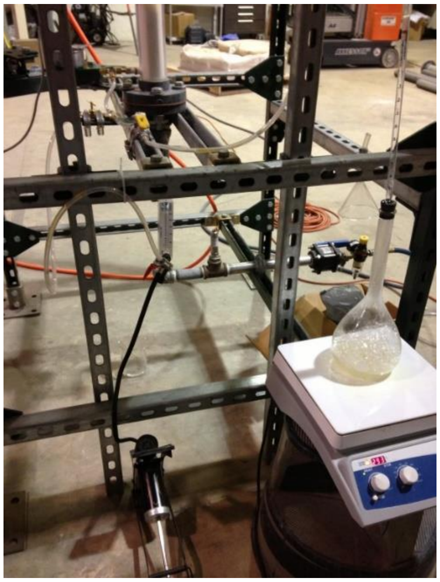

(a)

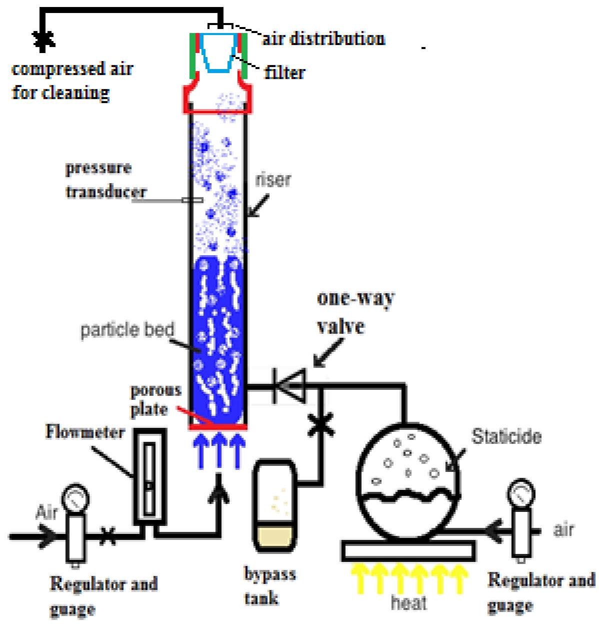


(b)

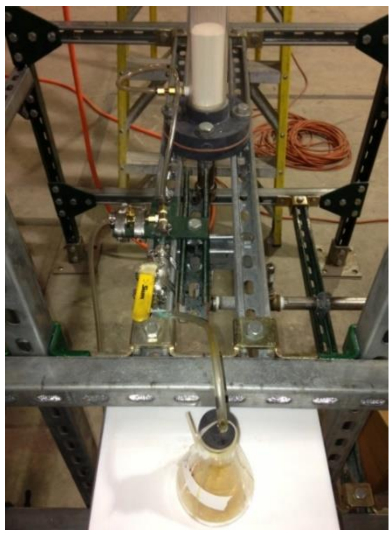

(c)

**Figure 15. Pressurized steam injection mechanisms, (a) intermittent, (b & c) continuous steam injection mechanism**

## Data acquisition

### Verification test for Field Point 2010 data acquisition unit

In order to check the precision of measurement by the available Field point AI data acquisition modules, a series of tests were performed. In this experiment a source of current was generated using the Omega CL-303 4-20 mA, a regulator type current generator, as shown in Figure 16(a). The readings from the data acquisition unit, shown by DAQ in the Figure 16(b) were then compared to the readings of the multimeter Agilent U12252.


(a) (b)

**Figure 16. Illustration of tests performed for channel check up**

Through this test, we found out that FP AI 111 module responded to the test perfectly in all its channels. This module showed to have 16 perfectly-working channels enough for support of all pressure transducers in the fluidized bed experiment. The error generated with this module was less than 0.1 percent on all its channels. However, this module stopped to connection to the main data processing module and we repeated this test for other available modules shown as "FP AI 100-2" and "FP AI 100-3" shown in Figure 16(b). Our results are available in the Appendix of this report and show that two modules FP AI 100-2 and FP AI 100-3 were used together to provide us with 15 working channel which generate less than 0.1 percent error in measurement in each channel.

### Velocity profile measurement above the separation plate (Pitot tube test)

Initially we decided to implement a precise inlet boundary condition for the air phase in our MFIX simulation, which was based on the inlet velocity of the incoming air instead of the mass flow rate. For this purpose the inlet section of the circulating fluidized bed was dismantled to measure the velocity profile over the separation plate. The measurements were performed at different heights and blower speeds. Initially the test standards of the manufacturer of the pitot tube (Dayer Instruments Inc.) was followed and relevant calibration plates were manufactured to mark 13 points on the guide roller (Figure 17); however, more points were added afterwards for higher resolution. The data received from the pitot tube was processed via the EXTECH manometer and converted into the dynamic pressure. The density calculation was later done through a program created in the Labview© VI version 8.5, which retrieved the static pressure (from a PX209 type transducers) and the temperature (from a T-Type thermocouple) in the downstream of the flow obtained from the Field Point© 2010 data acquisition unit. Figure 16 shows the results of our measurements in three different speeds and at four elevations above the separation plate in axial direction and 13 radial locations. These results show that increase of velocity can smoothen the profile in the middle radial locations and spikes are present in radial locations close to the pipe wall. Appendix A shows the verification-test results for the pressure transducer and the thermocouple used in this measurement. Figure 18 shows the result of velocity profile measurement at different speeds, positions and heights above the separation plate.

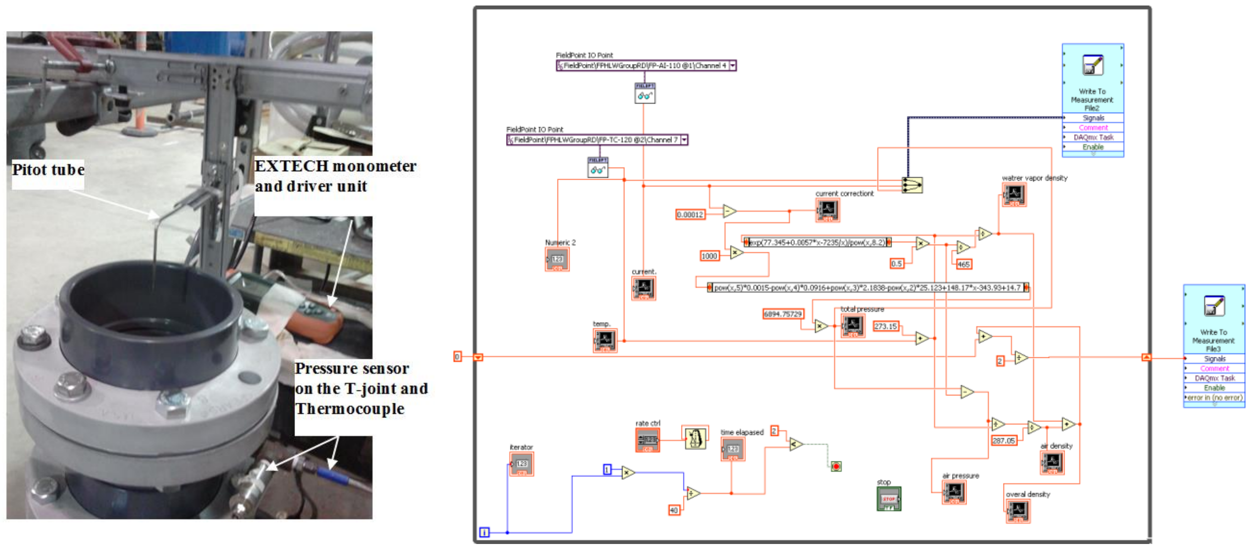


(a) (b)

**Figure 17. Pitot tube experiment, (a) setup and (b) Labview© VI version 8.5 for data processing**

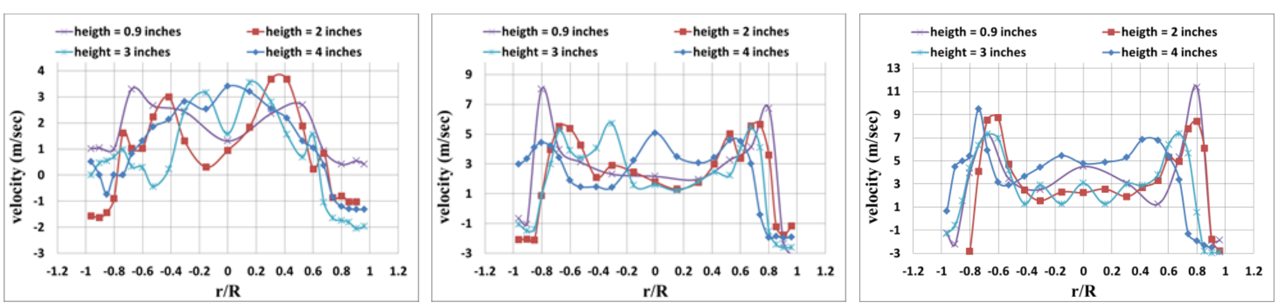


(a) (b) (c)

**Figure 18. Profile of the velocity at different heights above the separation plate , (a) 500 rpm, (b) 1000 rpm, and (c)1400 rpm**

## Riser pressure profile measurement

For this study, initially available PX209-type transducers from Omega Engineering Inc. were used with a range of -14.7 to 135 psi and a typical response time of 2 second. National Instruments FieldPoint data acquisition system was used for simultaneous recording of pressure along the test bed. The results of our verification tests for 15 transducers are available in the appendix of this report. In addition, a Labview© 8.5 VI program was designed to implement curve fitting and current-to-pressure conversion (Appendix A). These results showed that even though the curve fitting and conversion was perfectly performed through the Labview program, the transducers produced tremendous deviations from the factory data, which could be associated to damage for small-range transducers or due to loss of sensitivity and precision in bottom range of large-range-transducers. Accordingly, the use of these transducers wasn't acceptable for extremely small pressure changes, such that has happened in the minimum and bubbling fluidization experiments in both the bubbling and CFB test facilities at FIU.

Figure 19 shows Labview© 8.5 VI program used to visualize the measurement at different locations in our CFB facility.

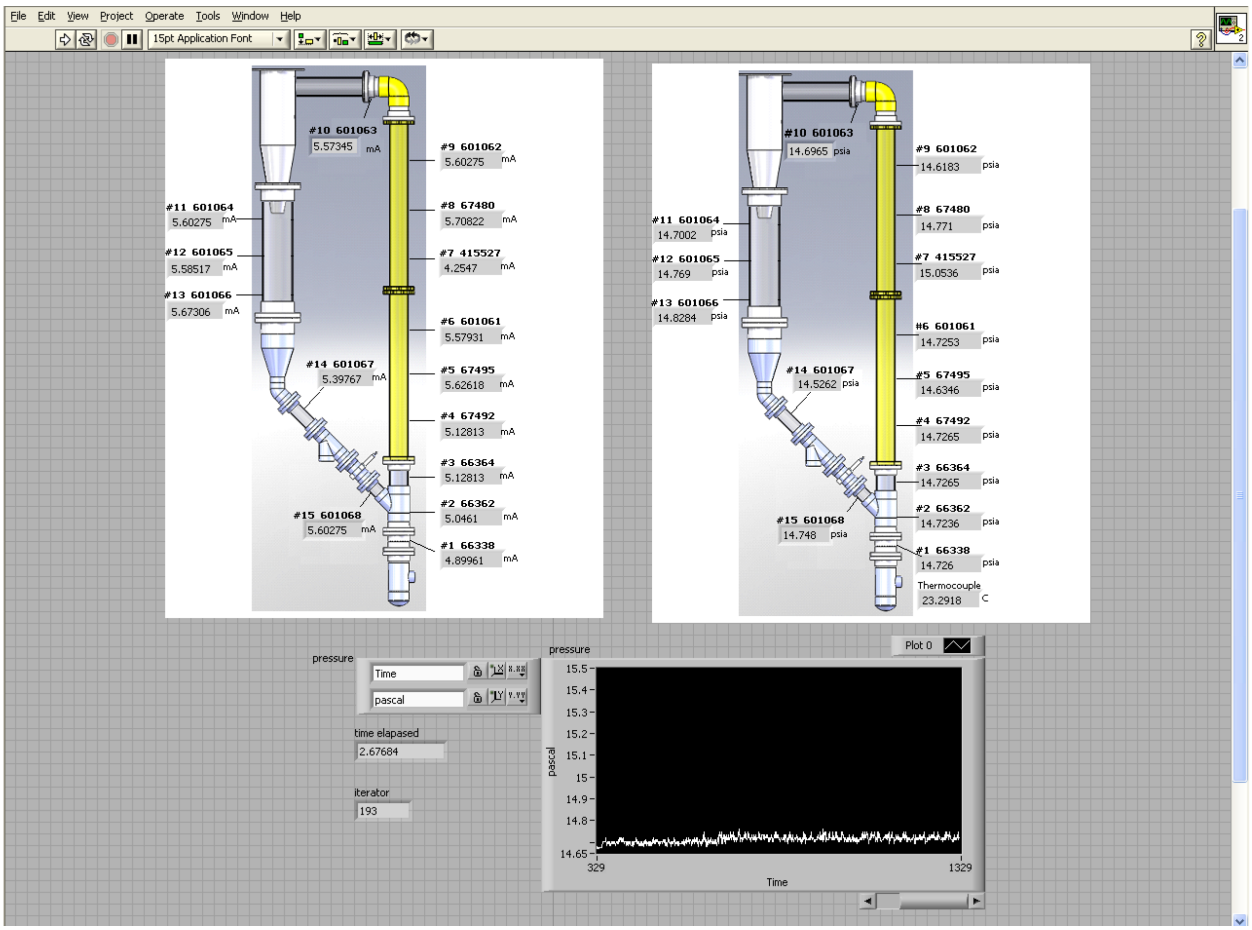


**Figure 19. Schematic diagram of the designed VI for the CFB, real time current and pressure readings at each measurement station, a chart with history of pressure change for one of the transducers.**

## Determination of appropriate pressure transducers for the CFB at FIU

We classified the working condition inside the CFB at FIU as steady and non-steady conditions. In steady tests, the air and solid influx to the system was set on fixed values through the VFD and opening of the solid sliding valve. Through this control mechanism the system could be working in fast, turbulent, and pneumatic transport states. Under unsteady conditions, controlling mechanisms of the air and solid varied the speed of the blower and/or the opening of the solid sliding valve. In addition, the working conditions could vary drastically with the initial height of the static bed in the riser.

In our tests by using one meter of the FCC column in the riser and an available 0 to 5 psi factory-certified pressure gauge, we ensured that the working pressure of the system was below 2.5 psi. Under such conditions, utilization of existing heavy duty pressure transducers, which were in range of 0-100 psig or 0-135 psig resulted in huge measurement errors. Therefore we purchased two Omega© 0-5psig pressure transducers of PX319-din-connection type. Further, a monometer was fabricated for the purpose of verification test of the transducers and calibration of their performance in our real time data extraction and processing in our designed Labview© 8.5 VI program.

Using the manometer shown in Figure 20, we could excite the transducers in increments of 0.05 psi and compare the performance of each transducer with the factory certified data.

**Figure 20. Monometer that was fabricated in FIU ARC laboratory for pressure measurements.**

Figure 21(a-b) shows the comparison of the sensor data from the pressure gauge and the manometer with the factory data for two pressure transducers. Our statistical analysis resulted in data within 95 percent confidence interval. These results showed that the data from manometer traced the factory data with less than 1.5 % of deviation; however, it was suggested to skip one data point in the curve fitting to avoid overlap of the confidence intervals of measurements.

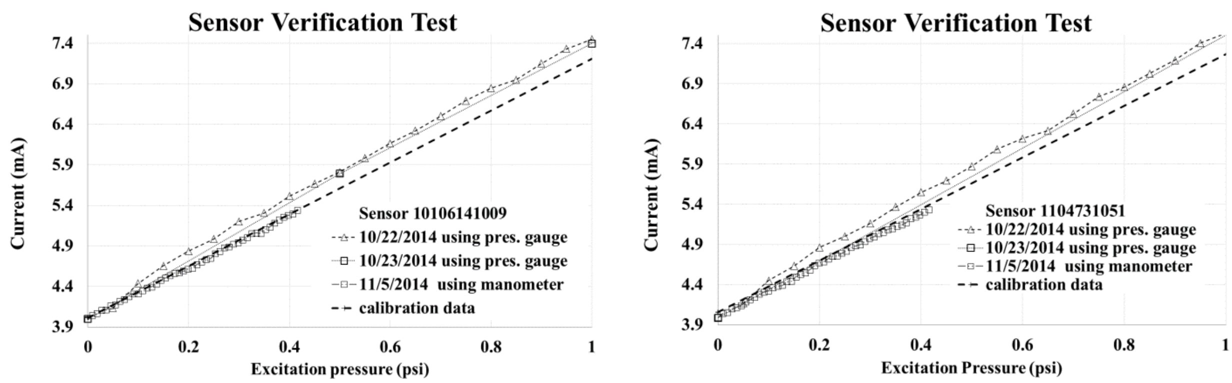


(a) (b)

**Figure 21. Sensor verification tests using manometer and certified 0-5psi pressure gauge, (a) transducer 10106141009 and (b) transducer 1104731051**

Our pressure measurement result of a non-steady tests in two ports closest to the separation plate (ports 4 and 5) are shown in **Error! Reference source not found.**Figure 22. The test started from 0 rpm speed of the blower and the blower speed was monotonically increased until 800 rpm and decreased back to 0rpm. Initially a 33inch FCC column was sitting on the separation plate.

Figure 23Figure 22 shows that the pressure difference between the ports 4 and 5 could be clearly measured using the 0-5psig type transducers.

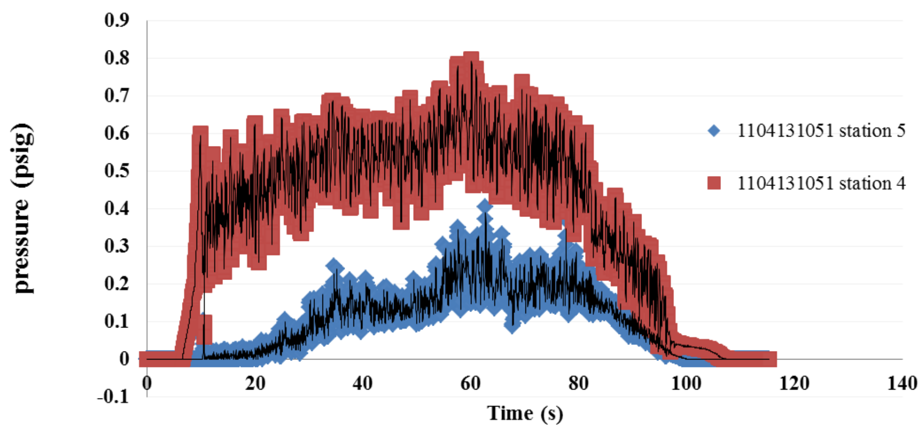


**Figure 22. Pressure difference between ports 4 and 5**

Further, we performed the same experiment by measuring the pressure at the most distant points to the separation plate on the riser, i.e., ports 8 and 9. This time the speed of the blower was kept constant on 420rpm, 450rpm, 480rpm, and 510rpm for 2 minutes.

Figure 23(a) shows a slight difference between current readings of the transducers at ports 8 and 9. In order to create more pressure difference between the ports 8 and 9, we repeated the test with 46” of static FCC column.

Figure 23(b-f) shows the current readings and the converted pressure values at different speed of the blower. Again, the results show lack of sensitivity of the transducers in response to pressure difference.

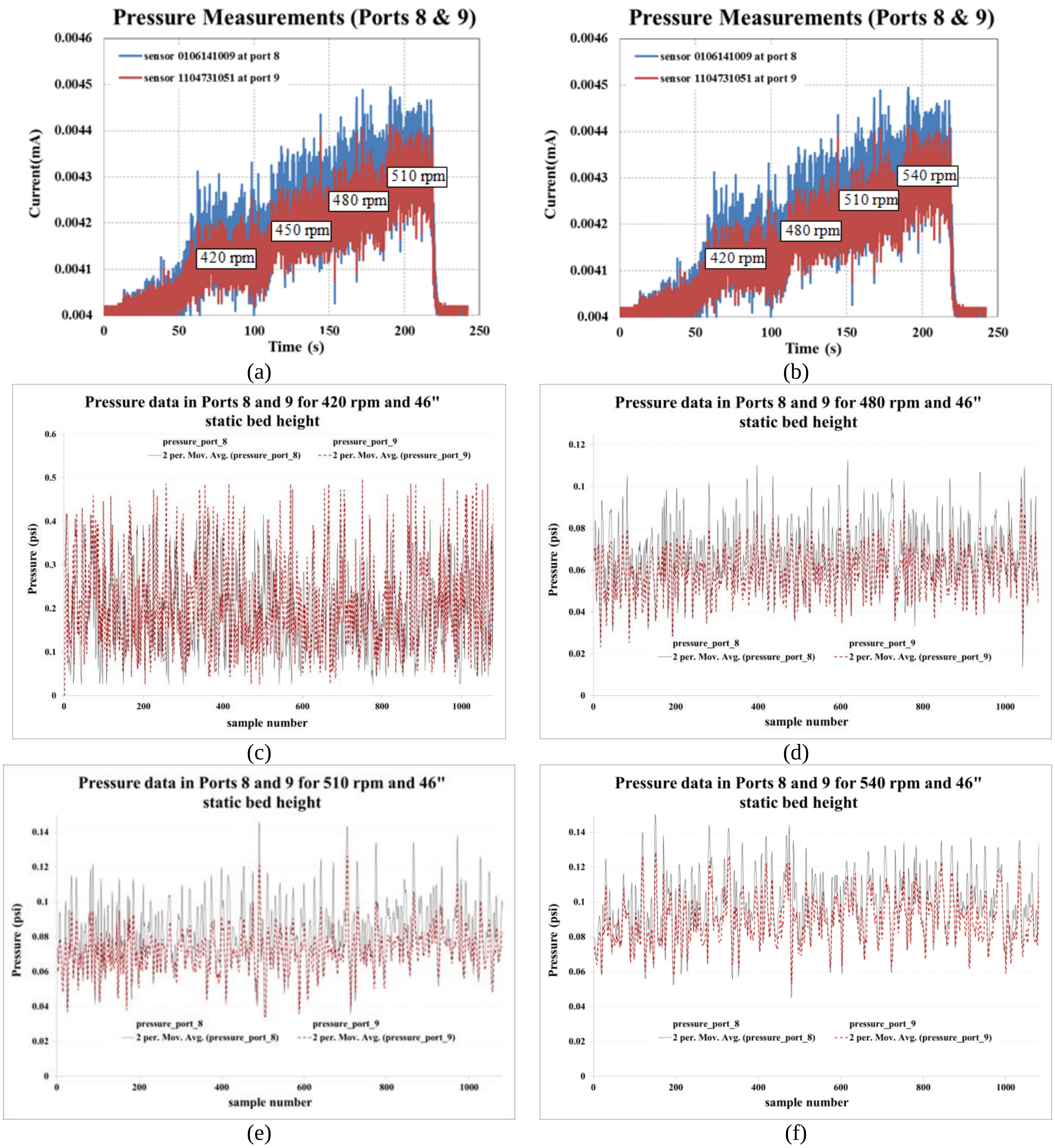


**Figure 23. Pressure difference between ports 8 and 9, (a) 33” FCC column and current readings, (b) 46 inch FCC and current readings, (c-f) 46” FCC and data after conversion to pressure.**

Further we performed steady-state tests for pressure measurements in ports 6 and 7 along the riser of the CFB at FIU. In our test, we collected measurement data during 5 minutes at blower speeds of 420rpm, 450rpm, 510 rpm, 540rpm, 570 rpm, and 600 rpm. Results showed that a transition happened from the fast fluidization regime of the flow observed in Figure 24(a-b) to the pneumatic transport regime of the flow, as observed in Figure 24 (c and d). However, using the 0-5 psig transducers couldn't result in distinct pressure difference in the fast fluidization regime. Thus, 0 to 2psig pressure transducers were purchased to better suit our measurement applications at ports 6, 7, 8, and 9 ports.

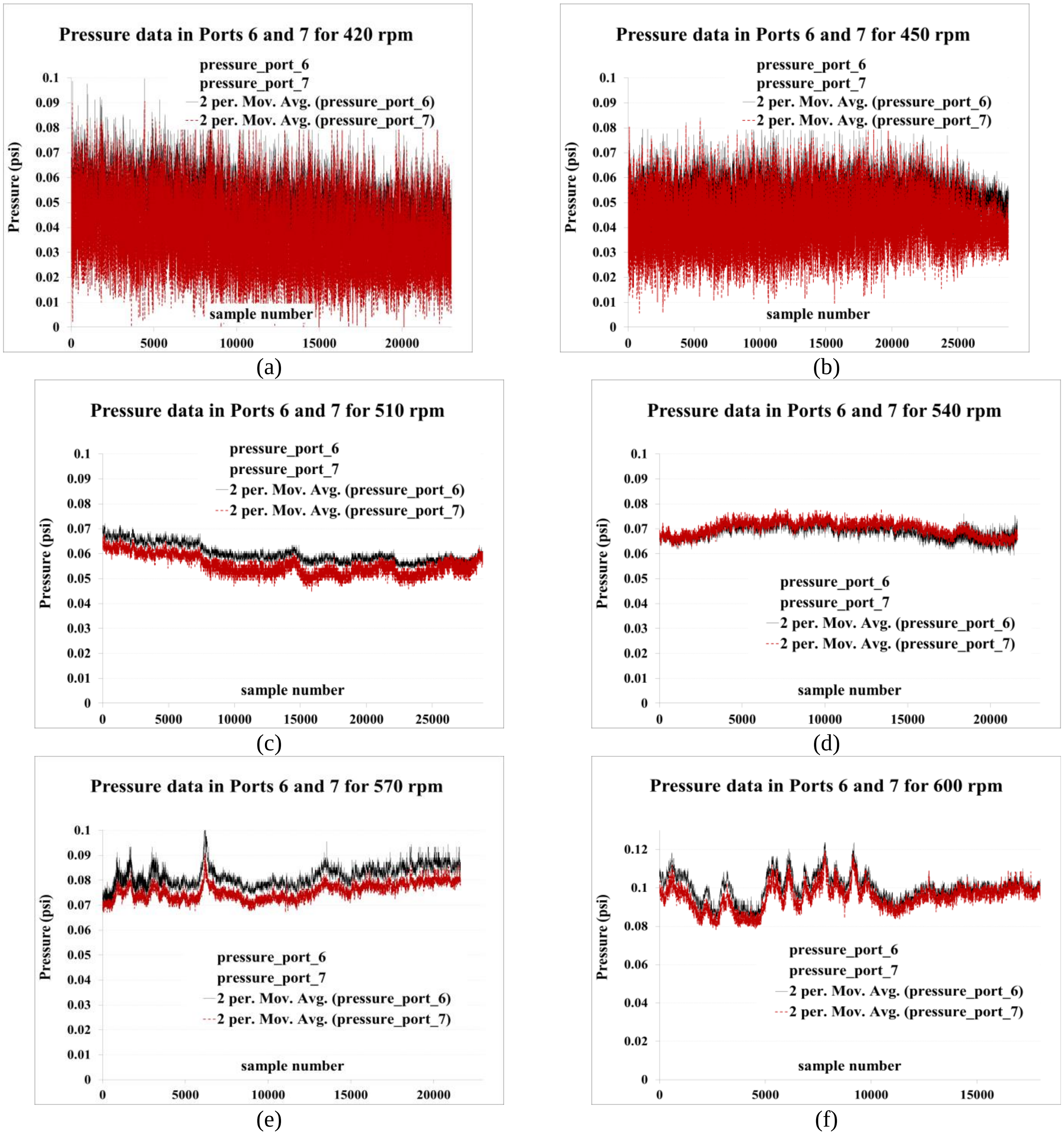


**Figure 24. Pressure difference between ports 6 and 7 for steady tests at different speeds of the blower.**

## Measurement of the solid flux rate

Solid flux rate measurement was needed to create accurate boundary conditions in the MFIX simulations to replicate the CFB experiments for validation purposes. An experiment was designed to measure this quantity as a function of position of the sliding handle of the valve when the system was not running. In fact, this approximation was based on the realization of slight effect of the pressures above the inventory of material (close to atmospheric pressure) and the pressure fronting the flow of the solid, which was negligible in comparison to the weight of the material above the orifice, working as the driving force.

Figure 25 illustrates the characteristic volume and computation of the mass flux obtained from the SolidWorks software. To construct this volume, a reference line and a horizontal indicator line were considered. The indicator line passed through junction of inclined and vertical pipes of the white PVC part, as shown in Figure 25(a). Lighting provided us to use the weak transparency of the inclined plastic pipe and measure the time between the start of partial opening of the sliding valve and observation of the horizontal level of the material on the indicator line. Maximum packing ratio of 0.5 and the density value from our measurements (845 $kg/m^3$) was used to find the mass flow rate of the falling FCC material using the

Equation 7. The results of this experiment are displayed in Table 2.

$$\dot{m} = (\varepsilon_{max} . V_c . \rho_{FCC}) / time \qquad \textbf{Equation 7}$$

**Table 2. Mass flow rate and Mass flux calculated for the FCC in different openings.**

| Position of the sliding indicator (inch) | Mass flow rate (kg/s) | Mass flux ($kg/m^2.s$) |
|---|---|---|
| 1 | 0.00 | 0.00 |
| 1.25 | 0.001 | 2.63 |
| 1.50 | 0.045 | 10.06 |
| 1.75 | 0.167 | 37.10 |
| 2.00 | 0.234 | 51.96 |

## Minimum Fluidization Experiment using the bubbling bed

The minimum fluidization test using a sensitive monometer was done inside the bubbling bed. Air flow rate was measured using the VFB65 SSV Float® with the accuracy of 3% in full scale. The temperature of the inlet air (regulated compressed air) at the working pressure (0.1 bar gauge = 1.4504 psig) was measured using a T-type thermocouple as 22.7 $\pm$0.3 $^oC$ and the Dwyer manometer MARK II 25 with maximum pressure of 3 inch of water was used. The Equation 8 was used for conversion of the standard flow rate to actual flow rate at the test condition.

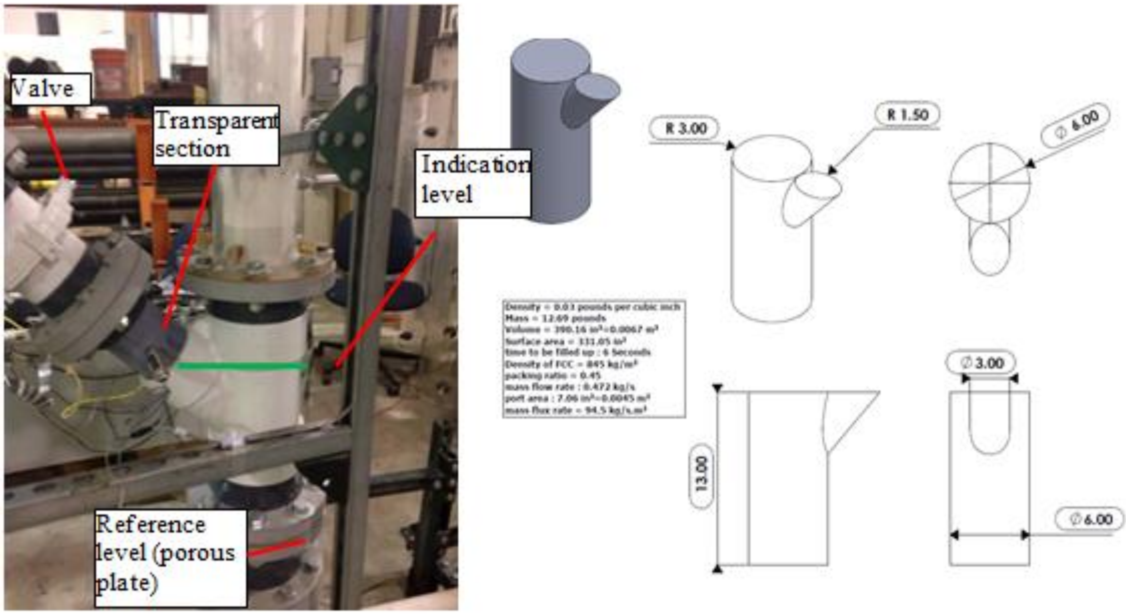


(a)

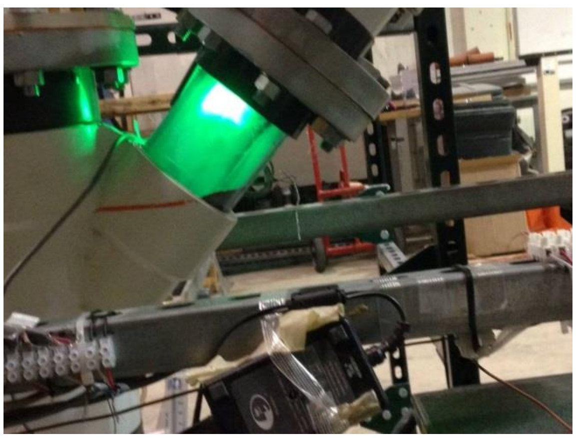

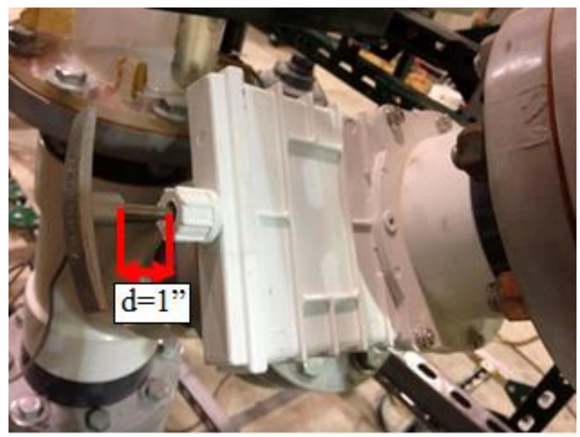


(b) (c)

**Figure 25. Solid flux measurement test, (a) the characteristic volume for measurement, (b) snapshot of the solid mass flux measurement experiment, and (c) view of the position of the valve handle indicator at the fully closed position (d= 1”).**

(b) (b) (c)

**Figure 26. Pressure drop and bed height increase measurement in small bubbling set up (a) using the Dwyer manometer MARK II 25 (b) and the VFB65 SSV Float® Rotameter**

$$Q_a = Q_s \times \frac{P_s \ T_a}{P_a \ T_s} \qquad \textbf{Equation 8}$$

Here $Q_a$ and $Q_s$ are the actual and observed/standard flow meter reading, respectively. $P_a$ is the actual pressure (14.7 psia + gauge pressure), $P_s$ is the standard pressure (0 psig) , $T_a$ is the actual temperature (460 R + Temp °F), and the $T_s$ is standard temperature (530 R= 70°F).

Figure 27 shows the results of our minimum fluidization velocity test. From these results, the homogenous bed expansion and increase of the pressure drop until the minimum fluidization velocity was clearly observed, which is in good qualitative agreement with similar tests published in the literature. However, the minimum fluidization velocity for our spent FCC sample at FIU was about 0.0025 m/sec. This result was close to $u_{mf}$ = 0.0035 m/sec reported by Ellis (2003) for spent FCC powder. Different value of $u_{mf}$ ($u_{mf}$ = 0.005) for the fresh FCC sample was reported to us in a private communication with Mr. Shadle L. (private communication, March 24, 2014), that was obtained from an experiment in the National Energy Technology Laboratory .We believe that the source of this difference roots in the quality of the sample in terms of its freshness.

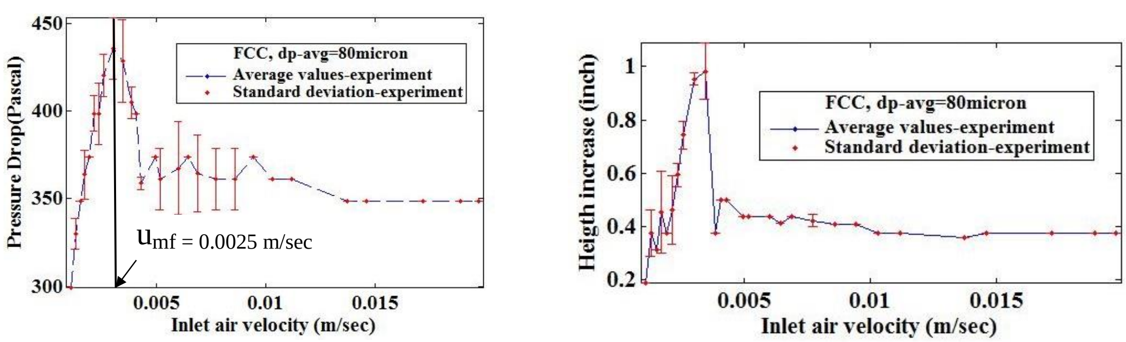


**Figure 27. Minimum fluidization test for FCC, test of pressure drop (a), and bed expansion (b), against inlet air velocity.**

## Image Processing

## High speed imaging system

Shadow sizing technique was used for measuring the velocities and void fraction of FCC particles in our experiments. This technique was used to capture the shadow of the particles, where particles were backlit with a light source and a camera acquires the shadow image of the particles. The light source was placed on the opposite side of the camera allowing the camera to capture the shadow of the solid particle flow in the riser and the camera was connected to the computer, which could control the time and exposure of the camera lenses.

Thus, later the CCD camera was replaced with a high-speed camera (Vision Research v5.0) that had 3800 pps shooting capability at a resolution of 512×512 pixels. The maximum frame rate was 60,000 pps at a resolution of 256 pixels in horizontal resolution and 32 pixels in vertical resolution. A telecentric lens (Edmund Optics Inc. 55–350) was used, that had a horizontal field of view of 8.8 mm and a depth of field of 1 mm according to the manufacturer's technical specification sheet (Edmund Optics, 2011). An LED light source was placed behind the particles to provide an even illumination of the flow field.

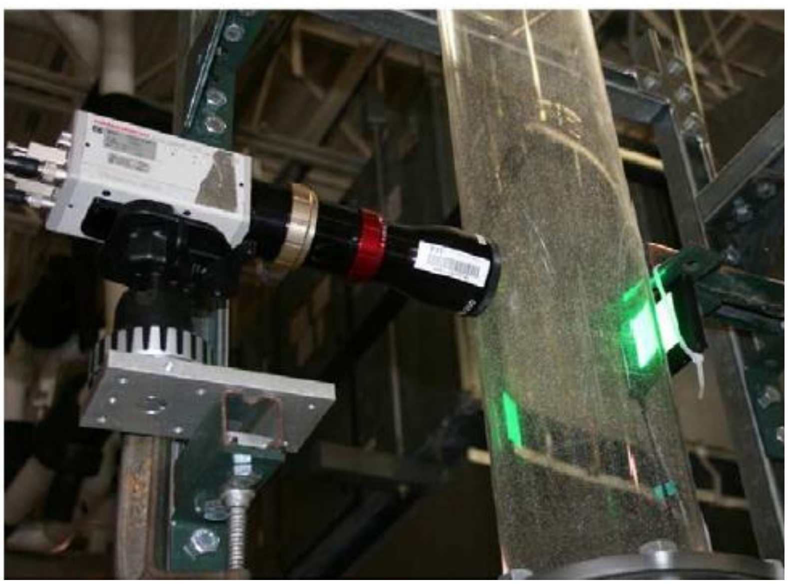

**Figure 28. Typical setup for a shadow sizing experimental setup**

Figure 29(a) shows the original image that was obtained from a location inside the riser of the CFB at FIU. The image filtering functions in the Matlab environment assisted us to remove the statics from the wall using the gray thresholding and noise removal filtration operations, as shown in Figure 29 (b-c). Further enhancements were obtained through histogram equalization operation, FFT filtration and color inversion, and boundary and centroid identification, as shown in Figure 29 (d-f).

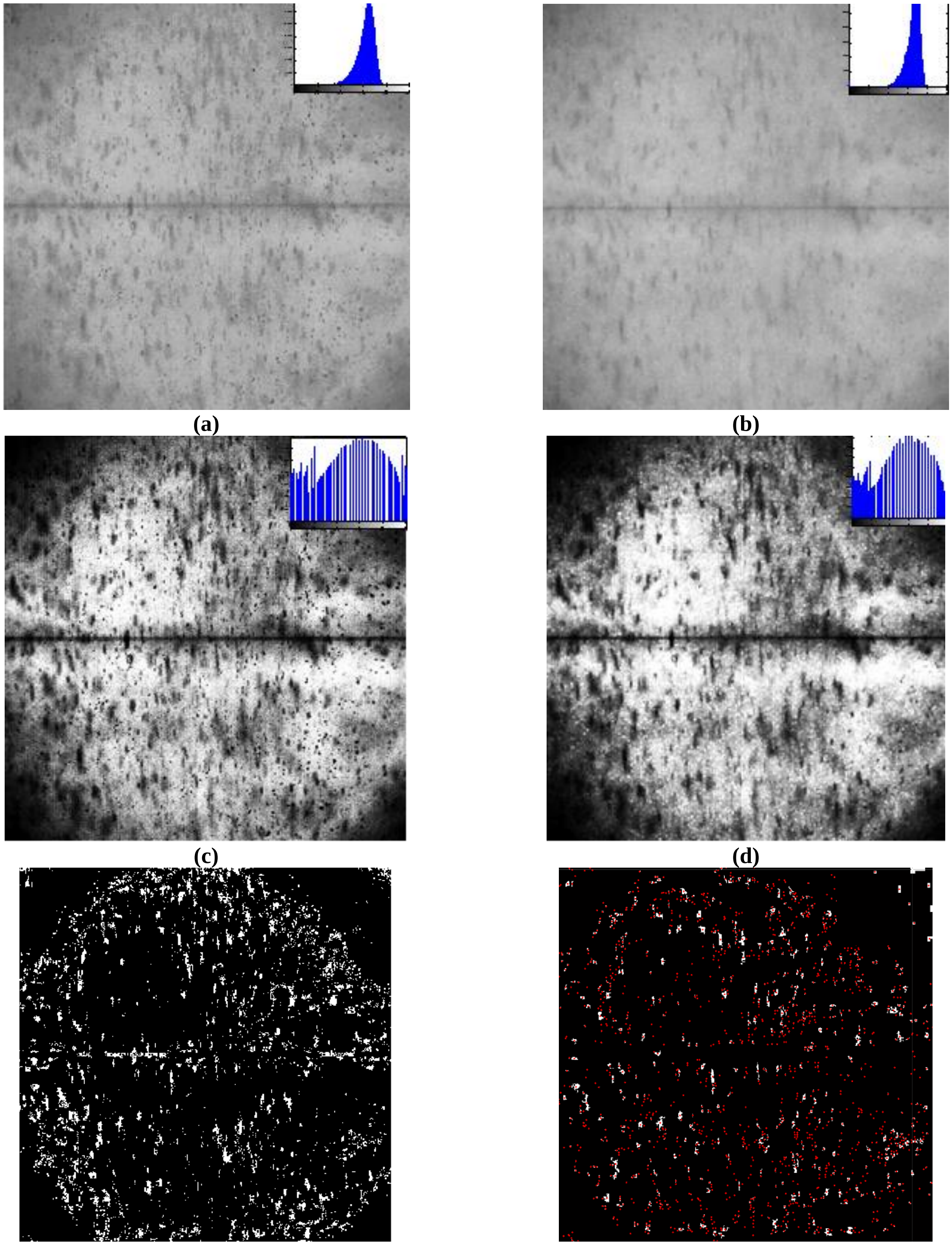

(a) (b) (c) (d) (e) (f)

**Figure 29. Image processing of the images taken from the high speed camera, (a) original image, (b) removal of on-wall statics from the image, (c) noise removal and gray thresholding, (d) polished image with equalized histograms, (e) FFT filtration and color inversion , (f) boundary and centroid identification.**

## High speed image acquisition in the bubbling bed

## Imaging polystyrene particles

The Phantom v5.0 high-speed digital CMOS camera was successfully incorporated into the small bed body frame. Setup allowed for vertical, lateral and longitudinal motion of camera. This adjustment enabled us to focus at various depths inside the transparent tube. Two snap shots of the flow, as shown in Figure 30, were taken in different depths inside the wall in a dilute region of the bed. The shadow images of the polystyrene particles with average diameter of 358 µm. in these images, red boundaries indicate the particles that formed pairs.

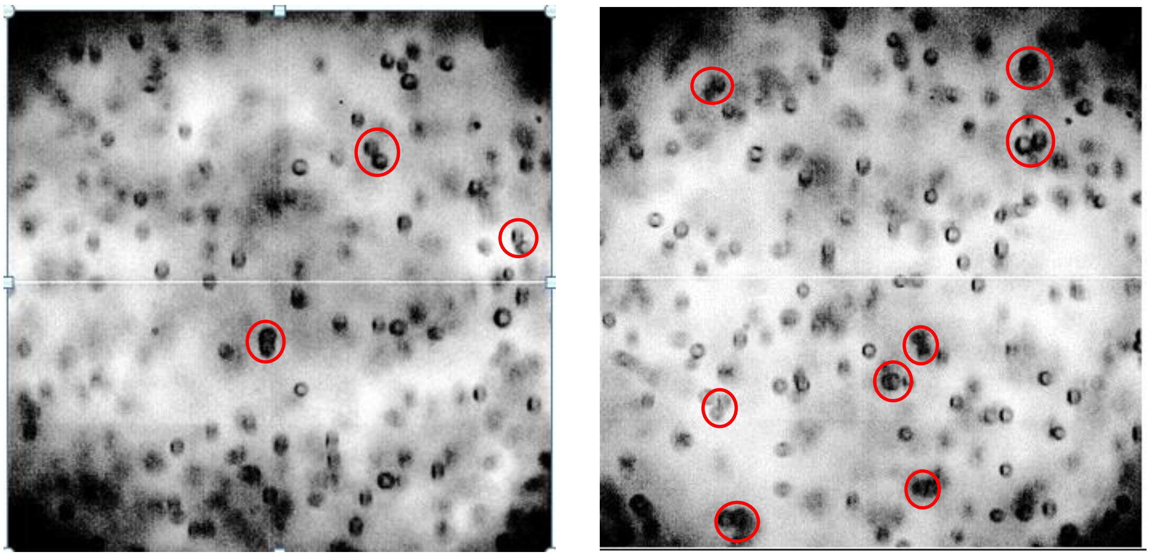

(a) (b)

**Figure 30. Outside-wall images taken from Polystyrene particles flowing inside the riser (a) focus at the radial location r/R=0.875 and (b) focus at the radial location r/R=0.938**

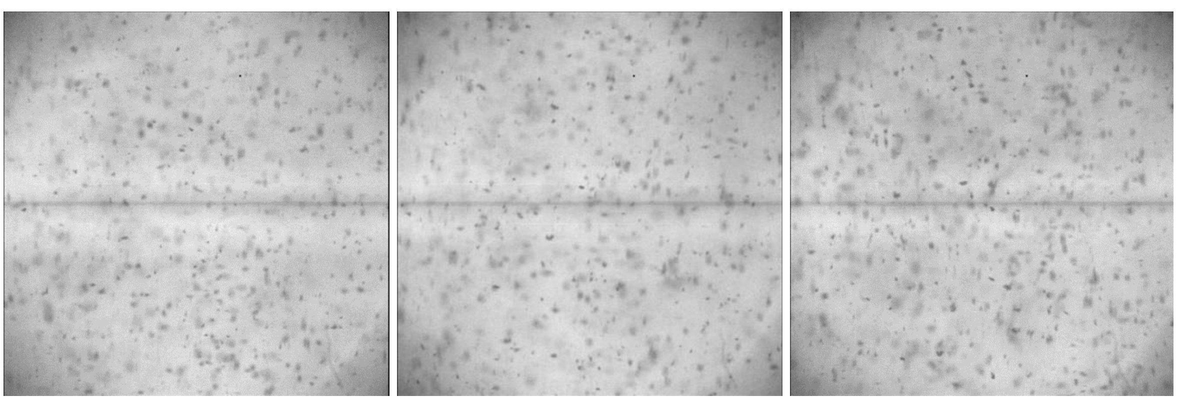

**Figure 31. Particle cluster images of FCC catalyst in the FIU bubbling bed.**

## Imaging FCC particles

Shadow imaging tests of our FCC material, characterized with average diameter of 79.03µm and strong cohesiveness, encountered serious issues of static electricity. This caused the particles to stick to the interior walls of the acrylic riser and block the imaging window. Application of the static guard agent to the system was a helpful method, to temporarily remove the statics from the riser wall and obtain images with recognition of particle clusters. Figure 31 shows the three images obtained using the high speed Phantom v5.0 camera with the FCC particles forming clusters in the bubbling bed.

## Image processing for analysis of the optical microscopy images

Optical imaging of the FCC catalyst was performed in order to obtain more accurate statistical information about the distribution of properties of the FCC powder in our analysis, such as the size and the degree of sphericity. This method could provide advantages such as improved accuracy and faster and cleaner information extraction in comparison to the conventional sieving procedure. Preprocessing operations such as image inversion, rescaling, and cropping were performed in the ImageJ software and boundary detection operation was performed through Matlab scripts. Figure 32(a-c) shows the procedures followed to improve the quality of the original image. These results show that the program needs more tuning adjustments to capture all particles in a wider range of diameter values.

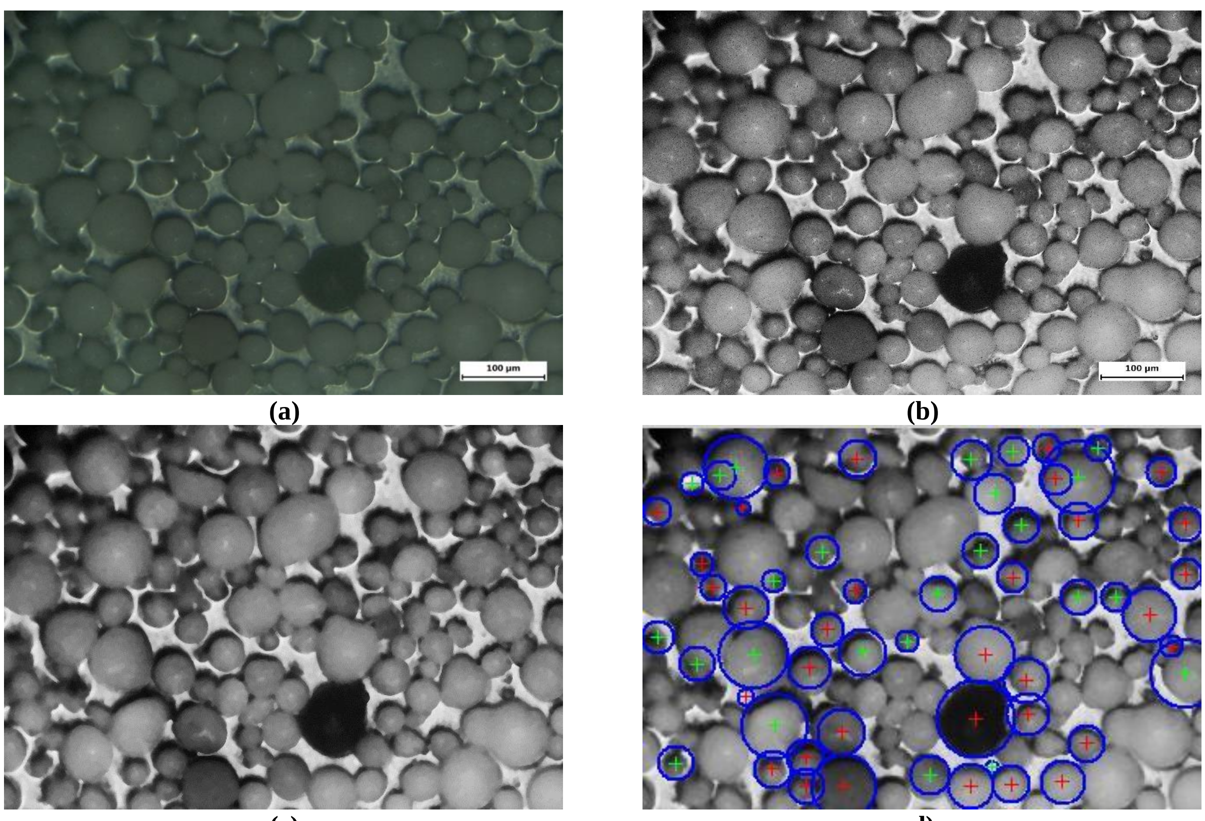


**Figure 32. Image processing, FCC material imaged under the Optical Microscopy, (a) original image, (b) converted and grayscale/histogram equalized image (c) noise eliminated image (d) boundary detection.**

# Numerical modeling

## DNS Simulations to Develop Improved Drag Laws for Clustering Particles

### Computer model for cluster structures for DNS

The main objective was to develop a robust method to computationally reproduce particle configurations exhibiting the same characteristics as those observed in experiment. However, it should be noted that generation of such particle configuration was non-trivial because different particle configurations could yield same properties. The numerical approach to create particle assemblies is available in the Appendix chapter of this report. Figure 33 shows the reduction of the objective function and the convergence of the numerical and experimental results for two solid phase volume fraction, Φ=0.1 and Φ=0.2.

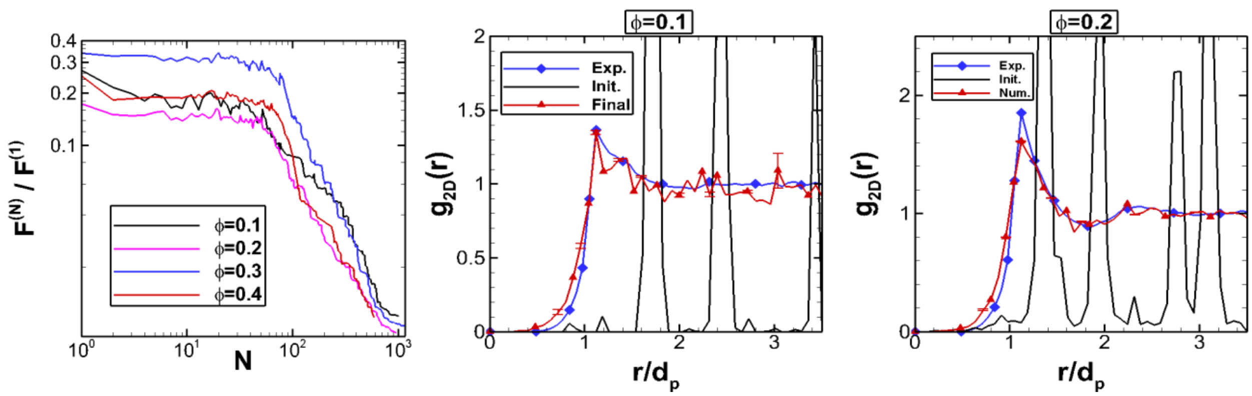


**(a)** **(b)** **(c)**

**Figure 33. Creation of configurations of particles, (a) optimization procedure, (b and c) agreement between the experimental and numerical g(r) functions) , (b) Φ=0.1 and (c) Φ=0.2**

## Developing an improved drag law for clustering particle systems

In order to develop an improved drag law for clustering particle systems, we first performed particle-resolved direct numerical simulation (PR-DNS) of flow past fixed assemblies of clustered particles. The Figure 34(a) shows a configuration of particles constructed using the optimization procedure explained earlier. In this assembly, a cubical configuration with solid volume fraction of Φ=0.083 was extracted and this assembly, as displayed in Figure 34 (b) is consisted of particle clusters of different particle numbers.

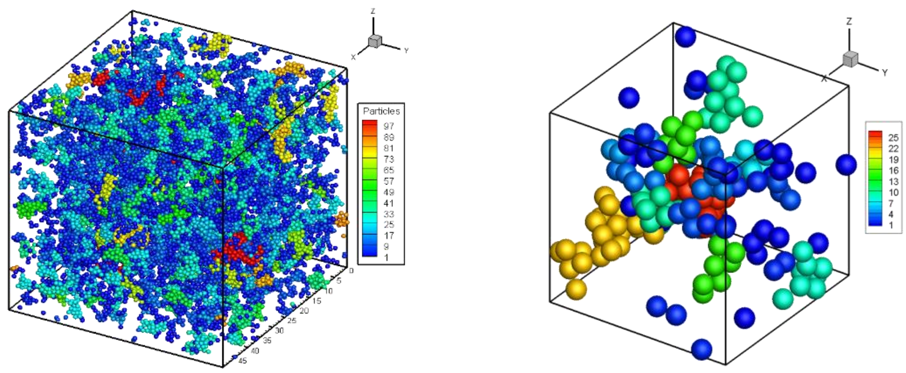

(a) (b)

**Figure 34. Representation of particle configuration for a collisional system of cohesive particles undergoing elastic collisions. (a) Complete configuration (b) sub-ensemble extracted from collisional cohesive particles used for PR-DNS. The coloring indicates the number of particles, Φ=0.083**

## DNS simulations for clustered particles

The particle ensemble configurations, such as the configuration shown in Figure 34 (b), were used in the in-house developed particle-resolved DNS code, PUReIBM (Particle-resolved Uncontaminated-fluid Reconcilable Immersed Boundary Method), to investigate the drag force on particle clusters in gas-solid flows. A grid independence study was performed for configurations which is available in the appendix chapter. The mean drag force $F = |\mathbf{F}| / \left(3\pi d_p \mu (1-\phi) |\langle \mathbf{w} \rangle|\right)$ was defined as the average hydrodynamic drag force exerted on a single particle normalized by the Stokes drag force at the same mean slip velocity $\langle \mathbf{w} \rangle$. In this expression, the dp, μ, and Φ are the particle diameter, dynamic viscosity of the fluid around the particle, and the solid phase volume fraction. According to results, as shown in Figure 35, a significantly smaller drag force was predicted for cluster ensembles in comparison to the drag force for uniform configurations.

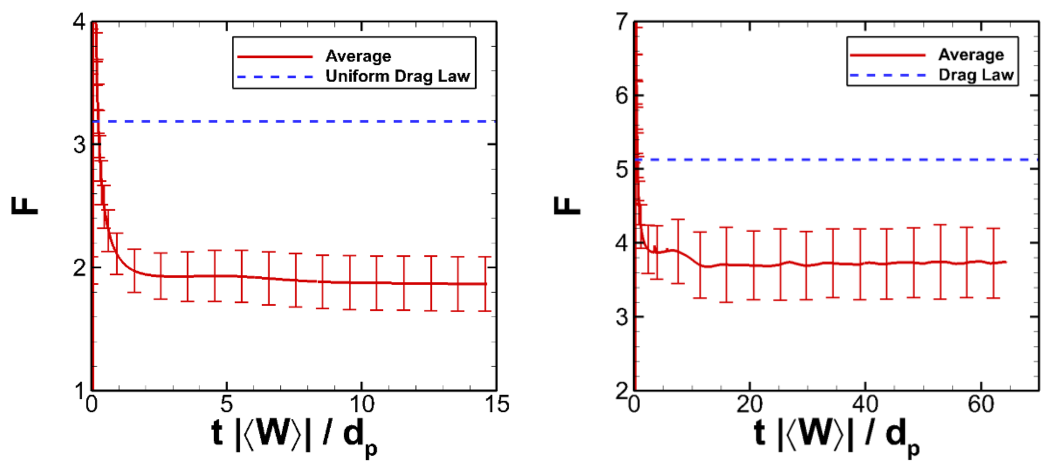


(a) (b)

**Figure 35. Evolution of mean drag force in clustered particle configurations compared with the uniform configuration drag law proposed by Tenneti et al., (a) $Re_m$=10 (b) $Re_m$ = 50**

**Initial form of the drag low for cluster of particles**

The initial form of the drag force on clustered particles was envisioned to depend on the characteristics of the particle cluster in the fluid flow. Equation 9 represents this form of the drag force, which takes into account the solid volume fraction, the Reynolds number around the particles, the effect of anisotropy and orientation of the cluster, the ratio of the frontal area to the wetted area of the cluster, and the ration between the cohesive inter-particle forces to the hydrodynamic forces. The last factor could define the competition between formation and breakup of the clusters. The hydrodynamic forces are responsible for breakup of the clusters and are partly due to particle fluctuation energy (granular temperature).

$$F=f(\Phi, Re_m, e_i^f e_j^p, \frac{A_f}{A_w}, \frac{F_{int}}{F_{coh}}) \qquad \textbf{Equation 9}$$

In this definition, $\mathbf{e}^{(p)}$ and $\mathbf{e}^{(f)}$ represent the orientation of clusters and the orientation of the mean flow, and the term $\mathbf{e}^{(p)}\mathbf{e}^{(f)}$ accounts for the cluster structure and its orientation with respect to the mean flow. Figure 36 (a) shows the dependency of the drag force on the $Re_m$ of the flow around the cluster for Φ=0.084. This result showed that drag force increased with the increase of the Reynolds number and there is a significant reduction of the drag force (up to 45%) for the cluster configuration. DNS simulation results with different tensors of orientations are shown in Figure 36 (b). This results which are at $Re_m = 10$ and Φ=0.084, indicated that there was no significant difference in the average drag force in terms of the flow direction angle. Figure 36(c) shows the dependency of the drag force on the number of particles in the cluster for $Re_m$=5 and $Re_m$ = 20. As shown by this figure, very close results were obtained at these two values of the Reynolds number.

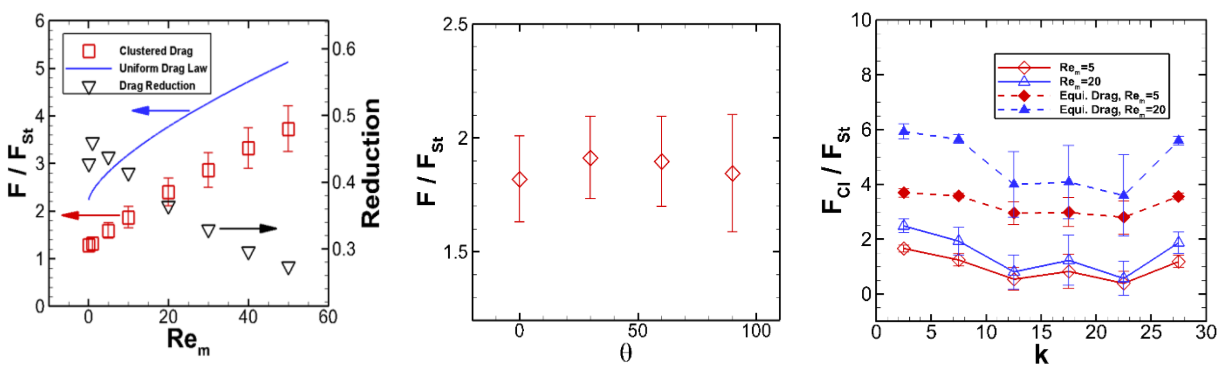


(a) (b) (c)

**Figure 36. Comparison of drag force in uniform and cluster configurations, Dependency of the mean drag force, (a) dependency on $Re_m$, (b) dependency on orientation of the cluster with respect to the mean gas flow, (c) dependency on number of particles in the cluster.**

Further, for simplicity, it was assumed that dependency of the drag force on the parameter $A_f$/Aw could be ignored. The uniform drag corrections were used to take into account the effect of the Φ and the $Re_m$. The last parameter in the proposed form of the drag, as knows by $F_{int}/F_{hyd}$, was a key parameter to determine whether or not particle clusters were prone to form in a computational cell. If the inter-particle forces were strong enough to attract particles into a cluster compared to hydrodynamic forces, which drive away particles from each other, the clustered drag law could be used. Otherwise, the uniform configuration drag law would be in effect.

## Cohesive index

The $F_{int}/F_{hyd}$ was defined as a measure of the particle-clustering tendency in the simulation results. Derivation of equations governing the motion of particles in presence of the cohesive interparticle forces could lead to a parameter that was denoted as the ratio of attractive to repulsive interparticle forces, named as Ha. Equation 10 shows the expression of the Ha, and derivation of equations is available in the Appendix chapter.

$$Ha = \frac{A}{\pi \rho d_p^2 d_0 \Theta_s} \quad . \qquad \textbf{Equation 10}$$

In order to investigate the effect of Ha parameter on the formation of particle clusters, simulation cases with three different values of the Ha parameters denoted as Case I: Ha=0.39, Case II: Ha=0.0039, and Case III: Ha=0.000039 for the volume fraction $\Phi$=0.1were considered. In these simulations, 23,731 particles were placed uniformly inside a cubic box with the characteristic side length of L= $50d_p$. Particles were initialized with a Maxwellian velocity distribution characterized by T=0.0085 $(m/s)^2$. The equations of motion of particles under the effect of interparticle cohesive forces (available in Appendix part) were solved to find the position of particles after the kinetic energy of these systems reduced to less than 5% of the initial energy.

The results, as shown in Figure 37, revealed that onset of cluster formation was more likely determined by the value of Ha., as drastically different results were obtained with the Ha=0.39 and Ha=0.0039. However, since the results with Ha=0.0039 and Ha=0.000039 are slightly different, once clusters were formed, their characteristics in terms of structure and distribution might be universal. Additionally, this results shows that more populated clusters happened to form with higher values of the Ha. This realization stands for a direct relation between the Ha and cohesion between particles.

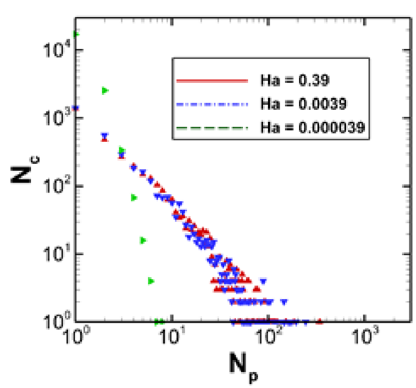


**Figure 37. Distribution of clusters with respect to the number of particle.**

## Simulations in MFIX

### Principle simulation

A study was conducted to investigate the differences in simulation results obtained using the Two-Fluid method (TFM) in the MFIX code where the algebraic and transport equations for the granular energy were solved. These equations along with the definition of terms are available in the appendix part of this report. In the simplest case, the default drag model in MFIX, the SYAM-OBRIEN was used to simulate the flow in a 7 (cm) by 100 (cm) bubbling fluidized bed, as shown in Figure 38. The boundary conditions and simulation set up for this simulation are available in Appendix chapter of this report. In this case a central jet velocity of 124.6 cm/s combined with a uniform inlet air with the velocity of 25.9 cm/s in vertical direction from the distributor plate in a symmetrical coordinate system were considered. The total length of the simulation was set to 0.1 seconds and a flexible time stepping method with start of time-step size of 0.0001 s was considered. This method guaranteed convergence by reducing the step size until converged solution was obtained in each time step. Further, to refine the computational results in our post processing, a 121x1981 cell-by-cell grid was considered in our Ha calculations.

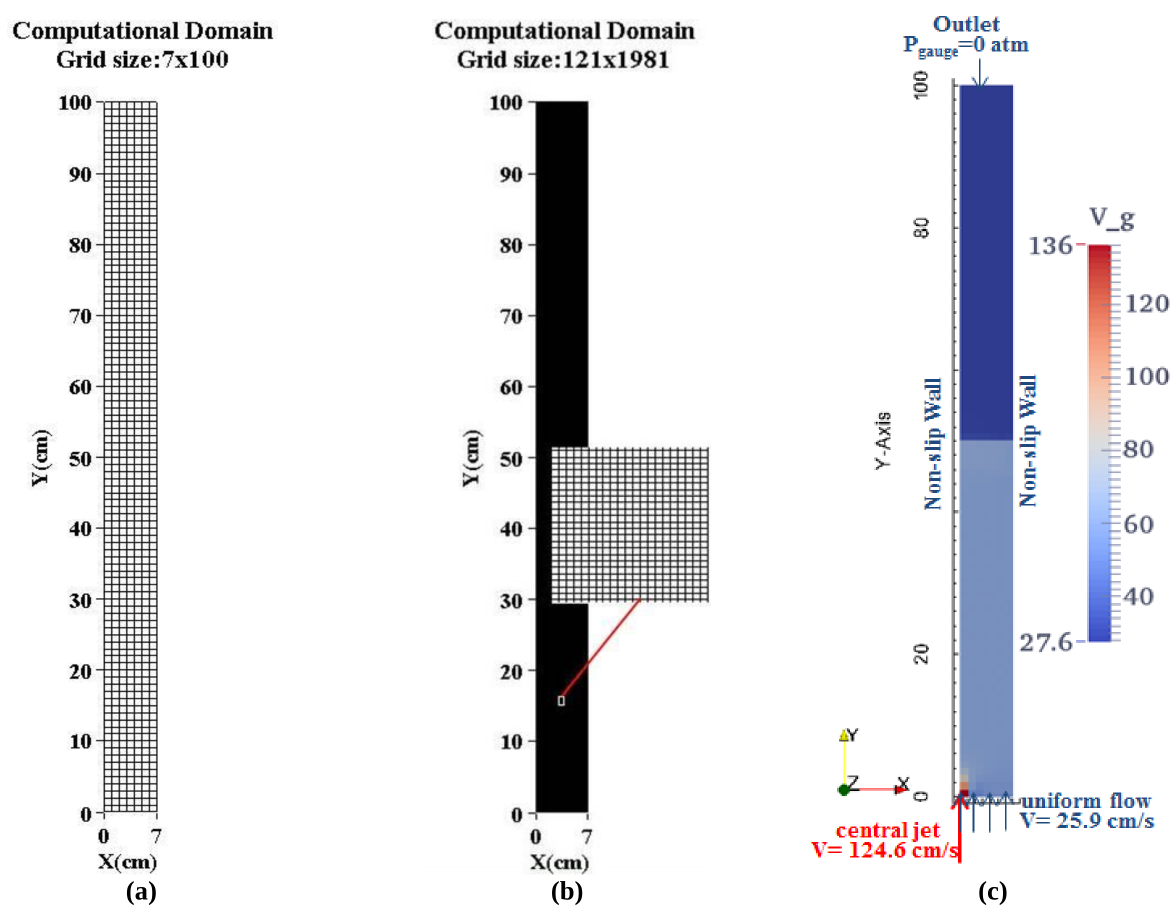


**Figure 38. Computational domain and the boundary conditions used for our principle simulation, (a) 7x100 grid , (b) 121x1981 grid for post processing refinement), and (c: boundary conditions).**

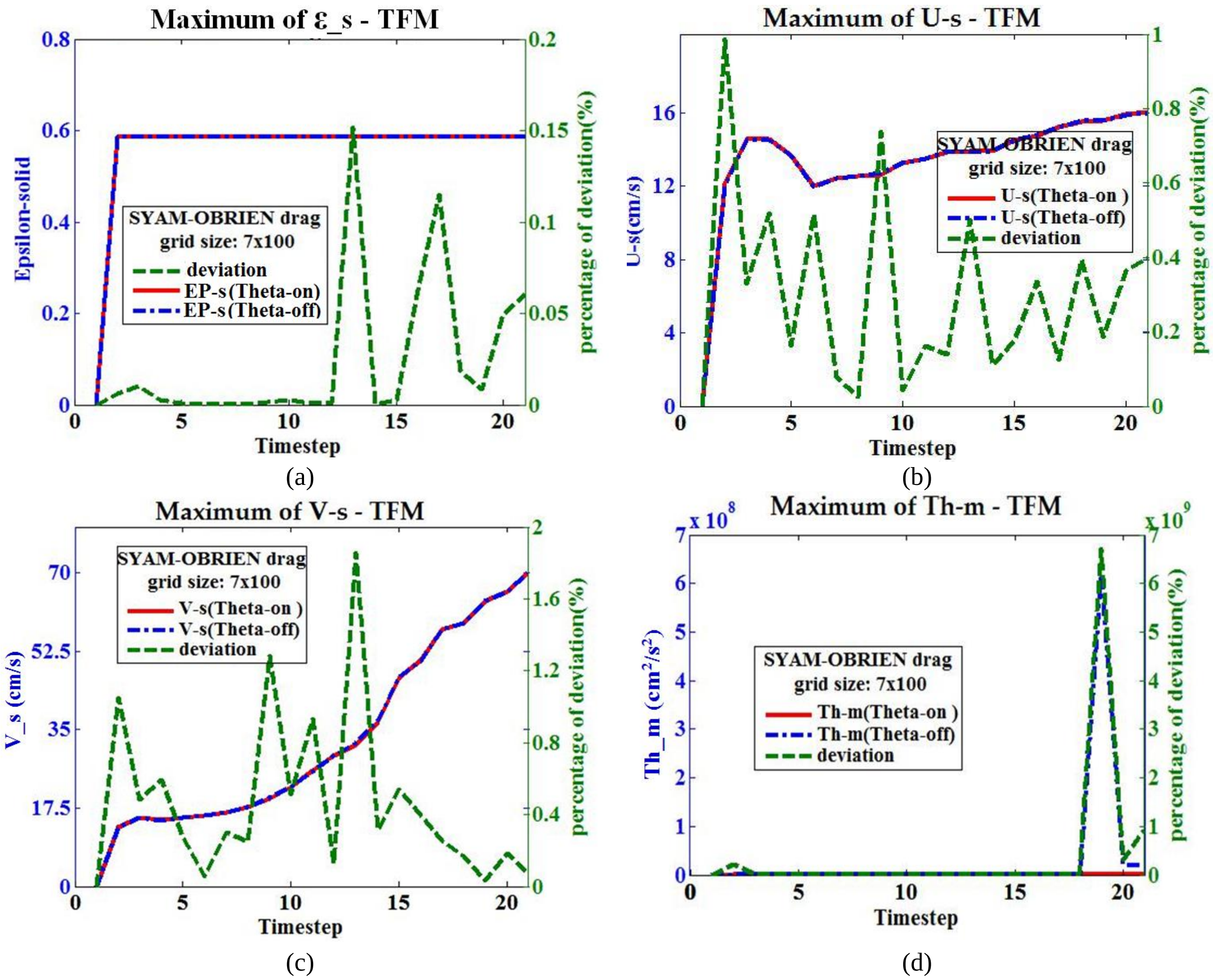


**Figure 39. Comparison of MFIX simulation results for algebraic (shown in blue and named as Theta-off) and transport (shown in red and named as Theta-on) equations of the granular temperature, (a) maximum of solid volume fraction, (b) radial solid velocity, (c) axial solid velocity, (d) and the granular temperature in the domain.**

Deviation of the results for each variable shown in Figure 39(a-c) revealed that use of the algebraic and transport equations of the granular temperature resulted in very similar quantities for the field variables ε_s, u_s, and v_s. However, significant deviation existed between the results shown by Th_m in Figure 39 (d). This huge deviation was associated with the non-physical results that were obtained due to error of the numerical modeling when ε_s approached zero in some computational regions. Based on these results, we decided to use the transport equation of the granular temperature in all of the simulation cases involved in the reporting period.

## Implementation of the Ha in principle simulation

The Ha parameter was calculated for all the computational cells in all times steps in our MFIX principle simulation. In our approach (named as Scheme 3) we interpolated the calculated values of the Ha on the 121x1981 computational grid. We obtained the granular temperature from the solution of the transport equation and used the Equation 10 to calculate the Ha value for each computational cell. Later, computational cells with Ha values greater than a threshold values, named as Ha_THS, were colored in blue, which helped us to identify the regions with higher chance of particle clustering.

Figure 40 displays the results of implementation of three levels of thresholding, Ha > 5, Ha > 20 and Ha > 50 in times step 11 and, Ha>5 in time step 5. The underlying contour is the contour of the gas volume fraction and this variable was used to better associate our identification procedure (explained earlier) with the phase content of the computational cell. Results in Figure 40 (a-c) showed that increase of the Ha_THS resulted in more filtration of computational cells marked for possible modifications. Based on this result, we understood that the Ha_THS must be carefully tuned for any further modifications.

Figure 40(d) showed that in the fifth time step, a suspicious region was marked for chance of clustering. After we magnified the blue marked region to better investigate about the cell content, Figure 41, we realized that clustering prediction by Ha (in green cross symbols) happened in a region with $\varepsilon\_g > 0.935$. This clustering prediction in an extremely dilute region encouraged us to set a threshold on the volume fraction of the solid for our future simulations.

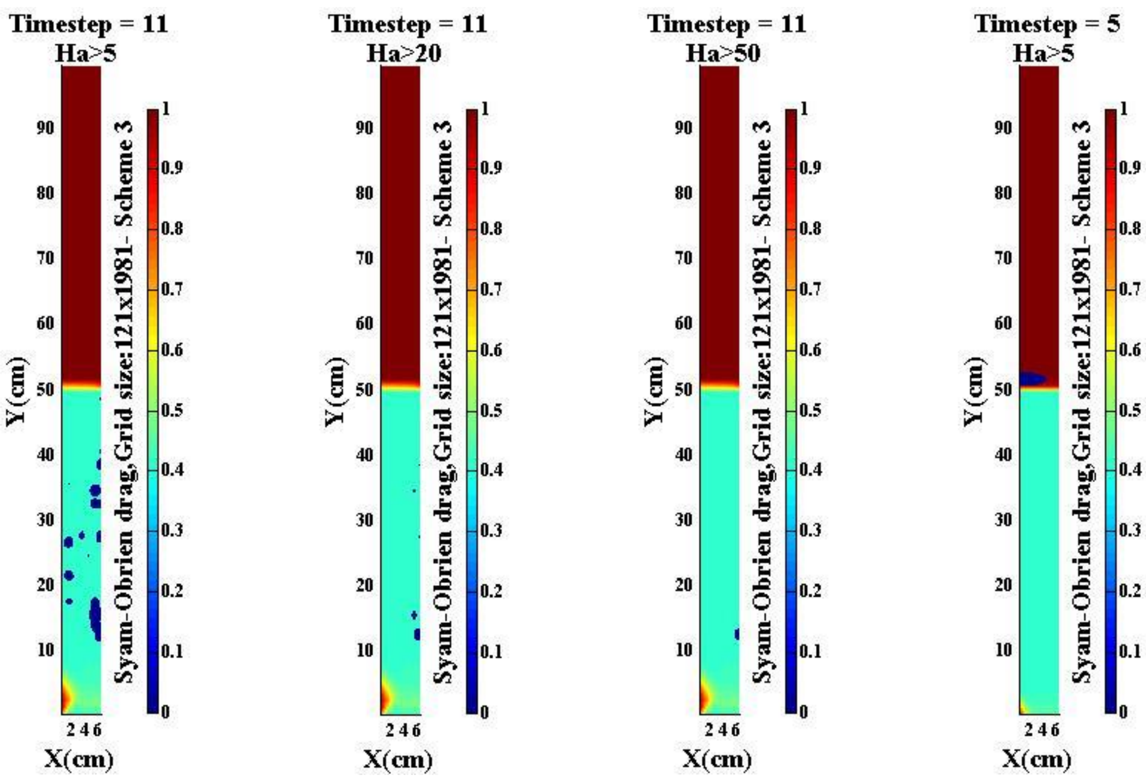


(a) (b) (c) (d)

**Figure 40. Cells marked by Ha thresholding, (a-c) showing the effect of increasing the Ha_THS in time step 11) and (d) Ha thresholding in time step 5**

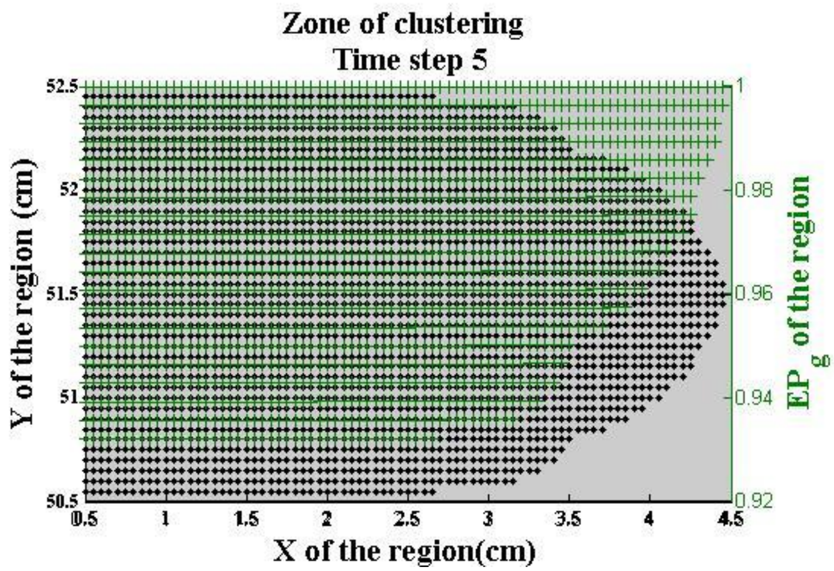


**Figure 41. Candidate zones for clustering predicted at time = 5s with the Syam-Obrien drag model.**

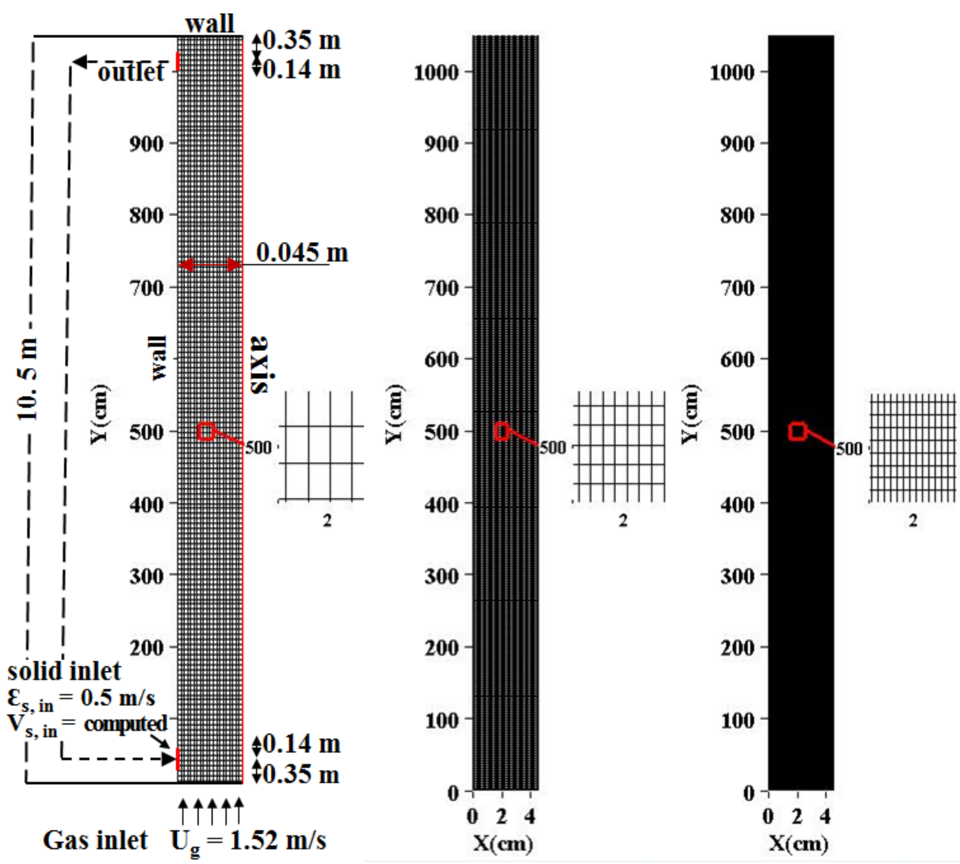


**Figure 42. Computational domain and boundary conditions used for MFIX-TFM fluidized bed flow simulations, (a) 20 × 150, (b) 40 × 300, (c) 60 × 450.**

## Two-Fluid-Modeling simulation of the air-FCC flow using the standard, Particle Resolved-DNS based and hybrid drag models

We performed series of simulations for the fluidized bed flow that is illustrated in Figure 42(a). The computational grids with different grid sizes are shown in Figure 42(b-c) for the purpose of grid independency check. Initially, we used three available standard drag models in the MFIX code, Gidaspow, Wen-Yu and Syam-O'Brien for our simulations. Later, we implemented the TGS drag model in our MFIX simulations for the same flow and geometrical conditions. The TGS model was developed by Tenneti and Subramaniam (2011) based on direct numerical simulation of the flow around particles. Definition of all standard and TGS models along with our simulation set up are available in the Appendix chapter of this report.

### Simulation results of constituent models

Figure 43 illustrates the results obtained with the TGS drag model and the three existing standard drag models on three different computational grids. The computational results were obtained in the last 100 time steps of the simulations and results were time and space-averaged on each cross section along the riser of the fluidized bed. In our analysis for each modeling, the profile of the solid volume fraction was plotted against the available experimental data points. A computer script was used to interpolate the numerical results for specific heights of the riser, where data points were obtained from the experiment of Li and Kwauk (1994). Figure 43 (a) illustrates the grid independency study with the TGS drag model where the computational grid (40×300) was found to be optimum. It was observed from Figure 43 (b-d) that when the existing drag models or the TGS model were used alone, the solid volume fraction profile in the riser showed significant deviation from the experimental data given by Li and Kwauk (1994). Figure 38(d) shows that all models produced very similar results with the increase of the computational grid size, and these results were in good agreement with the simulation results obtained by Hong et al. (2012), where they used the Gidaspow drag model in their simulation of the same flow.

Then, the maximum of the deviation of the numerical data points from the corresponding experimental data points was calculated by Equation 11. Further, for each numerical and experimental data point a relative deviation value was calculated and an average of relative deviations over all of the data points was calculated, according to Equation 12.

$$Err_{max} = \mathrm{Max}\left(\left|f_{exp}(\lambda) - f_{sim}(\lambda)\right|\right) \qquad \textbf{Equation 11}$$

$$Err_{avg.}(\%) = \frac{100}{N} \times \sum_{\lambda=1}^{N} \left(\left| f_{exp}(\lambda) - f_{sim}(\lambda) \right|\right) / f_{exp}(\lambda) \qquad \textbf{Equation 12}$$

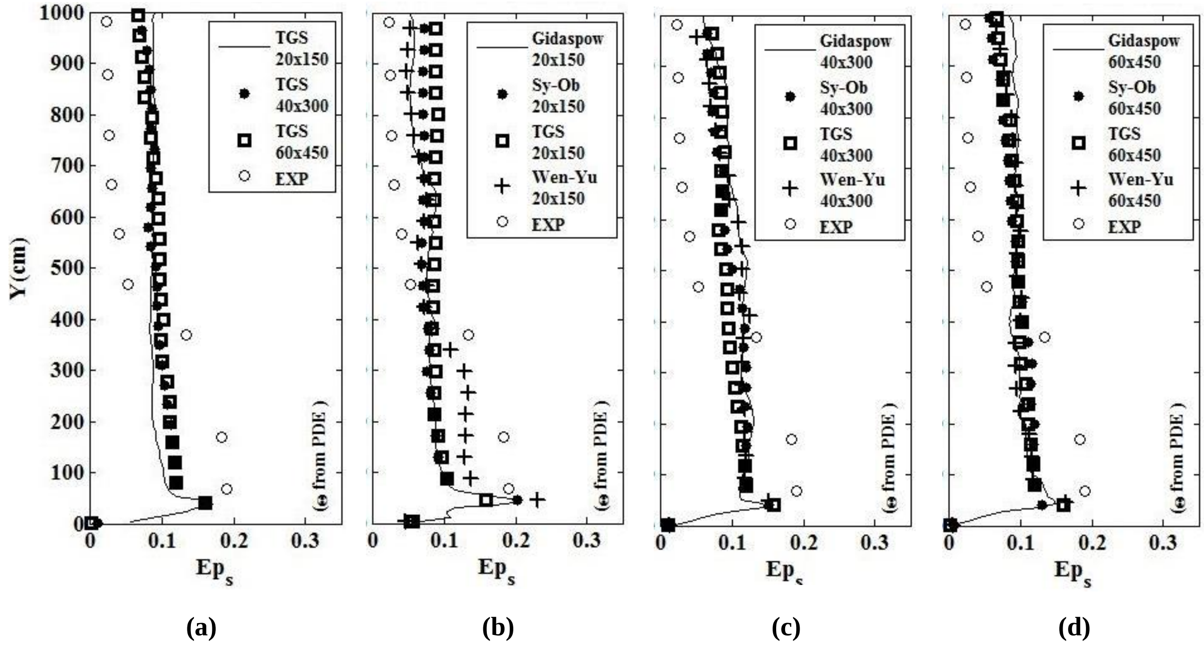


**Figure 43. Profile of solid volume fraction along the riser of the fluidized bed, MFIX-TFM results with TGS and existing drag models on three computational grid sizes**

Table 3 shows the maximum and relative errors in the simulation results for the computational grid size of 20 × 150. These results indicated that in the best case, the Wen-Yu model produced 77 percent of relative error in comparison with the experimental data of Li and Kwauk (1994).

**Table 3. Error in numerical simulation compared to available experimental data of Li and Kwauk (1998) for computational grid size of 20 × 150**

| Simulation Case | Max. error | Rel. error (%) |
|---|---|---|
| Hong et al. (date) | 0.0773 | 166 |
| Syam-O'Brien | 0.0954 | 106 |
| Gidaspow | 0.0959 | 93 |
| Wen-Yu | 0.0545 | 77 |
| TGS | 0.0918 | 143 |

## Simulation using the hybrid drag model in the MFIX TFM code

This work was further extended by introduction of a hybrid model to the MFIX code and the successful simulations of the same test case as explained earlier above. The new drag model was simply defined by Table 4, as is shown in the following.

**Table 4 Definition of the proposed drag model**

| New drag | Criteria |
|---|---|

| | |
|---|---|
| Use TGS | Ha > Ha_threshold |
| Use standard model | Ha ≤ Ha_threshold |

Definition of the cohesive index, Ha, was earlier shown by Equation 10. Threshold of Ha, known as Ha_THS, was used to switch between the TGS and a standard drag model, which were used in earlier sections. Use of the TGS model for larger values of Ha was based on the fact that DNS-based drag coefficients were assigned for cells with higher chance of clustering. We used the Gidaspow, the Wen-Yu, and the Syam-O'Brien, as our standard drag models, to construct three versions of the hybrid drag model as proposed in the Table 5.

**Table 5 Versions of the proposed drag model.**

| Model | Arguments | Condition |
|---|---|---|
| AGDSM 1 | Use TGS | Ha > Ha_threshold |
| | Use Syam-O'Brien | Ha ≤ Ha_threshold |
| AGDSM 2 | Use TGS | Ha > Ha_threshold |
| | Use Wen-Yu | Ha ≤ Ha_threshold |
| AGDSM 3 | Use TGS | Ha > Ha_threshold |
| | Use Gidaspow | Ha ≤ Ha_threshold |

As the results of our principle simulations showed earlier, the use of Ha concept in our modeling could present clustering prediction in extremely dilute regions of the domain. To overcome this problem, we set a constraint on Ha calculation in regards to the solid volume fraction. Table 6 shows the constraints set on the solid volume fraction and the granular temperature in our new drag model. These constraints eliminated the possibility of clustering prediction and singularity in Ha calculations in very dilute regions of the domain, where the solid volume fraction and the granular temperature were both extremely small. The optimum values for the variables listed in Table 6 were obtained by best practices. Initially, relatively small values were assigned to threshold values, which resulted in a limited variation in the numerical simulation. Later, extremely small values were selected for these variables, which resulted in a significant change in results and in some cases significant improvements in numerical results were obtained. The Ha_THS parameter was examined in a wide range for all three proposed versions of the drag model in order to find the optimum value.

**Table 6 Variation of the thresholds in the AGDSM models**

| Mode-**1** | | Mode-**2** | |
|---|---|---|---|
| Parameter | Threshold value | Parameter | Threshold value |
| $\varepsilon_s$_THS | 0.02 | $\varepsilon_s$_THS | $1\times10^{-3}$ |
| $\Theta$_THS | 0.0008 ($cm^2/s^2$) | $\Theta$_THS | $1\times10^{-16}$ ($cm^2/s^2$) |
| Ha_THS | [ $1\times10^{-5}$ - 1 ] | Ha_THS | **[**$1\times10^{-10}$ - 0.1**]** |

## Simulation results using the “Mode-1” filtration

Figure 44 shows the effect of switching operations on simulation results under the constraints of the first mode, as explained earlier in Table 6. The immediate observation from Figure 44 (a-b) is that, for various values of the Ha_THS parameter and the fixed values of $\varepsilon_s$ _THS and Θ_THS, a significant alteration in the solid volume fraction profile occurred. However, identical results were obtained for the Ha_THS parameter in a broad range of variation (e.g., [$1\times10^{-5}$ to 1]). In addition, improvement of the numerical results, in terms of deviation from the experimental data, was limited to only small portions of the computational domain in high and low sections of the riser.

Further, Figure 44(c-f) showed that the effect of filtration by the model constraints was more pronounced for AGDSM2 and AGDSM3 versions of the proposed model. According to Figure 44 (c-d) and Figure 44 (e- f) for the AGDSM2 and AGDSM3 models, respectively, no alteration of the results was observed in a significantly wider range of the Ha_THS parameter (e.g., [$1\times10^{-5}$ to $1\times10^{4}$]). In fact, the extremely conservative nature of the filtration procedure in the first mode, accounted for the unnecessary elimination of switching operations in the regions where relatively large values of Ha were detected. This observation helped to understand that, although the onset of the changes in the simulation results of the AGDSM1 model, occurred at large values of the threshold (Ha_THS = 0.05), the loss of the sensitivity to smaller values of the Ha_THS in our modeling could be overcome by significant reduction of the values for the Θ_THS and $\varepsilon_s$ _THS parameters (Mode 2 in Table 6). We referred to this treatment as “simulation with relaxed constrains” and we later showed that this treatment was effective for all versions of the proposed drag model.

## Simulation results with relaxed constrains, the “Mode-2” filtration

Simulation results with relaxed constrains, introduced as mode 2 in Table 6, are displayed in Fig. 4 for the AGDSM1, AGDSM2 and AGDSM3 versions. For brevity, we presented the best results for each proposed version of the AGDSM model. These results were selected based on the plotted error values against the Ha-THS parameter for all three versions of the proposed model in Fig. 40.

Figure 46(a-c) shows comparisons between the best cases obtained by each version of the proposed model and its corresponding original standard drag model. These result showed significant qualitative improvements of the hybrid models over their constituent standard models. Figure 46 (d) shows that all versions produced better results in comparison the results that was previously published by Hong et al. (2012). According to the Figure 46 (d), the best agreement between the $\varepsilon_s$ profile and the experimental profile occurred for the AGDSM3 model.

To support these claims, we calculated and listed the error values and optimal conditions of the models in the Table 7. This table shows that the maximum error values with the AGDSM3 model was 58.4 less than the maximum of errors calculated for the Gidaspow model, respectively.

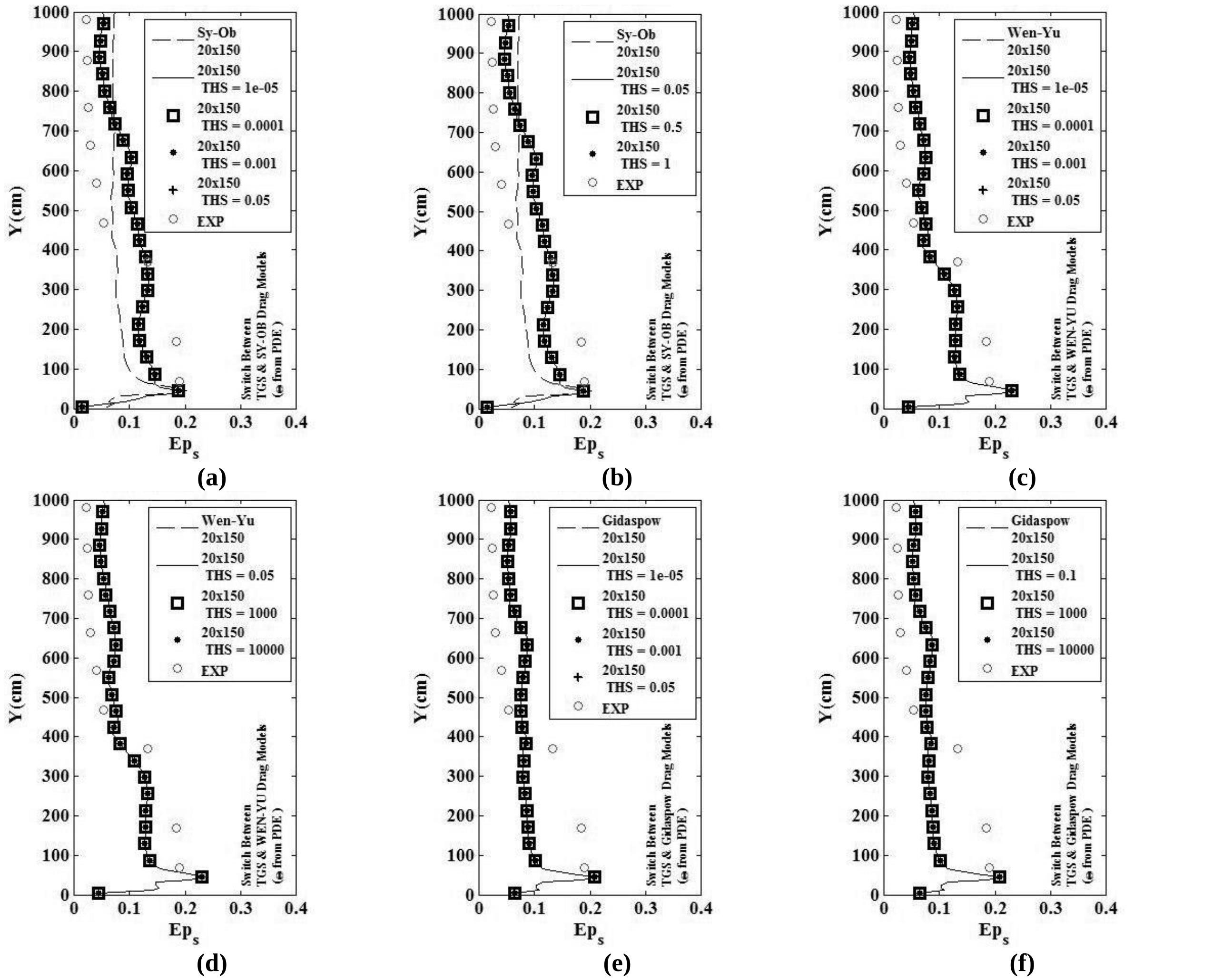


**Figure 44. Switching effects in the three versions of the AGDSM model on time and area-averaged profile of the solid volume fraction along the riser against variation of the Ha_THS.**

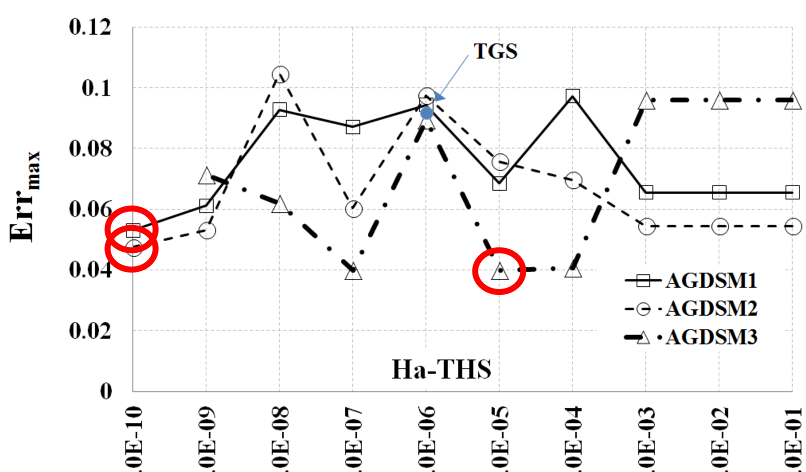


**Figure 45. Maximum error in TFM simulation for three versions of the proposed drag model, red circles show the cases with the smallest computational error for three AGDSM versions.**

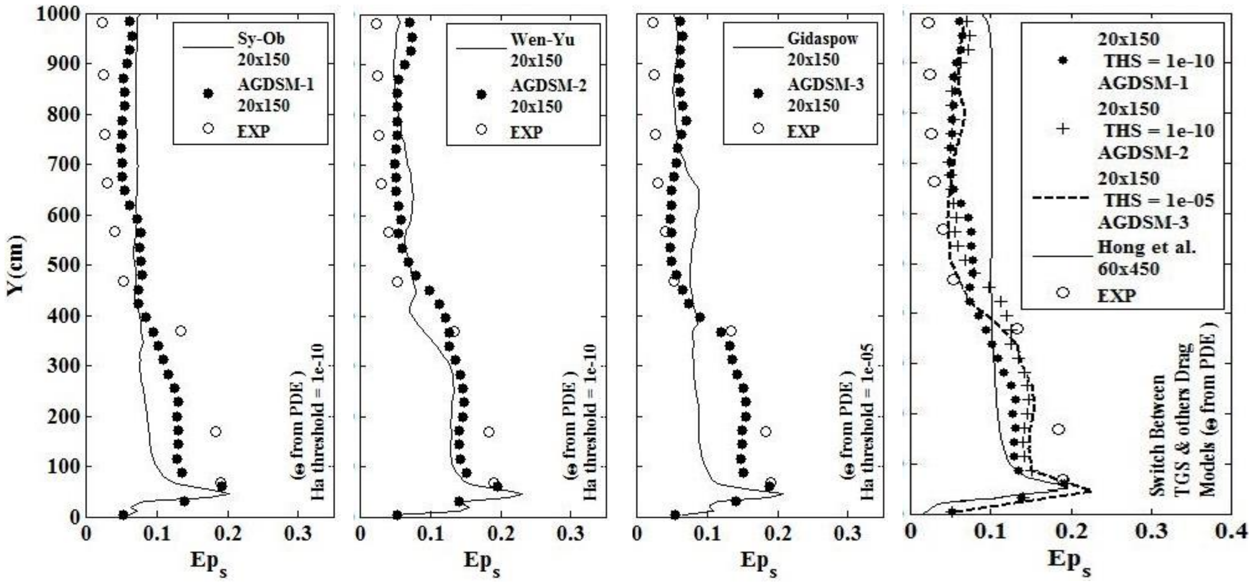


**(a)** **(b)** **(c)** **(d)**

**Figure 46. Optimal MFIX-TFM simulations by versions of the AGDSM model, (a) to (c) are versions of the AGDSM model versus corresponding standard models, (d): best result from AGDSM1-3 versions and the profile of Hong et al. (2012)**

**Table 7 Error calculations and best improvements for different versions of the AGDSM model**

| Case | Err. $_{max}$ | Err. $_{avg}$ (%) | Ha_THS | Impr. (Err. $_{max}$) |
|---|---|---|---|---|
| Hong et al. (2012) | 0.0773 | 166.1 | - | - |
| Syam-O'Brien | 0.0954 | 106.2 | - | % 44.5 |
| Gidaspow | 0.0959 | 93.5 | - | % 58.4 |
| Wen-Yu | 0.0545 | 77.4 | - | % 12.9 |
| TGS | 0.0918 | 143.1 | - | % 56.5 |
| AGDSM 1 | 0.0531 | 74.5 | $1\times10^{-10}$ | - |
| AGDSM 2 | 0.0474 | 71.6 | $1\times10^{-10}$ | - |
| AGDSM3 | 0.0399 | 67.2 | $1\times10^{-5}$ | - |

## Drag force for clustered particles

Extensive DNS simulations of air-particle flows in the presence of strong cohesive inter-particle forces were performed. The purpose of this investigation was to obtain a relation between clustered drag and the uniform drag, as described by Equation 13.

$$\frac{F_{Cl}}{F_U} = g(\phi, \mathrm{Re}_m)$$ **Equation 13**

The immediate results from simulations in Ø = 0.087 and for Reynolds number of particles varying in the range of 0 to 60 is shown in Figure 47. These results showed that in the case of clustered configurations, drag force was decreased significantly from drag force of a uniform particle configuration. The fitted curve through the values of drag force of clustered configurations (blue triangles) had the form shown by Equation 14.

$$g(Re_m) = \frac{164.543 + 0.8045\, Re_m^{\;1.6292}}{305.9554 + Re_m^{\;1.6292}} \qquad \textbf{Equation 14}$$

A hybrid-type drag model for clustered particles based on switching between a uniform drag law and the clustered drag law was formulated in Table 8. This proposed model was named as AGDSM-11. In this proposed drag law, the Syam-O'Brien drag model was used as the base/uniform model. Simulations with different threshold numbers of the cohesive index, Ha_THS, were performed and we compared the results of the AGDSM_1 and AGDSM_11 models at Ha_THS = 1e-10 in Figure 48. The results showed that application of clustering could help in significant reduction of the computational error in dense regions of the riser ($0 \leq z < 486$cm). Quantitative comparison of computational error is available in Table 8, which shows that maximum and relative errors associated with the cluster model (AGDSM_11) were significantly lower in comparison to the AGDSM_1 model. The relative error in this region was below 9 percent for the AGDSM_11 model and 30 percent for the AGDSM_1 model. However, the cluster model needs more tuning to improve the modeling in the dilute region of the riser. Hence, more effort is needed to obtain drag coefficients for various values of solid volume fraction ($0 \leq \Phi \leq 0.2$).

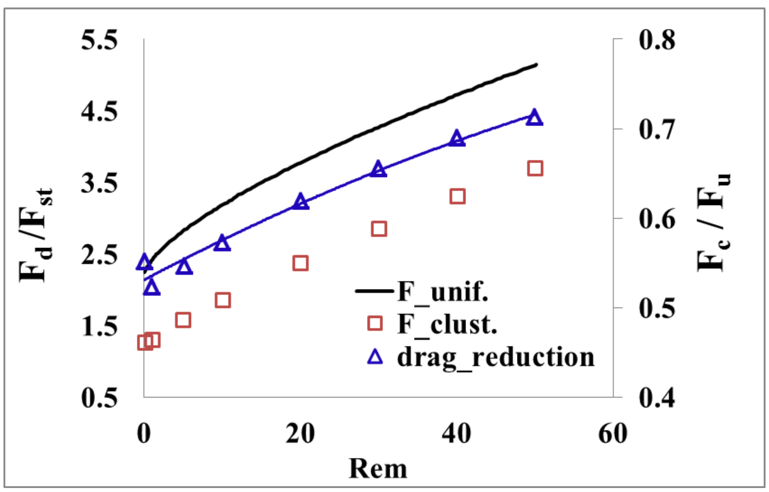


**Figure 47. Comparison of average drag force per particle between the uniform and clustered particle assemblies. The symbols (□) show the drag force on clustered configurations while the solid black line represents the uniformly distributed particles drag model of Tenneti et al (2012). These two quantities are measured with respect to the left vertical axis. The symbols (▿) show the $F_{cl}/F_u$ ratio, which is measured with respect to the right vertical axis.**

**Table 8. Drag law for clustered particles**

| Model | Arguments | Condition |
|---|---|---|
| AGDSM-11 | Use g(Re,ø)*(Syam-O'Brien) | Ha > Ha_threshold |
| | Use Syam-O'Brien only | Ha ≤ Ha_threshold |

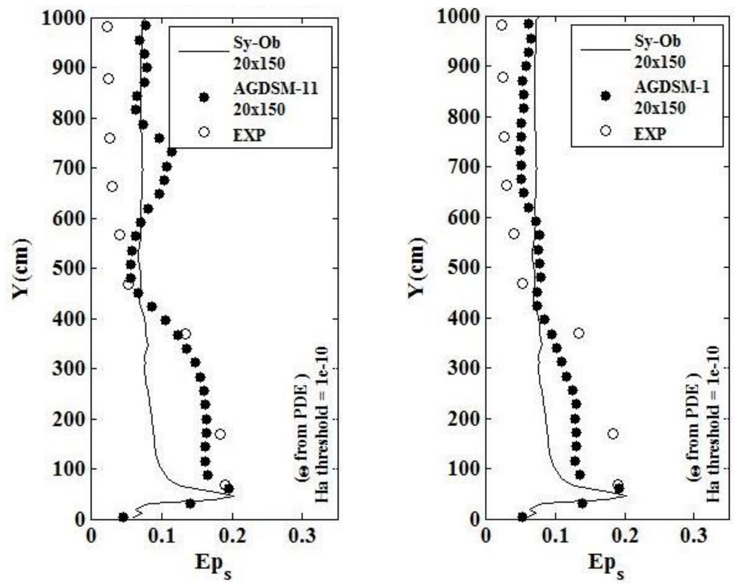


**Figure 48. Utilization of hybrid models, cluster-aware drag model (AGDSM11, Syam-O'Brien ⇋ g(Re,ø) * Syam-O'Brien ) on left, and AGDSM_1 (TGS ⇋ Syam-O'Brien) on the right**

**Table 9 Error calculations and improvements for AGDSM_1 and the cluster model (AGDSM_11)**

| Case | Err. $_{max}$ $0 \leq z < 1000$* | Err. $_{max}$ $0 \leq z < 486$* | Err. $_{avg}$ (%) $0 \leq z < 1000$* | Err. $_{avg}$ (%) $0 \leq z < 486$* | Ha_THS | Impr. (Err. $_{max}$) | Impr. (Err. $_{rel}$) |
|---|---|---|---|---|---|---|---|
| Syam-O'Brien | 0.0954 | 0.0954 | 106.2 | 40.05 | - | - | - |
| AGDSM_1 | 0.0531 | 0.0531 | 74.5 | 29.15 | $1\times10^{-10}$ | % 44.5 | % 29.8 |
| AGDSM_11 | 0.053 | 0.0207 | 119.33 | 8.87 | $1\times10^{-10}$ | % 17.5 | % 28.4 |

***** Units are in centimeters

# Conclusions

In this research the circulating fluidized bed (CFB) at FIU was modified in regards to safe operation, measurement and data acquisition, and solid feeding mechanism aspects. Velocity profile above the separation plate, pressure measurements along the riser of the CFB, and high speed imaging of FCC were conducted in the CFB test unit. The CFB is complete for future testing in any regimes of fluidization; however, advanced imaging techniques such as optical probe or X-ray photography are required to obtain high resolution images from the particles clusters in the freeboard region of the CFB riser the FIU. In addition, high standard data collection in the CFB requires more advanced electrostatic charge removal techniques, such as UV light emission, and advanced solid flux rate indication methods.

Our bubbling test setup was used to collect useful data and images. Using this test rig, we performed imaging from polystyrene and FCC particles, our minimum fluidization experiment, electrostatic charge removal test, and transducer verification tests in very small pressure increments.

In addition, we successfully implemented the drag model TGS and performed series of numerical simulations in the MFIX program. Our simulation results of a pilot flow with available experimental data showed that simulations using one model, i.e., any of the standard drag models and the TGS model, failed to agree closely with the available experimental data.

On the other hand, combining a standard drag model with the TGS model, under optimized conditions and based on a switching mechanism, was proved to be a useful method to significantly improve the accuracy of the numerical results. In this approach, the switching mechanism proved to be exceptionally sensitive to the variation of the threshold values of the cohesive index, Ha-THS. In addition, this approach was observed to be successful for all versions of the proposed drag model under optimal conditions, where a maximum of almost 60 percent improvement in accuracy of simulation results was obtained for the Gidaspow model. Therefore, a direct or indirect implementation of particle clustering and ensuing modifications in the TFM approach is necessary to be practiced for gas-solid flows under the influence of cohesive inter-particle forces. The results indicate that an optimization approach utilizing simulated annealing method was an appropriate tool to reproduce particle configurations with specified first and second order statistical quantities.

Implementation of the Ha as switching criteria in combination with a modification to the standard model was recognized as a hybrid model suitable for cluster configurations. We obtained significant improvements in the dense region of the computational domain where a 78.3 percent improvement of compared to the original standard model could be obtained. However, the improvement in the entire domain was not higher than the other proposed models and more comprehensive data from the PR-DNS simulations was needed to better tune the cluster drag model.

For future investigation, the authors would like to extend the current work to finding a correlation between the cohesive index and the drag force in various TFM simulations including the flow under the present investigation. Further, the profitability of the Ha concept and the concept of switching to the TGS drag correlation will be tested in direct element method in parallel simulations.

# References

Andrews IV. A. T., Loezos P. N., Sundaresan S., 2005. Coarse-Grid Simulation of Gas-Particle Flows in Vertical Risers, Industrial & Engineering Chemistry Research, Volume 44, Issue 16, 6022–6037.

Beetstra R., Van Der Hoef M.A., Kuipers J.A.M, 2007, Drag Force of Intermediate Reynolds Number Flow Past Mono- and Bidisperse Arrays of Spheres, AIChEJ Journal, Volume 53, Issue 2, 489-501

Benyahia S., 2008, Verification and validation study of some polydisperse kinetic theories, Journal of Chemical Engineering Science, Volume 63, Issue 23, 5672–5680

Benyahia S., 2012, Analysis of Model Parameters Affecting the Pressure Profile in a Circulating Fluidized Bed, AIChE Journal, Volume 58, Issue 2, 427-429

Bokkers G. A., Laverman, J. A.,van Sint Annaland, M., Kuipers, J. A. M., 2006, Modelling of large-scale dense gas-solid bubbling fluidized beds using a novel discrete bubble model, Journal of Chemical Engineering Science, Volume 61, Issue 17, 5590–5602

Bona Lu, Wei Wanga, Jinghai Lia, 2009, Searching for a Mesh-Independent Sub-Grid Model for CFD Simulation of Gas–Solid Riser Flows, Journal of Chemical Engineering Science, Volume 64, Issue 15, 3437- 3447

Brereton, C. M. H., Grace, J. R., (1993), "Microstructural aspects of the behavior of circulating fluidized beds," Chem. Eng. Sci. 48, pp. 2565–2572.

Cao, J., Ahmadi, G., (1995), "Gas-particle two-phase turbulent flow in a vertical duct," Int. J. Multiphase Flow, 21, pp. 1203–1228.

Cho S.H., Choi H.G., Yoo J.Y. 2005, Direct Numerical Simulation of Fluid Flow Laden with Many Particles, International Journal of Multiphase Flow, Volume 31, Issue 4, Pages 435–451

Clayton Crowe, Martin Sommerfeld and Yutaka Tsuji, 1998, Multiphase flows with droplets and particles, CRC Press LLC.

Dejin, L., Kwauk, M., Hongzhong, L., (1996), "Aggregative and particulate fluidization - the two extremes of a continuous spectrum," Chem. Eng. Sci., 51, pp. 4045–4063.

Ding, J., Gidaspow, D., (1990), "A bubbling fluidization model using kinetic theory of granular flow," AIChE Journal, 36, p. 523.

Dombrowski N., Johns W. R., 1963, The Aerodynamic Instability and Disintegration of Viscous Liquid Sheets, Journal of Chemical Engineering Science, Vol. 18, Issue 3, 203-214

Ellis N., 2003, Hydrodynamics of Gas-Solid turbulent fluidized beds, Ph.D. thesis, University of British Colombia, Vancouver, Canada

Ergun S., 1952, Fluid flow through packed columns, Chemical Engineering Progress Symposium Series, Volume 48, Issue 2, 89–94.

Garg R., Tenneti S., Yusof J.M., 2011, and Subramaniam S., Direct Numerical Simulation of Gas-Solids Flow Based on the Immersed Boundary Method, Computational Gas-Solids Flows and Reacting Systems: Theory, Methods and Practice, IGI global disseminator of knowledge

Gidaspow D., 1994, Multiphase Flow and Fluidization: Continuum and Kinetic Theory Descriptions with Applications. Academic Press, Boston, 315-316

Gidaspow, D., Huilin, L., (1998), "Equation of state and radial distribution functions of FCC particles in a CFB," AIChE Journal, 44, p. 279.

Hartge, E. U., Rensnet, D., Werther, J., (1988), "Solids concentration and velocity patterns in circulating fluidized beds", in: P. Basu, J.F. Large (Eds.), Circulating Fluidized Bed Technology II, Pergamon, New York, pp. 165–180.

Helland, E., Occelli, R., Tadrist, L., (2000), "Numerical study of cluster formation in a gas-particle circulating fluidized bed," Powder Technology, 110, pp. 210–221.

Hill, R.J., Koch D.L., Ladd, A.J.C., 2001a, The First Effects of Fluid Inertia on Flows in Ordered and Random Arrays of Spheres. Journal of Fluid Mechanics, Volume 448, 213–241

Hill R.J., Koch D.L., Ladd A.J.C., 2001b, Moderate-Reynolds-Number Flows in Ordered and Random Arrays of Spheres, J. of Fluid Mechanics, Volume 448, 243-278

Hong K., Wang W., Zhou Q., Wang J., Li J., 2012, An EMMS-Based Multi-Fluid Model (EFM) for Heterogeneous Gas–Solid Riser Flows: Part I. Formulation of Structure-Dependent Conservation Equations, Journal of Chemical Engineering Science, Volume 75, 376–389

Hoomans, B.P.B., Kuipers, J.A.M., Briels, W.J.W., Van Swaaij, P.M., (1996) "Discrete particle simulation of bubble and slug formation in a two-dimensional gas-fluidized bed: a hard-sphere approach," Chem. Eng. Sci., 51, pp. 99–118.

Horio, M., Morshita, K., Tachibana, O., Murata, M., (1988), "Solid distribution and movement in circulating fluidized beds," P. Basu, J.F. Large (Eds.), Circulating Fluidized Bed Technology II, Pergamon, New York.

Hu H.H., Patankar N.A., Zhu, M.Y., 2001, Direct numerical simulations of fluid-solid systems using the arbitrary Lagrangian–Eulerian technique. Journal of Computational Physics, Volume 169, Issue 2, 427–462

Igci Y., Pannala S., Benyahia S., & Sundaresan S. ,2012, Validation Studies on Filtered Model Equations for Gas-Particle Flows in Risers, Industrial & Engineering Chemistry Research, Volume 51, Issue 4, 2094-2103

Israelachvili J., 1991, Intermolecular and Surface Forces, Academic Press, London, UK, 3rd edition, ISBN 978-0-12-375182-9 (ALK. paper)

Ito, M., Tsukada, M., Shimamura, J., Horio, M., (1998), "Prediction of cluster size and slip velocity in circulating fluidized beds by a DSMC model," Fan, L.S., Knowlton, T.M. (Eds.), Fluidization IX. Engineering Foundation Inc., New York, pp. 525–532.

Jenkins JT, Zhang C., 2002, Kinetic theory for identical, frictional, nearly elastic spheres, Phys Fluids. Volume 14, 1228–1235

Karimipour S., Pugsley T., 2012, Application of the Particle in Cell Approach for the Simulation of Bubbling Fluidized Beds of Geldart A Particles, Journal of Powder Technology, Volume 220, 63–69

Liang-Shih Fan and Chao Zhu, 1998, Principles of Gas-Solid Flows, Cambridge Series in Chemical Engineering.

Li J., Ge W., Wang W., Yang N., Liu X., Wang L., He X., Wang X., Wang J., Kwauk M., 2013, From Multiscale Modeling to Meso-Science, A Chemical Engineering Perspective Principles, Modeling, Simulation, and Application, Springer Heidelberg New York Dordrecht London, Library of Congress Control Number: 2012954048, DOI 10.1007/978-3-642-35189-1

Li J., Kwauk M., 1994, Particle-Fluid Two Phase Flow, The Energy Minimization Multiscale Method, Metallurgy Industry Press, Beijing

Liu X., Xu X., Zhang W., 2006, Numerical simulation of dense particle gas two-phase flow using the minimal potential energy principle. Journal of University Science and Technology Beijing, Mineral, Metallurgy, Material, Volume 13, Issue 4, 301–307.

Lu B., Wang W., Li J., 2009, Searching for a mesh-independent sub-grid model for CFD simulation of gas-solid riser flows, Journal of Chemical Engineering Science, Volume 64, Issue 15, 3437-3447

Lun, C., Savage, S., Jeffery, D., and Chepurnity, N., (1984), "Kinetic theory for granular flow: Inelastic particles in Coutte flow and slightly inelastic particles in a granular flowfield," Journal of Fluid Mechanics, 140, pp. 223.

Ma J., Ge, W., Wang X., Wang, J. Li J. 2006, High-Resolution Simulation Of Gas–Solid Suspension Using Macro-Scale Particle Methods, Journal of Chemical Engineering Science, Volume 61, Issue 21, 7096 –7106

McKeen T., Pugsley T., 2003, Simulation and Experimental Validation of a Freely Bubbling Bed of FCC Catalyst, Journal of Powder Technology, Volume 129, Issues 1-3, 139–152

Mikami, T., Kamiya, H., & Horio, M., 1998, Numerical simulation of cohesive powder behaviour in a fluidized bed, Chemical Engineering Science, Volume 53, Issue 10, 1927-1940

Milioli, C. C., Milioli F. E., Holloway W., Agrawal, K., Sundaresan S., 2013, Filtered Two-Fluid Models of Fluidized Gas-Particle Flows: New Constitutive Relations, AIChE Journal, Volume 59, Issues 9, 3265–3275,

Nguyen, N.Q., Ladd, A.J.C., 2005, Sedimentation of Hard-Sphere Suspensions at Low Reynolds Number. Journal of Fluid Mechanics (2005) 525, 73

Nomura, T., Hughes, T.J.R., 1992. An arbitrary Lagrangian–Eulerian finite element method for interaction of fluid and a rigid body. Journal of Computer Methods in Applied Mechanics and Engineering, Volume 95, Issue 1, 115–138

Noymer, D. P., Glicksman, L. R., (1998), "Cluster motion and particle-convective heat transfer at the wall of a circulating fluidized bed," Int. J. Heat Mass Transfer, 41, pp. 147–158.

Ouyang, J., Li, J., (1999), "Discrete simulations of heterogeneous structure and dynamic behavior in gas–solid fluidization," Chem. Eng. Sci., pp. 5427–5440.

Pannala S., Syamlal M., O'Brien T. J., 2011, Computational Gas-Solids Flows and Reacting Systems: Theory, Methods and Practice, ISBN-13: 978-1615206513, Engineering Science Reference

Qi H.Y., Li F., Xi B, You C., 2007. Modeling of Drag with the Eulerian Approach and EMMS Theory for Heterogeneous Dense Gas–Solid Two-Phase Flow, Journal of Chemical Engineering Science, Volume 62, Issue 6, 1670–1681

Samuelsberg A., Hjertager B.H., 1996, Computational Modeling of Gas/Particle Flow in a Riser, AIChE Journal, Volume 42, Issue 6, 1536-1546

Schiller L., Naumann A., 1935. A Drag Coefficient Correlation, VDI Zeitung publications, Volume 77, 1935, 318-320.

Seville J.P.K., Willett C.D., Knight P.C., 2000, Interparticle Force in Fluidization: a review, J. of Powder Technology, Volume 113, Issue 3, 261-268

Sharma N., Patankar N., 2005, A fast computation technique for the direct numerical simulation of rigid particulate flows, Journal of Computational Physics, Volume 205, Issue 2, 439–457

Sharma, K. A., Tuzla, K., Matsen, J., Chen, J. C., (2000), “Parametric effects of particle size and gas velocity on cluster characteristics in fast fluidized beds,” Powder Technology, 111, pp. 114-122.

Sinclair, J.L., Jackson, R., (1989), “Gas–particle flow in a vertical pipe with particle–particle interactions,” AIChE Journal, 35, p. 1473.

Soong, C. H., Tuzla, K., Chen, J. C., (1993), “Identification of particle clusters in circulating fluidized beds,” in: A.A. Avidan (Ed.), Circulating Fluidized Bed Technology IV Engineering Foundation, New York, pp. 615–620.

Spahn, F., Schwarz, U., and Kurths, J., (1997), “Clustering of granular assemblies with temperature dependent restitution under Keplerian differential rotation,” Physical Review Letters, 78, pp. 1596-1599.

Syamlal M., Rogers W., O’Brien T.J, 1993, MFIX Documentation; Theory Guide, Technical Note, U.S. Department of Energy, Office of Fossil Energy, Morgantown Energy Technology Center, Morgantown, West Virginia

Syamlal M., Rogers W., O'Brien T.J., 1993, MFIX Documentation: Volume 1, Theory Guide, National Technical Information Service, Springfield, VA, Appendix A

Syamlal M., O’Brien T. J., 2003, Fluid Dynamic Simulation of O3 Decomposition in 3 a Bubbling Fluidized Bed, AIChE Journal, Volume 49, Issue 11, 2793-2801

Tenneti S., Garg R., Subramaniam S., 2011, Drag Law for Monodisperse Gas–solid Systems Using Particle-resolved Direct Numerical Simulation of Flow Past Fixed Assemblies of Spheres, International Journal of Multiphase Flow, Volume 37, Issue 9, 1072-1092

Tenneti S., Subramaniam S., 2013, Particle-Resolved Direct Numerical Simulation for Gas-Solid Flow Model Development, Annual Review of Fluid Mechanics, Volume 46, 199-230

Tsuo, Y. P., Gidaspow, D., (1990), “Computation of flow patterns in circulating fluidized beds,” AIChE Journal, 36, p. 885.

Tsuji, Y., Kawaguchi, T., Tanaka, T., (1993), “Discrete particle simulation of two-dimensional fluidized bed,” Powder Technology, 77, pp. 79–87.

Van Deemter, J. J., van der Laan, E. T., ,1961, Momentum And Energy Balances for Dispersed Two-Phase Flow, Journal of Applied Sciences Research , Section A, Volume 10, 102-108

van der Hoef M.A., van Sint Annaland M., Deen N.G., Kuipers J.A.M., 2008, Numerical Simulation of Dense Gas-Solid Fluidized Beds: A Multiscale Modeling Strategy, Annual Review of Fluid Mechanics, Volume 40, 47-70

van der Hoef M.A., Beetstra R., Kuipers J.A.M., 2005. Lattice-Boltzmann Simulations of Low-Reynolds-Number Flow Past Mono- and Bidisperse Arrays of Sphere: Results for the Permeability and Drag Force, Journal of Fluid Mechanics, Volume 528, 233–254

Van Wachem, B.G.M., Schouten, J.C., Van den Bleek, C.M., Krishna, R., Sinclair, J.L., (2001), “CFD modeling of gas fluidized beds with a bimodal particle mixture,” AIChE J., pp. 1292–1301.

Van Wachem, B.G.M., Van der Schaff, J., Schouten, J.C., Krishna, R., Van den Bleek, C.M., (2001), “Experimental validation of Lagrangian–Eulerian simulations of fluidized beds,” Powder Technology, 116, pp. 155–165.

Wen C. Y., Yu Y. H., 1966, Mechanics of Fluidization, Chemical Engineering Progress Symposium Series, Volume 62, Issue 1, 100–111

Wang J., Ge W., Li J., 2008, Eulerian Simulation Of Heterogeneous Gas–Solid Flows in CFB Risers: EMMS-based Sub-Grid Scale Model with a Revised Cluster Description, Journal of Chemical Engineering Science, Volume 63, Issue 6, 1553-1571

Wang J., 2009, A Review of Eulerian Simulation of Geldart A Particles in Gas-Fluidized Beds, Journal of Industrial and Engineering Chemistry Research, volume 48, Issue 12, 5567-5577

Wang W., Li J., 2007, Simulation of Gas–solid Two-phase Flow by a Multiscale CFD Approach: Extension of the EMMS Model to the Sub-grid Scale Level, Journal of Chemical Engineering Science, Volume 62, Issues 1-2, 208–231.

Xion Q., Li B., Zhou G., Fang X., Xu J., Wang J., He X., Wang X., Wang L. , Ge W., Li J., 2012, Large-scale DNS of Gas–Solid Flows on Mole-8.5, Journal of Chemical Engineering Science, Volume 71, 422–430

Xu M., Chen F., Liu X., Ge W., Li J., 2012, Discrete Particle Simulation of Gas–Solid Two-Phase Flows with Multi-scale CPU–GPU Hybrid Computation, Journal of Chemical Engineering, Volumes 207-208, 746–757

Yang N., Wang W., Ge W., Li J., 2003, CFD Simulation of Concurrent-up Gas–Solid Flow in Circulating Fluidized Beds with Structure-Dependent Drag Coefficient, Journal of Chemical Engineering, Volume 96, Issues 1-3, 71-80

Ye M., van der Hoef M.A., Kuipers J.A.M., 2005a, From Discrete Particle Model To A Continuous Model of Geldart A Particles, Journal of Chemical Engineering Research and Design, volume 83, issue 7, 833–843

Ye M.A, van der Hoef M.A., Kuipers J.A.M., 2005b, The Effects of Particle and Gas Properties on the fluidization, Journal of Chemical Engineering Science, Volume 60, Issue 16, 4567- 4580

Ye M. A., van der Hoef M.A., Kuipers J.A.M, 2008, Two-fluid modeling of Geldart A particles in gas-fluidized beds, Journal of Particuology, Volume 6, Issue 6, 540–548

Ye M. A., van der Hoef M.A., Kuipers J.A.M, 2009, Why the Two-Fluid Model Fails to Predict the Bed Expansion Characteristics of Geldart A Particles in Gas-Fluidized Beds: A tentative answer, Journal of Chemical Engineering Science, Volume 64, Issue 3, 622-625

Yin X., Sundaresan S., 2009, Drag Law for Bidisperse Gas–Solid Suspensions Containing equally sized spheres, Journal of Industrial and Engineering Chemistry Research, Volume 48, Issue 1, 227–241

Yerushalmi, J., Glicksman, M. J., Graff, R. A., Dobers, S., Squires, A. M., (1975), “Production of gaseous fuels from coal in the fast fluidized bed,” Fluid. Technol., pp. 437–469.

Zhang D.Z., Vanderheyden W.B., 2002, The Effects of Mesoscopic Structures on the Macroscopic Momentum Equations for Two-Phase Flows. International Journal of Multiphase Flow, Volume 28, Issue 5, 805–822

Zhou, H., Flamant, G., Gauthier, D., Lu, J., (2002), “Lagrangian approach for simulating the gas-particle flow structure in a circulating fluidized bed riser,” Int. J. Multiphase Flow, 28, pp. 1801–1821

Zou L. M., Guo Y. C., Chan C. K., 2008, Cluster-based drag coefficient model for simulating gas-solid flow in a fast-fluidized bed, Journal of Chemical Engineering Science, Volume 63, Issue 4, 1052–1061

## Milestone Status

Project Gantt Chart (Table 1) illustrates the progress toward completing the project tasks.

**Table 10** Project Gantt Chart (simplified)

| Milestone # | Milestone Description | Planned Completion Date | Revised Completion Date | Actual Completion Date | Comments |
|---|---|---|---|---|---|
| 1 | Conduct full system shakedown of the circulating fluidized bed set-up | 04/13/12 | 07/01/2012 | 6/31/12 | Completed |
| 2 | Complete the image analysis and experimental data processing | 04/12/2013 | 07/12/2013 | 7/12/2013 | Completed |
| 3 | Develop drag laws to account for particle clustering effects | 10/21/2013 | 10/21/2013 | 10/21/2013 | Completed |
| 4 | Validate the MFIX results against the experimental data | 09/29/2014 | 09/29/2014 | 9/29/14 | Completed |

## Project Budget Status

Table 8 illustrates the cost status of the project for this reporting period.

The cumulative expenditures amount to $220,232.40 versus the baseline estimate of cumulative cost is $221,630. A no-cost extension has been requested until January 1, 2015 which has been granted by NETL.

**Table 11 Project Cost Status.**

| Baseline Reporting Quarter | Budget Period 1 | | | | | | | |
|---|---|---|---|---|---|---|---|---|
| | Q1 | | Q2 | | Q3 | | Q4 | |
| | 10/1/2011 - 12/31/11 | | 01/1/2012 - 03/31/11 | | 04/1/2012 - 6/30/12 | | 07/1/2012 - 09/30/12 | |
| | Q1 | Cumulative Total | Q2 | Cumulative Total | Q3 | Cumulative Total | Q4 | Cumulative Total |
| **Baseline Cost Plan** | | | | | | | | |
| Federal Share | $20,606.18 | $20,606.18 | $13,356.18 | $33,962.36 | $11,906.18 | $45,868.54 | $13,356.18 | $59,224.72 |
| Non-Federal Share | $1,858.86 | $1,858.86 | $1,858.86 | $3,717.72 | $1,858.86 | $5,576.58 | $1,858.86 | $7,435.44 |
| Total Planned | $22,465.04 | $22,465.04 | $15,215.04 | $37,680.08 | $13,765.04 | $51,445.12 | $15,215.04 | $66,660.16 |
| **Actual Incurred Cost** | | | | | | | | |
| Federal Share | $776.66 | $776.66 | $5,107.19 | $5,883.85 | $13,439.54 | $19,323.39 | $21,193.61 | $40,517.00 |
| Non-Federal Share | $0.00 | $0.00 | $0.00 | $0.00 | $0.00 | $0.00 | $3,161.79 | $3,161.79 |
| Total Incurred Costs | $776.66 | $776.66 | $5,107.19 | $5,883.85 | $13,439.54 | $19,323.39 | $24,355.40 | $43,678.79 |
| **Variance** | | | | | | | | |
| Federal Share | $19,829.52 | $19,829.52 | $8,248.99 | $28,078.51 | -$1,533.36 | $26,545.15 | -$7,837.43 | $18,707.72 |
| Non-Federal Share | $1,858.86 | $1,858.86 | $1,858.86 | $3,717.72 | $1,858.86 | $5,576.58 | -$1,302.93 | $4,273.65 |
| Total Variance | $21,688.38 | $21,688.38 | $10,107.85 | $31,796.23 | $325.50 | $32,121.73 | -$9,140.36 | $22,981.37 |

| Budget Period 2 | | | | | | | |
|---|---|---|---|---|---|---|---|
| Q1 | | Q2 | | Q3 | | Q4 | |
| 10/1/2012 - 12/31/12 | | 01/1/2013 - 03/31/12 | | 04/1/2013 - 6/30/13 | | 07/1/2013 - 09/30/13 | |
| Q1 | Cumulative Total | Q2 | Cumulative Total | Q3 | Cumulative Total | Q4 | Cumulative Total |
| | | | | | | | |
| $71,915.81 | $138,575.97 | $8,022.81 | $146,598.78 | $10,197.81 | $156,796.59 | $8,022.81 | $164,819.41 |
| $1,858.86 | $9,294.30 | $1,858.86 | $11,153.16 | $1,858.86 | $13,012.02 | $1,858.86 | $14,870.88 |
| $73,774.67 | $147,870.27 | $9,881.67 | $157,751.94 | $12,056.67 | $169,808.61 | $9,881.67 | $179,690.29 |
| | | | | | | | |
| $19,196.33 | $59,713.33 | $37,505.54 | $97,218.87 | $21,460.61 | $118,679.48 | 19,903.29 | $138,582.77 |
| $3,161.79 | $6,323.58 | $3,161.79 | $9,485.37 | $2,107.86 | $11,593.23 | $3,161.79 | $14,755.02 |
| $22,358.12 | $66,036.91 | $40,667.33 | $106,704.24 | $23,568.47 | $130,272.71 | $23,065.08 | $153,337.79 |
| | | | | | | | |
| $52,719.48 | $78,862.64 | -$29,482.73 | $49,379.91 | -$11,262.80 | $38,117.11 | -$11,880.48 | $26,236.64 |
| -$1,302.93 | $2,970.72 | -$1,302.93 | $1,667.79 | -$249.00 | $1,418.79 | -$1,302.93 | $115.86 |
| $51,416.55 | $81,833.36 | -$30,785.66 | $51,047.70 | -$11,511.80 | $39,535.90 | -$13,183.41 | $26,352.50 |

| Budget Period 3 | | | | | | | |
|---|---|---|---|---|---|---|---|
| Q1 | | Q2 | | Q3 | | Q4 | |
| 10/1/2013 - 12/31/13 | | 01/1/2014 - 03/31/14 | | 04/1/2014 - 6/30/14 | | 07/1/2014 - 09/30/14 | |
| Q1 | Cumulative Total | Q2 | Cumulative Total | Q3 | Cumulative Total | Q4 | Cumulative Total |
| | | | | | | | |
| $8,082.32 | $172,901.73 | $8,082.32 | $180,984.05 | $10,257.32 | $191,241.37 | $8,082.32 | $199,323.69 |
| $1,858.86 | $16,729.74 | $1,858.86 | $18,588.60 | $1,858.86 | $20,447.46 | $1,858.86 | $22,306.32 |
| $9,941.18 | $189,631.47 | $9,941.18 | $199,572.65 | $12,116.18 | $211,688.83 | $9,941.18 | $221,630.01 |
| | | | | | | | |
| $15,012.72 | $153,595.49 | $12,845.40 | $166,440.89 | $12,887.05 | $179,327.94 | $15,610.14 | $194,938.08 |
| $3,161.79 | $17,916.81 | $3,161.79 | $21,078.60 | $2,107.86 | $23,186.46 | $2,107.86 | $25,294.32 |
| $18,174.51 | $171,512.30 | $16,007.19 | $187,519.49 | $14,994.91 | $202,514.40 | $17,718.00 | $220,232.40 |
| | | | | | | | |
| -$6,930.40 | $19,306.24 | -$4,763.08 | $14,543.16 | -$2,629.73 | $11,913.43 | -$7,527.82 | $4,385.61 |
| -$1,302.93 | -$1,187.07 | -$1,302.93 | -$2,490.00 | -$249.00 | -$2,739.00 | -$249.00 | -$2,988.00 |
| -$8,233.33 | $18,119.17 | -$6,066.01 | $12,053.16 | -$2,878.73 | $9,174.43 | -$7,776.82 | $1,397.61 |

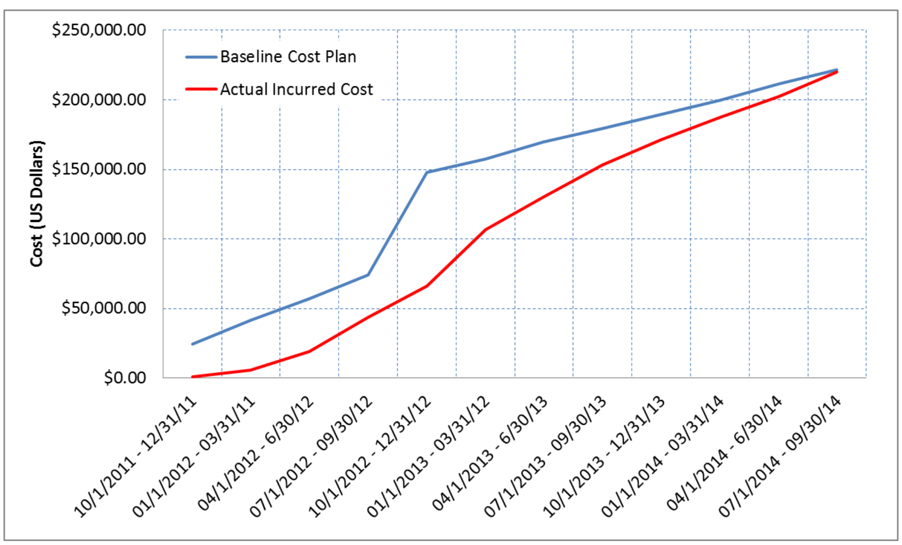

# Appendix

**Table Ap. 1 MSDS data sheet for the FCC particle obtained from Catalysts Inc.**

## Material Data Safety Sheet
### EQUILIBRIUM CATALYST, INC.

### SECTION I - IDENTIFICATION

| | |
|---|---|
| PRODUCT NAME | ISSUE DATE/ REVISION DATE |
| EQUILIBRIUM CATALYST (SPENT FLUID CRACKING CATALYST) | January 5th, 2011 |
| Supplier | EMERGENCY PHONE NUMBER |
| EQUILIBRIUM CATALYST, INC. (ECI) | 1-800-424-9300 Chemtrec |
| ADDRESS | INFORMATION PHONE NUMBER |
| PO Box 73312 Metairie, LA 70033 | 1-504-836-5040 |
| HAZARDOUS MATERIAL DESCRIPTION, PROPER SHIPPING NAME, HAZARD CLASS, HAZARD ID NO. (49 CFR 172.101) | ADDITIONAL HAZARD CLASSES |
| NOT REGULATED FOR TRANSPORTATION | NONE |
| CHEMICAL FAMILY & SYNONYMS | CHEMICAL FORMULA |
| ALUMINUM OXIDE/SILICA OXIDE | $AL_2O_3$*X $H_2O$ |

### SECTION II - HAZARDOUS INGREDIENTS

| CAS REGISTRY NUMBER | RTECS REGISTRY NUMBER | % WT | CHEMICAL NAMES | OSHA PEL TOTAL mg/m³ | ACGIH TLV TOTAL mg/m³ | OTHER LIMITS Respirable mg/m³ | Listed as carcinogen NTP, IARC, or OSHA 1910 (z) (specify) |
|---|---|---|---|---|---|---|---|
| 7631-86-9 | VV7322000 | 25-80 | Silica (Synthetic $SiO_2$) | 6 | 10 | N.E. | No |
| 1344-28-1 | BK1200000 | 20-75 | Alumina ($Al_2O_3$) | 10 | 10 | 5(OSHA) | No |
| 112926-00-8 | VV7322000 | 20-75 | Silica Gel | 6 | 10 | N.E. | No |
| 60676-86-0 | OF7525000 | 1.0 (max) | Quartz | 0.1 | N.E. | N.E. | IARC (2B), NTP |
| Not Listed | N.E. | 0.1-2.5 | Sulfate | N.E. | N.E. | 0.1(ACGIH) | No |
| 68188-83-0 | N.E. | 0.1-10 | Rare Earths ($RE_2O_3$) | N.E. | N.E. | N.E. | Yes |
| 13463-67-7 | VV7328000 | 0.1-3.0 | Titanium Dioxide ($TiO_2$) | N.E. | 10 | N.E. | No |
| 1313-59-3 | XR2275000 | 0.2-1.5 | Sodium Oxide ($Na_2O$) | N.E. | N.E. | N.E. | No |
| 7440-44-0 | WC4800000 | 0-2.0 | Coke | N.E. | N.E. | N.E. | No |
| 7439-89-6 | FF250100 | 0.2-2.0 | Iron | N.E. | N.E. | N.E. | No |
| 7440-36-0 | N.E. | 0-2500 PPM | Antimony | 0.5 | 0.5 | N.E. | No |
| 7440-50-8 | CC4025000 | 5-1000 PPM | Copper | 1(dust & mist) | 1(dust & mist) | N.E. | No |
| 7440-02-0 | GL5325000 | 45-7000 PPM | Nickel | 0.1(soluble cpds) | 0.1(soluble cpds) | N.E. | IARC (2B), NTP |
| 7440-62-2 | QR5950000 | 45-7000 PPM | Vanadium | 0.05 (dust) | 0.05 (dust) | N.E. | No |
| 7439-92-1 | YW1355000 | 200 PPM | Lead | 50 µg/m³ | 0.15 | N.E. | IARC, NTP, OSHA |

*Components marked with an "*" are reportable under SARA Title III Section 313 (40CFR part 372). California Proposition 65 status: This product contains ingredients known to the State of California to cause cancer, birth defects or other reproductive harm. EPA has defined zeolites as statutory mixtures consisting of silica and alumina in various proportions plus metallic oxides and certain cations.

### SECTION III - PHYSICAL DATA

| SPECIFIC GRAVITY | pH | BULK DENSITY | BOILING POINT |
|---|---|---|---|
| @ 2.1 | 3-6 (5% slurry) | 0.7-1.1 g/cm³ | N.E. |
| APPEARANCE AND ODOR | | SOLUBILITY IN WATER | MELTING POINT |
| Off white to gray fine odorless powder. | | Nil - Heavy metals may leach off in water. | 2072 °C ($Al_2O_3$) |

### SECTION IV - FIRE AND EXPLOSION DATA

| FLASH POINT | METHOD USED | FLAMMABLE LIMITS | LEL | UEL |
|---|---|---|---|---|
| NOT APPLICABLE | NOT APPLICABLE | NOT APPLICABLE | NOT APPLICABLE | NOT APPLICABLE |

BASIC FIRE FIGHTING PROCEDURES

Use extinguishing agent suitable for surrounding fire. Exposed firefighters must wear MSHA/NIOSH approved positive pressure self-contained breathing apparatus with full face mask and protective clothing. Use water spray to cool fire-exposed containers.

UNUSUAL FIRE AND EXPLOSION HAZARDS

Combustible at high temperatures. Fire may produce poisonous or irritating gas, fumes or vapors. Irritating or toxic substances may be emitted upon thermal decomposition.

### SECTION V - REACTIVITY DATA

| STABLE | UNSTABLE | CONDITIONS TO AVOID |
|---|---|---|
| X | | Avoid contamination and wetting of catalyst. Avoid elevated temperatures. Avoid contact with strong oxidizers. |

INCOMPATIBILITY

Incompatible with strong mineral acids, Chlorine Trifluoride, and other halogenated compounds. Thermal decomposition products may include carbon monoxide, carbon dioxide, oxides of sulfur, nickel subsulfide and nickel carbonyl.

### SECTION VI - SPILL OR LEAK PROCEDURES

SPILL OR LEAK PROCEDURES

Where possible use vacuum suction for cleanup. Use dust suppressant when sweeping is necessary. Avoid methods that result in water pollution. Caution should be exercised regarding personnel safety and exposure to the spilled material, as indicated elsewhere in this data sheet. During an accidental release, personal protective equipment may be required (see Section VIII below). CERCLA reportable quantity should be calculated based on product analysis.

DISPOSAL OF SPILLED MATERIALS

Collect for disposal. Treatment, storage, transportation and disposal must be in accordance with local, state/provincial and federal regulation. Dispose of in an approved and permitted landfill. Catalyst is considered a hazardous waste in some states.

Page1of 2

## SECTION VII - HEALTH HAZARD DATA

**HEALTH HAZARDS - ACUTE (PRIMARY ROUTES OF ENTRY: INHALATION, INGESTION, SKIN CONTACT AND EYE CONTACT)**

SKIN: Dusts may be slightly to moderately irritating. Contact may cause reddening, itching and inflammation. Prolonged or repeated contact may cause dermatitis and allergic sensitization.

EYE: Direct contact may cause irritation, redness and pain. May also cause abrasion of the ocular surface. May cause discoloration of the eyelid and conjunctivae. Repeated or prolonged contact may cause conjunctivitis.

INGESTION: May cause liver damage & gastrointestinal disturbances. Symptoms include irritation, nausea, vomiting and diarrhea.

INHALATION: May cause respiratory tract irritation, pneumonitis and pulmonary edema. May cause an excess risk of asthmatic attacks in susceptible individuals. Fumes from heated material may cause metal fume fever, characterized by sweet or metallic taste in the mouth accompanied by dryness and irritation of the throat, cough, shortness of breath, general malaise, weakness, fatigue, muscle and joint pains, blurred vision, nose bleeds, bloody diarrhea, fever and chills. Repeated or prolonged breathing of particles of respirable size may cause inflammation of the lung leading to chest pain, difficulty breathing, coughing and possible fibrotic change in the lung - "pneumoconiosis". May cause "Siderosis" - inflammation of the lungs, chest pain, difficult breathing and coughing.
Nickel metal is a pulmonary sensitizer.

**HEALTH HAZARDS - CHRONIC**

Elevated concentrations of aluminum have been found in brain issue of patients with Alzheimer's Disease. It is still unclear whether aluminum is the cause or merely a marker of some other disease process.

Quartz has been classified by IARC as a class 2A carcinogen. NTP, IARC and OSHA have determined that lead is a confirmed human carcinogen.

IARC has determined that there is sufficient evidence for the carcinogenicity of nickel and nickel compounds in humans. NTP has classified nickel and nickel compounds as substances that may reasonably be anticipated to be carcinogens. Animal testing indicates that nickel and nickel compounds may cause reproductive effects.

This product may contain Titanium Dioxide. IARC has determined that there is inadequate evidence for the carcinogenicity of Titanium Dioxide in humans. IARC has determined that there is limited evidence for the carcinogenicity of Titanium Dioxide in experimental animals. (IARC Class 3)

There is suggestive evidence that Yttrium compounds exert some carcinogenic activity based on oral test with laboratory animals. In animal studies Yttrium compounds have produced decreased body weights, pneumoconiosis, emphysema and enlarged lymph nodes

**EMERGENCY AND FIRST AID PROCEDURES**

SKIN: Remove contaminated clothing immediately. Wash area of contact thoroughly with soap and water. Get medical attention if irritation persists.

EYE: Flush immediately with large amounts of temperate potable water for at least fifteen minutes. Eyelids should be held away from the eyeball to ensure thorough rinsing. Get immediate medical attention.

INHALATION: Remove affected person from source of exposure. If not breathing, ensure airway is not obstructed and administer mouth-to-mouth resuscitation and/or CPR as appropriate. If breathing is difficult, administer oxygen if available. After administration of oxygen, continue to monitor closely. Keep affected person warm and at rest. Get medical attention immediately.

INGESTION: If victim is conscious, give one to three glasses of water or milk to dilute stomach contents. Keep affected person warm and at rest. Get immediate medical attention.

**NOTES TO PHYSICIAN**

Persons with asthmatic-type conditions, chronic bronchitis, other respiratory diseases or recurrent skin eczema or sensitization should be excluded from working with this material. It is conceivable that trace metals could induce symptoms of dermal sensitivity.

**MEDICAL CONDITIONS AGGRAVATED BY EXPOSURE**

Persons with preexisting cardiovascular, skin or respiratory conditions, including asthma, may be at an increased risk from exposure.

## SECTION VIII - SPECIAL PROTECTION INFORMATION

**RESPIRATORY PROTECTION**

If exposure limits are to be exceeded or if irritation is experienced, NIOSH approved respiratory protection should be worn. NIOSH approved respirator for particulates with a TLV of less than 0.05 $mg/m_3$ is generally acceptable. In areas where oxygen content is less than 19.5% or where airborne concentrations of dust are high, NIOSH approved supplied air respirator should be worn. Ventilation and other forms of engineering controls are often the preferred means for controlling chemical exposures. Respiratory protection may be needed for non-routine emergency situations.

**EYE/SKIN PROTECTION**

Avoid eye contact with this material. Wear safety glasses or dust proof chemical goggles if airborne concentrations are high. Provide an eyewash station immediately accessible to the work area. Do not wear contact lenses when working with this material. Prevent skin contact. Wear gloves found to be impervious under conditions of use. Additional protection may be necessary to prevent skin contact including apron, arm covers, face shield, boots or full body protection. A safety deluge shower should be located in the work area.

## SECTION IX - SPECIAL PRECAUTIONS

**PRECAUTIONS TO BE TAKEN IN HANDLING AND STORAGE**

Flammable, toxic and/or corrosive gases may be found in confined vapor spaces. Do not enter confined vapor spaces without proper protective equipment. Water contamination should be avoided. Hands and face should be washed with soap and water prior to eating, drinking, smoking and application of cosmetics, and these activities should be prohibited in areas where this product is used. Contaminated work clothes should not be brought home. Empty containers may contain toxic, flammable or explosive vapors. Do not cut, grind, drill, weld, reuse or dispose of containers unless adequate precautions are taken against these hazards. Store in a well ventilated area away from sources of ignition and incompatibles. Area should be secured to prevent unauthorized access to catalyst.

## Blower sketch and performance

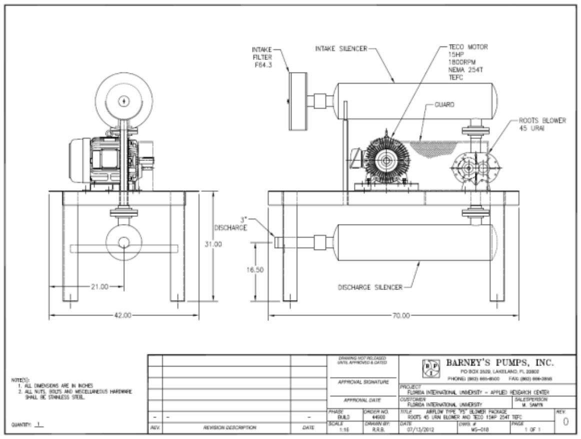


| Speed RPM | 1 PSI | | 6 PSI | | 7 PSI | | 10 PSI | |
|---|---|---|---|---|---|---|---|---|
| | CFM | BHP | CFM | BHP | CFM | BHP | CFM | BHP |
| 860 | 79 | 0.5 | 42 | 2.7 | 37 | 3.2 | - | - |
| 1760 | 188 | 1 | 151 | 5.7 | 146 | 6.6 | 133 | 9.4 |
| 3600 | 410 | 2.7 | 374 | 12.2 | 369 | 14.1 | 356 | 19.8 |

**Figure Ap. 1. Technical drawing of the Roots blower purchased at FIU (on left) and the performance of the blower (on right)**

## Verification test for the Field point 2010 data acquisition devices

**Table Ap. 2 Verification for the Fieldpoin® data acquisition units**

| FP-AI 110 ** | | | | FP-AI 110 ** | | | | FP-AI 110 ** | | | |
|---|---|---|---|---|---|---|---|---|---|---|---|
| Channel | Source current (mA) | FP reading current (mA) | error % | Channel | Source current (mA) | FP reading current (mA) | error % | Channel | Source current (mA) | FP reading current (mA) | error % |
| 0 | 0 | 0 | 0 | 3 | 0.001 | 0 | 0 | 6 | 0.001 | 0 | 0 |
| 0 | 5.002 | 5.003 | 0.019992 | 3 | 5.006 | 5.152 | 2.9165002 | 6 | 4.999 | 7.086 | 41.7483497 |
| 0 | 10.004 | 10.004 | 0 | 3 | 10.002 | 10.312 | 3.09938012 | 6 | 10.002 | 14.133 | 41.3017397 |
| 0 | 15 | 15.001 | 0.006667 | 3 | 15.002 | 15.466 | 3.09292094 | 6 | 14.998 | 21 | 40.0186692 |
| 0 | 19.999 | 19.998 | 0.005 | 3 | 20.007 | 20.618 | 3.05393112 | 6 | 20.001 | 21 | 4.99475026 |
| 1 | 0.001 | 0 | 0 | 4 | 0.001 | 0 | 0 | 7 | 0.002 | 0 | 0 |
| 1 | 4.998 | 4.993 | 0.10004 | 4 | 5.001 | 5.001 | 0 | 7 | 5.007 | 5.006 | 0.01997204 |
| 1 | 10.003 | 10.003 | 0 | 4 | 10.001 | 9.998 | 0.029997 | 7 | 9.993 | 9.995 | 0.02001401 |
| 1 | 15.001 | 15 | 0.006666 | 4 | 15.005 | 15.005 | 0 | 7 | 14.996 | 14.995 | 0.00666844 |
| 1 | 19.999 | 20 | 0.005 | 4 | 20.008 | 20.005 | 0.014994 | 7 | 20.005 | 20.003 | 0.0099975 |
| 2 | 0.001 | 0 | 0 | 5 | 0.001 | 0 | 0 | | | | |
| 2 | 5.002 | 5.172 | 3.398641 | 5 | 4.992 | 5.002 | 0.20032051 | | | | |
| 2 | 10.009 | 10.342 | 3.327006 | 5 | 10.002 | 10.004 | 0.019996 | | | | |
| 2 | 14.995 | 15.501 | 3.374458 | 5 | 15.007 | 14.999 | 0.05330846 | | | | |
| 2 | 20.009 | 20.687 | 3.388475 | 5 | 20.008 | 19.995 | 0.06497401 | | | | |

| FP-AI 100 -2 | | | | FP-AI 100 -2 | | | | FP-AI 100 -2 | | | |
|---|---|---|---|---|---|---|---|---|---|---|---|
| Channel | Source current (mA) | FP reading current (mA) | error % | Channel | Source current (mA) | FP reading current (mA) | error % | Channel | Source current (mA) | FP reading current (mA) | error % |
| 0 | 0 | 0 | 0 | 3 | 0.001 | 0 | 0 | 6 | 0.001 | 0 | 0 |
| 0 | 4.997 | 4.993 | 0.059988002 | 3 | 5.001 | 4.998 | 0.059988 | 6 | 4.999 | 4.999 | 0 |
| 0 | 9.982 | 9.987 | -0.05009016 | 3 | 10.002 | 10.003 | -0.009998 | 6 | 9.993 | 9.995 | -0.02001 |
| 0 | 14.998 | 15.004 | -0.04000533 | 3 | 15.002 | 15.004 | -0.01333156 | 6 | 15.003 | 15.004 | -0.00667 |
| 0 | 20.005 | 20.009 | -0.019995 | 3 | 20.004 | 20.003 | 0.004999 | 6 | 20.005 | 20.009 | -0.02 |
| 1 | 0.001 | 0 | 0 | 4 | 0.001 | 0 | 0 | 7 | 0.002 | 0 | 0 |
| 1 | 5.005 | 5.002 | 0.05994006 | 4 | 5 | 5.007 | -0.14 | 7 | 5.001 | 5.006 | -0.09998 |
| 1 | 9.998 | 9.995 | 0.030006001 | 4 | 9.995 | 10.004 | -0.09004502 | 7 | 10.004 | 10.009 | -0.04998 |
| 1 | 15.003 | 15.004 | -0.00666533 | 4 | 15.003 | 15.013 | -0.059984 | 7 | 14.999 | 15.004 | -0.03334 |
| 1 | 20.008 | 20.009 | -0.004998 | 4 | 20.005 | 20.0013 | 0.01849538 | 7 | 20.002 | 20.003 | -0.005 |
| 2 | 0.001 | 0 | 0 | 5 | 0.001 | 0 | 0 | | | | |
| 2 | 5.001 | 5.005 | -0.079984 | 5 | 4.999 | 21.152 | -323.124625 | | | | |
| 2 | 9.998 | 9.993 | 0.050010002 | 5 | 10.005 | 22.746 | -127.346327 | | | | |
| 2 | 15.004 | 15.003 | 0.006664889 | 5 | 15.003 | 24 | -59.9680064 | | | | |
| 2 | 20.004 | 20.006 | -0.009998 | 5 | 20.005 | 24 | -19.9700075 | | | | |

| FP-AI 100 -2 | | | | FP-AI 100 -2 | | | | FP-AI 100 -2 | | | |
|---|---|---|---|---|---|---|---|---|---|---|---|
| Channel | Source current (mA) | FP reading current (mA) | error % | Channel | Source current (mA) | FP reading current (mA) | error % | Channel | Source current (mA) | FP reading current (mA) | error % |
| 0 | 0 | 0 | 0 | 3 | 0.001 | 0 | 0 | 6 | 0.001 | 0 | 0 |
| 0 | 4.997 | 4.993 | 0.059988002 | 3 | 5.001 | 4.998 | 0.059988 | 6 | 4.999 | 4.999 | 0 |
| 0 | 9.982 | 9.987 | -0.05009016 | 3 | 10.002 | 10.003 | -0.009998 | 6 | 9.993 | 9.995 | -0.02001 |
| 0 | 14.998 | 15.004 | -0.04000533 | 3 | 15.002 | 15.004 | -0.01333156 | 6 | 15.003 | 15.004 | -0.00667 |
| 0 | 20.005 | 20.009 | -0.019995 | 3 | 20.004 | 20.003 | 0.004999 | 6 | 20.005 | 20.009 | -0.02 |
| 1 | 0.001 | 0 | 0 | 4 | 0.001 | 0 | 0 | 7 | 0.002 | 0 | 0 |
| 1 | 5.005 | 5.002 | 0.05994006 | 4 | 5 | 5.007 | -0.14 | 7 | 5.001 | 5.006 | -0.09998 |
| 1 | 9.998 | 9.995 | 0.030006001 | 4 | 9.995 | 10.004 | -0.09004502 | 7 | 10.004 | 10.009 | -0.04998 |
| 1 | 15.003 | 15.004 | -0.00666533 | 4 | 15.004 | 15.013 | -0.059984 | 7 | 14.999 | 15.004 | -0.03334 |
| 1 | 20.008 | 20.009 | -0.004998 | 4 | 20.005 | 20.0013 | 0.01849538 | 7 | 20.002 | 20.003 | -0.005 |
| 2 | 0.001 | 0 | 0 | 5 | 0.001 | 0 | 0 | | | | |
| 2 | 5.001 | 5.005 | -0.079984 | 5 | 4.999 | 21.152 | -323.124625 | | | | |
| 2 | 9.998 | 9.993 | 0.050010002 | 5 | 10.005 | 22.746 | -127.346327 | | | | |
| 2 | 15.004 | 15.003 | 0.006664889 | 5 | 15.003 | 24 | -59.9680064 | | | | |
| 2 | 20.004 | 20.006 | -0.009998 | 5 | 20.005 | 24 | -19.9700075 | | | | |

## Verification test for the measurement devices used in the pitot tube test (density calculation)

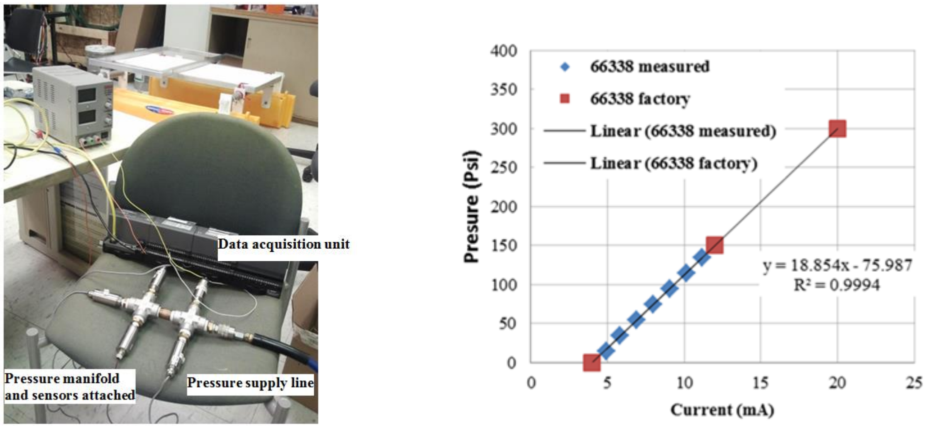


**Figure Ap. 2. Pressure sensor verification test for sensor # 66338 used in pitot tube test.**

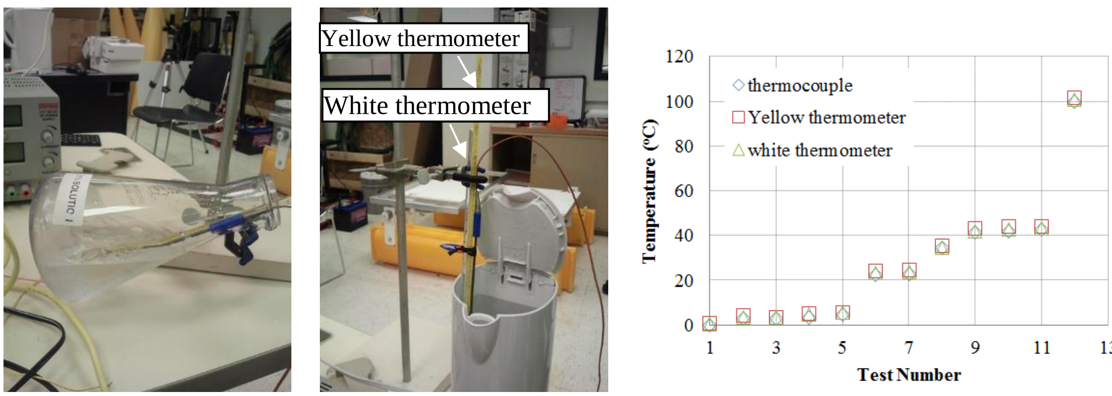


**Figure Ap.3.** Thermocouple T-type verification test, used in pitot tube test.

## Verification test for the measurement devices used in rise pressure profile measurement

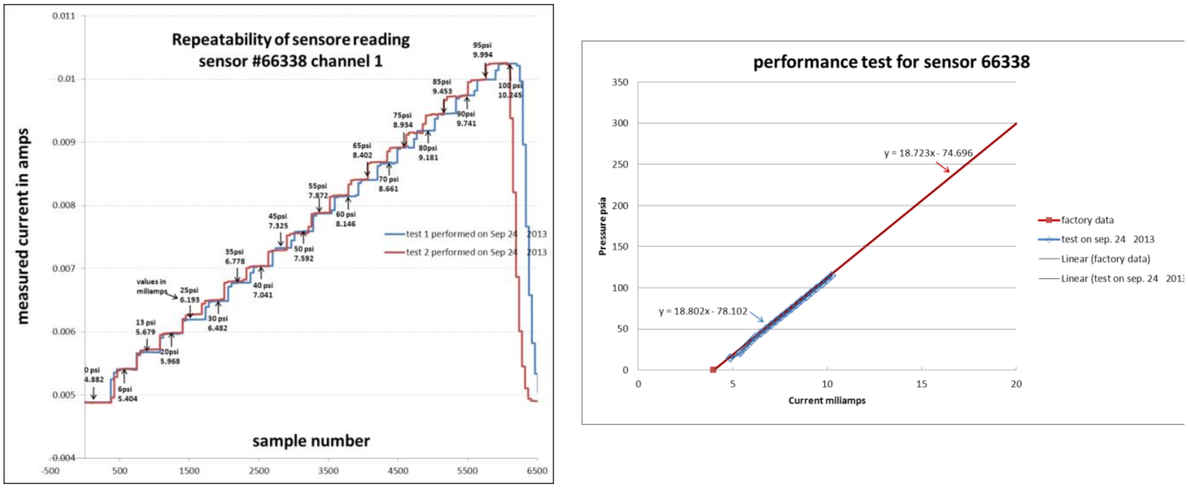


**Figure Ap. 4. Verification test for sensor # 66338, (a) response to excitation pressure, (b) curve fitting to the data**

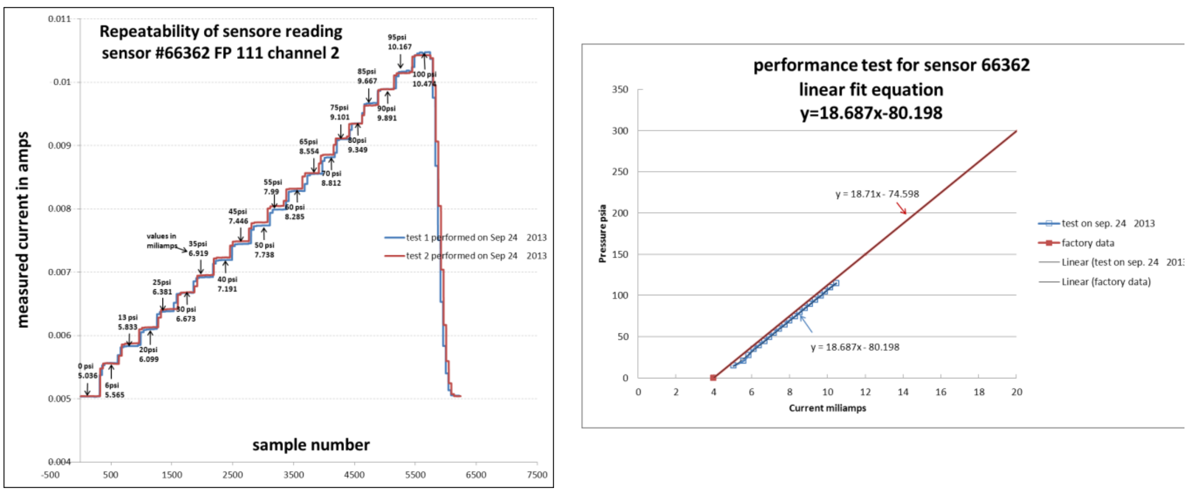


**Figure Ap. 49 Verification test for sensor # 66362, (a) response to excitation pressure, (b) curve fitting to the data**

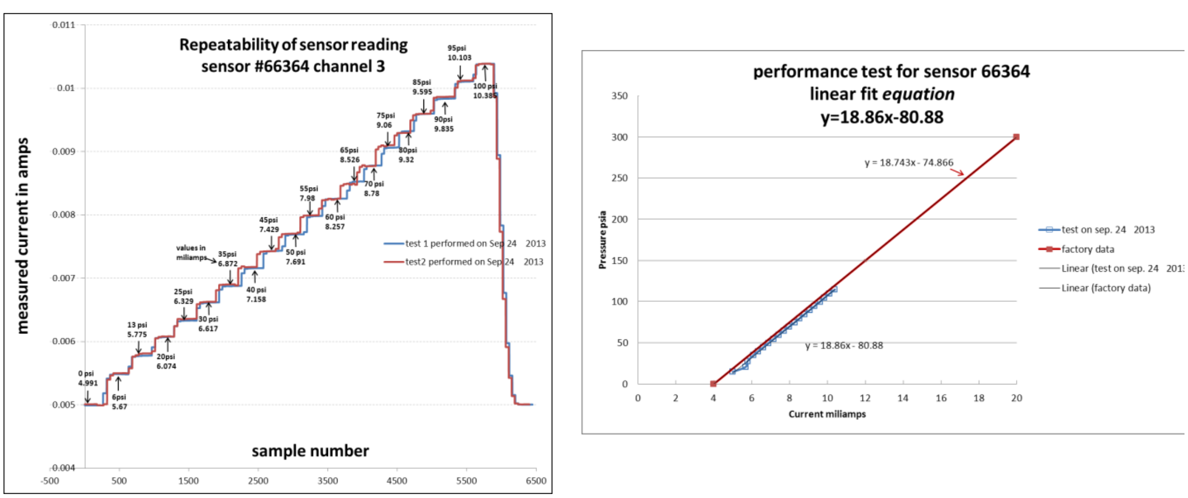


**Figure Ap. 6. Verification test for sensor # 66364, (a) response to excitation pressure, (b) curve fitting to the data**

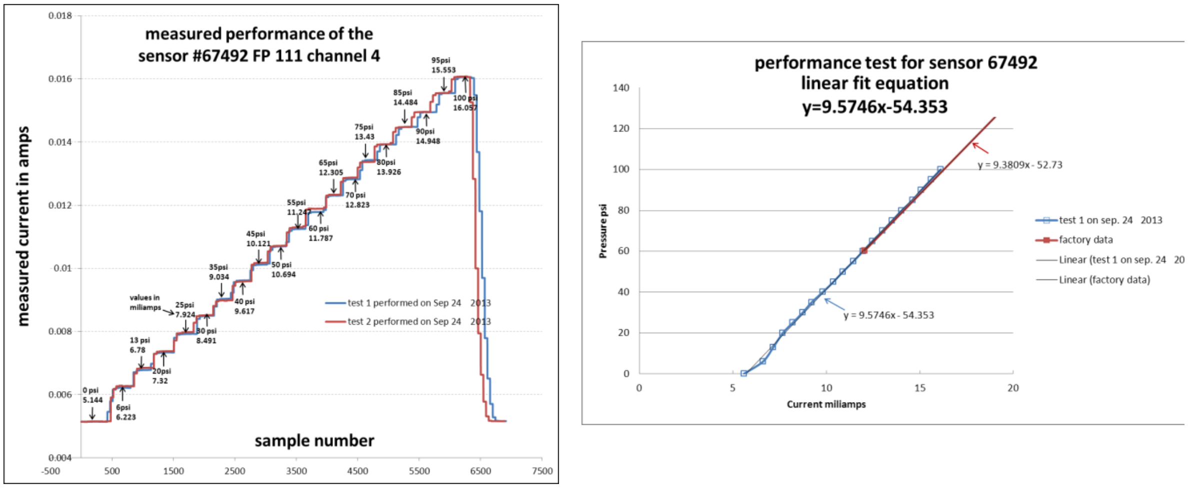


**Figure Ap. 7. Verification test for sensor # 67492, (a) response to excitation pressure, (b) curve fitting to the data**

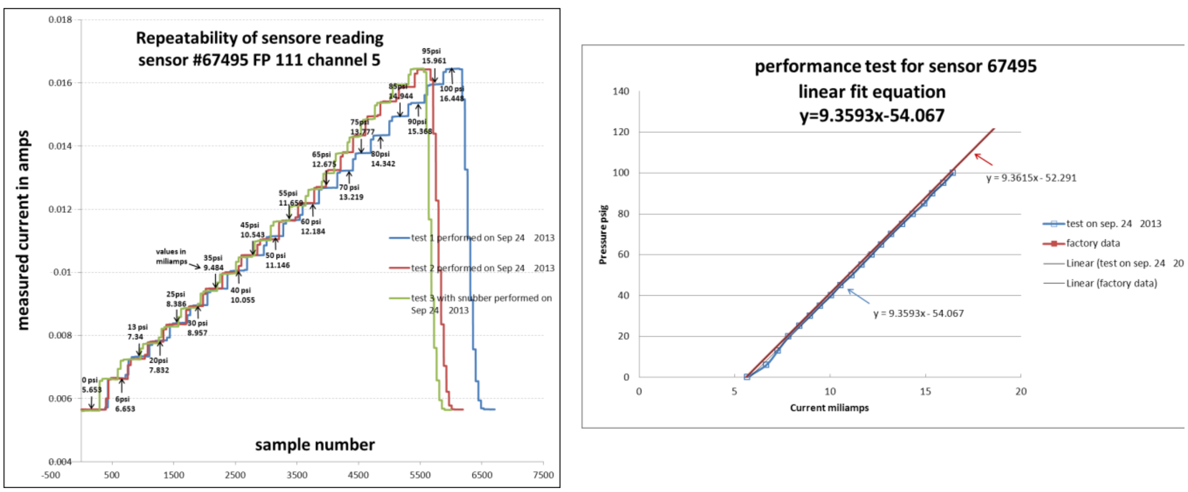


**Figure Ap. 8. Verification test for sensor # 67495, (a) response to excitation pressure, (b) curve fitting to the data**

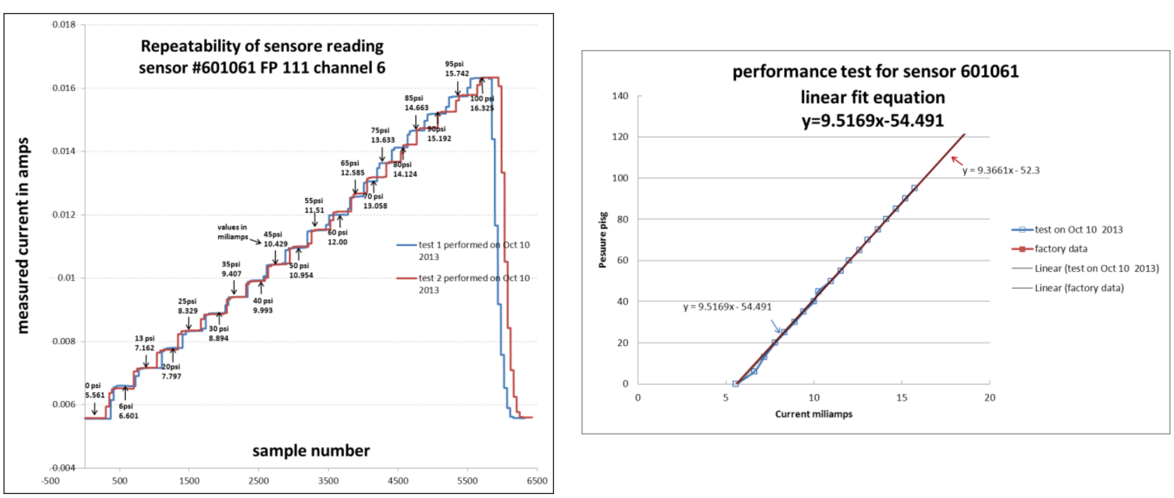


**Figure Ap. 9. Verification test for sensor # 601061, (a) response to excitation pressure, (b) curve fitting to the data**

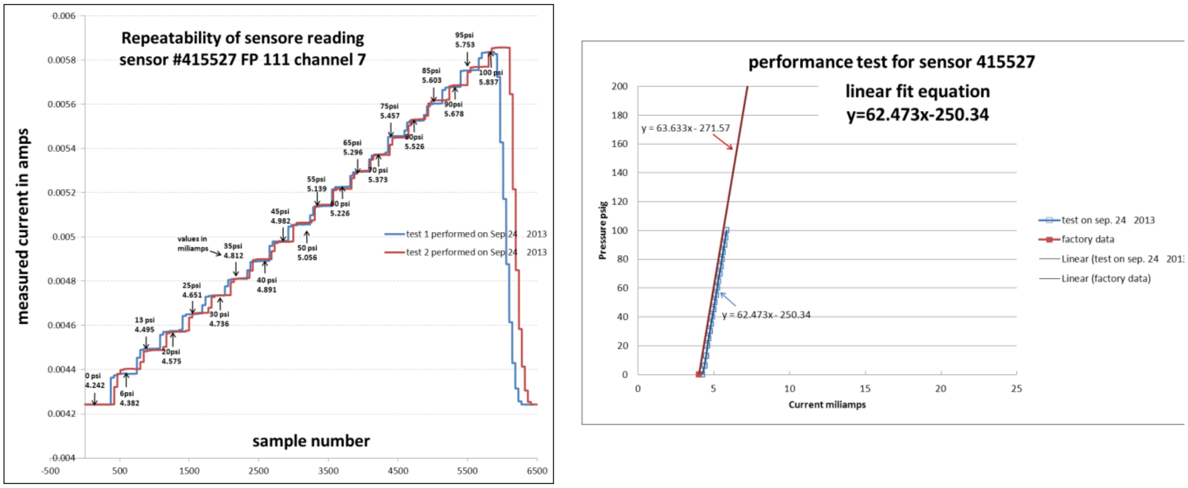


**Figure Ap. 10. Verification test for sensor # 415527, (a) response to excitation pressure, (b) curve fitting to the data**

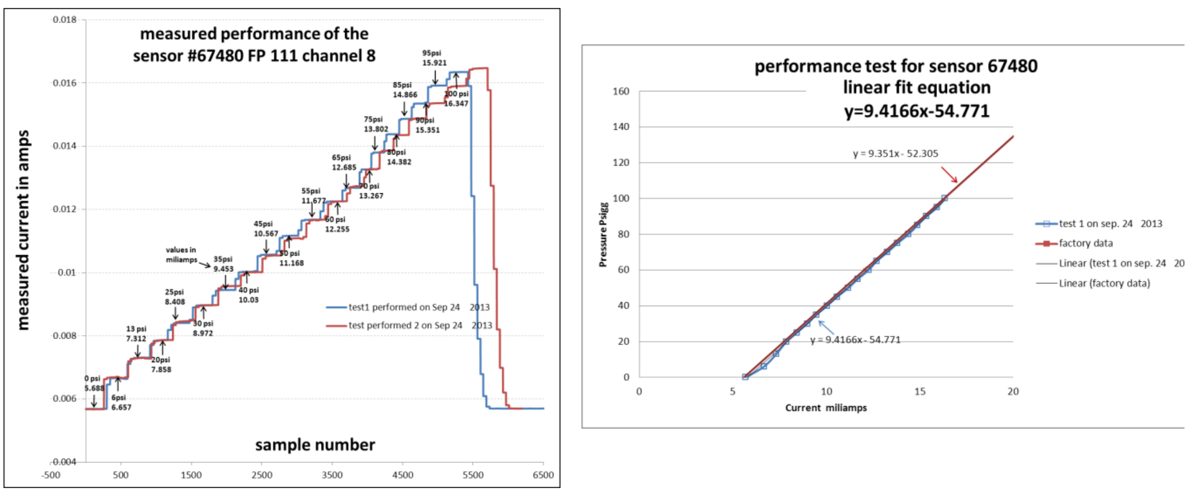


**Figure Ap. 11. Verification test for sensor # 67480 (a) response to excitation pressure, (b) curve fitting to the data**

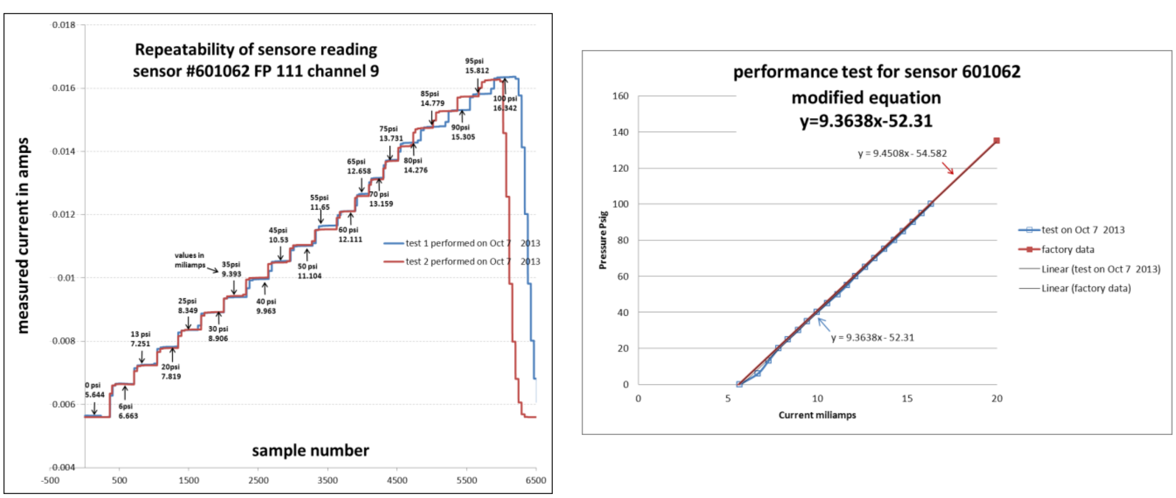


**Figure Ap. 12. Verification test for sensor # 601062, (a) response to excitation pressure, (b) curve fitting to the data**

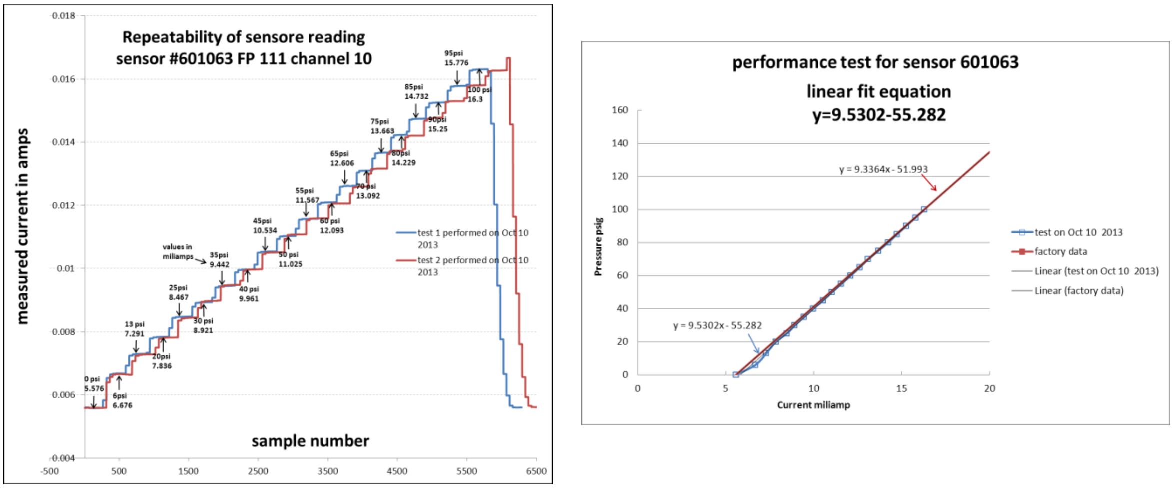


**Figure Ap. 13. Verification test for sensor # 601063, (a) response to excitation pressure, (b) curve fitting to the data**

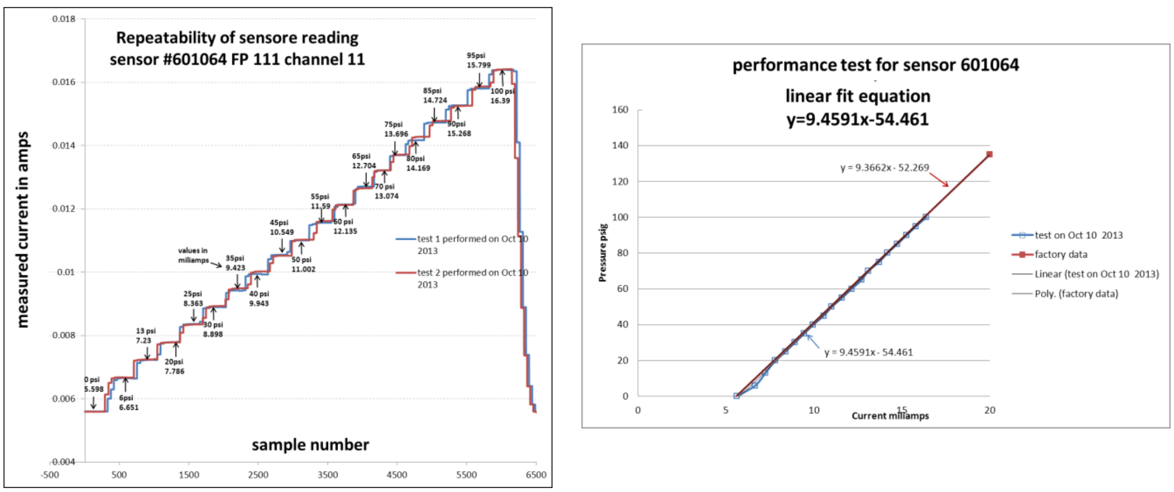


**Figure Ap. 14. Verification test for sensor # 601064, (a) response to excitation pressure, (b) curve fitting to the data**

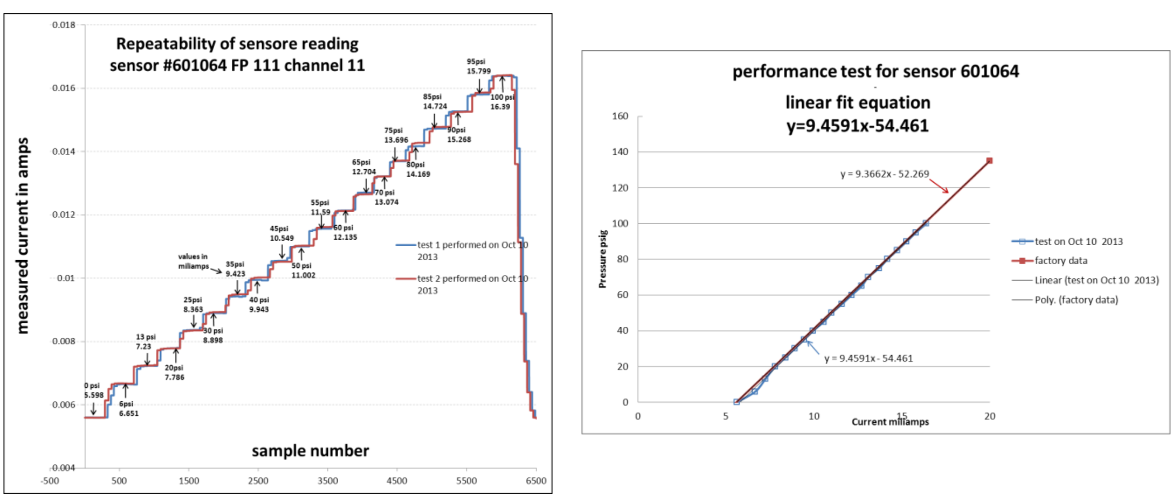


**Figure Ap. 15. Verification test for sensor # 601064, (a) response to excitation pressure, (b) curve fitting to the data**

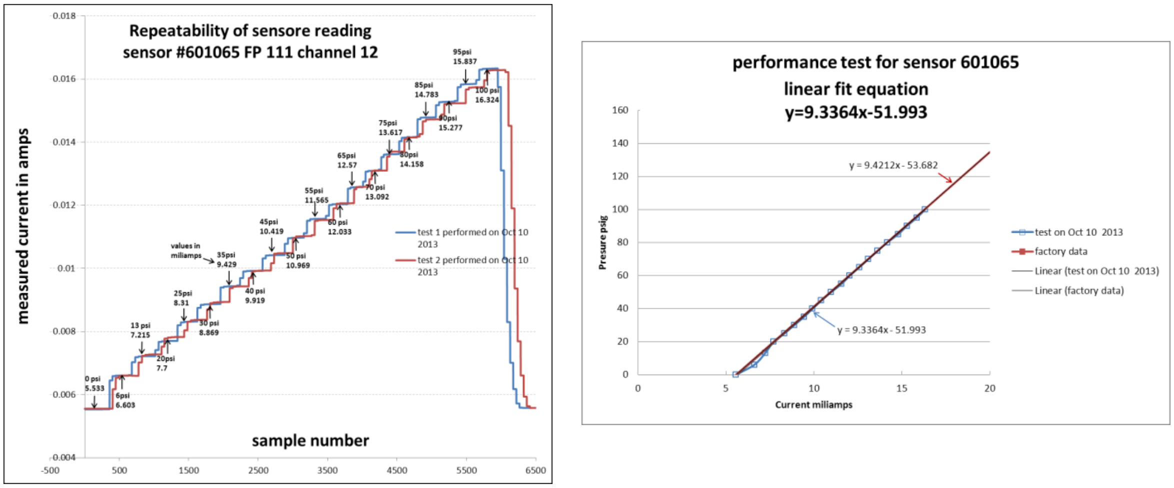


**Figure Ap. 16. Verification test for sensor # 601065, (a) response to excitation pressure, (b) curve fitting to the data**

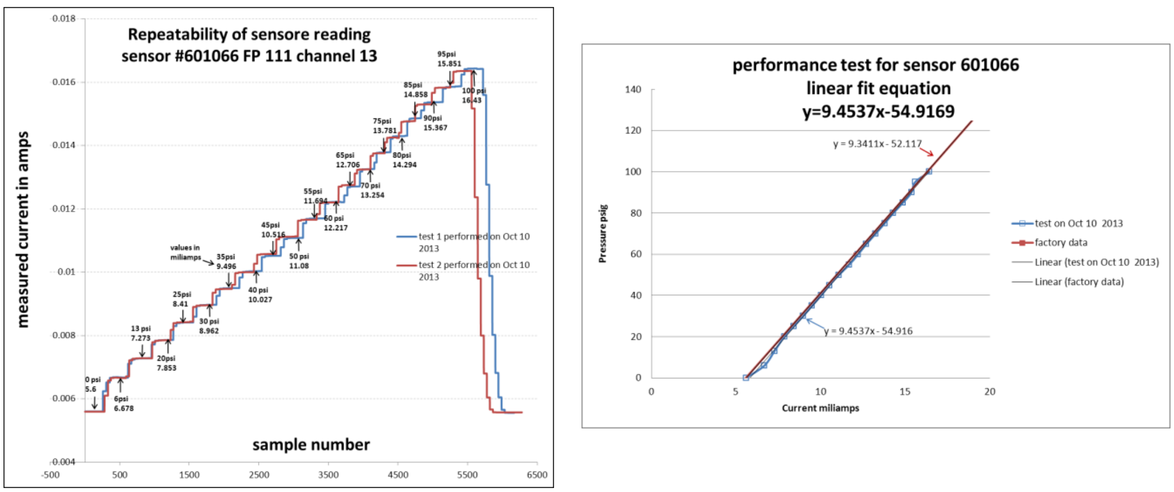


**Figure Ap. 17.50 Verification test for sensor # 601066, (a) response to excitation pressure, (b) curve fitting to the data**

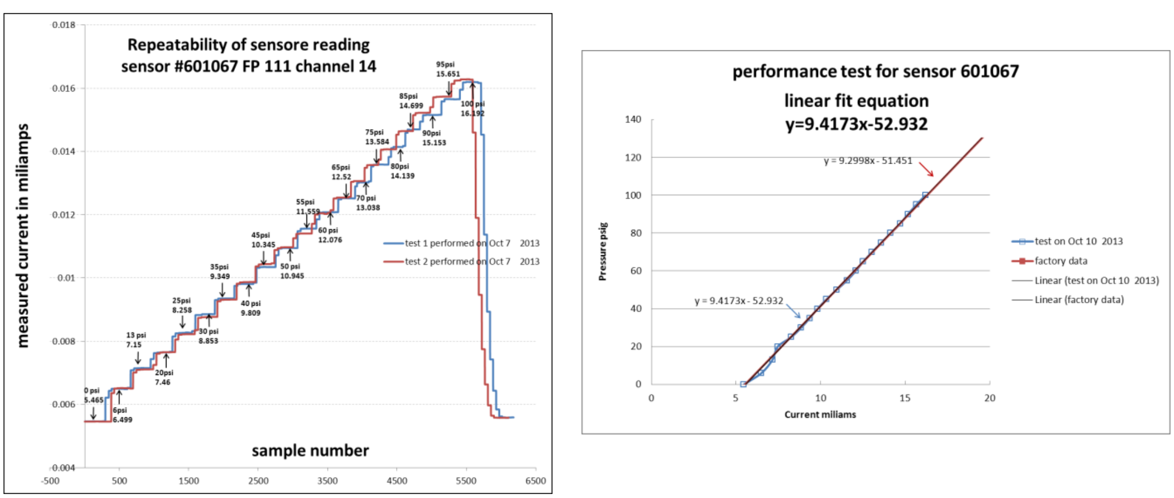


**Figure Ap. 18. Verification test for sensor # 601067, (a) response to excitation pressure, (b) curve fitting to the data**

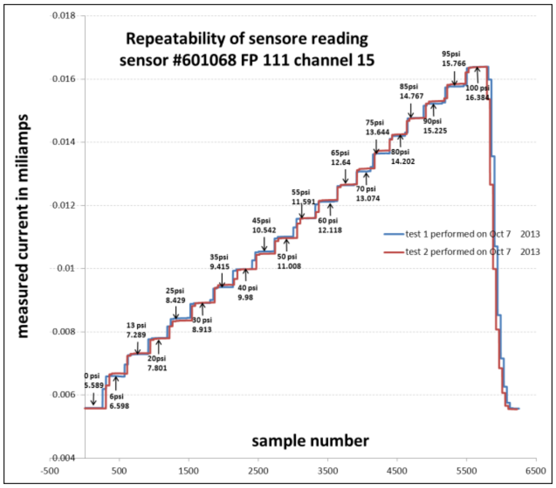


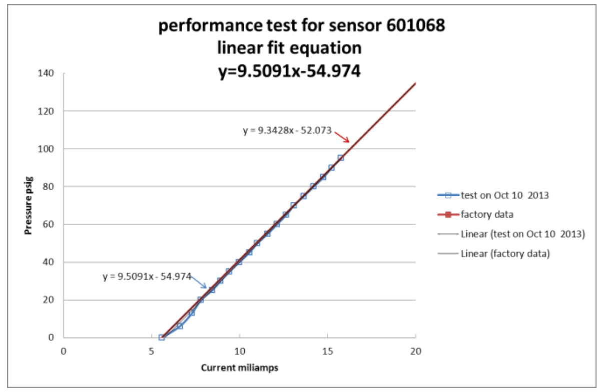


**Figure Ap. 19. Verification test for sensor # 601068, (a) response to excitation pressure, (b) curve fitting to the data**

## Design of new Labview VI for curve fittings (transducer verification tests)

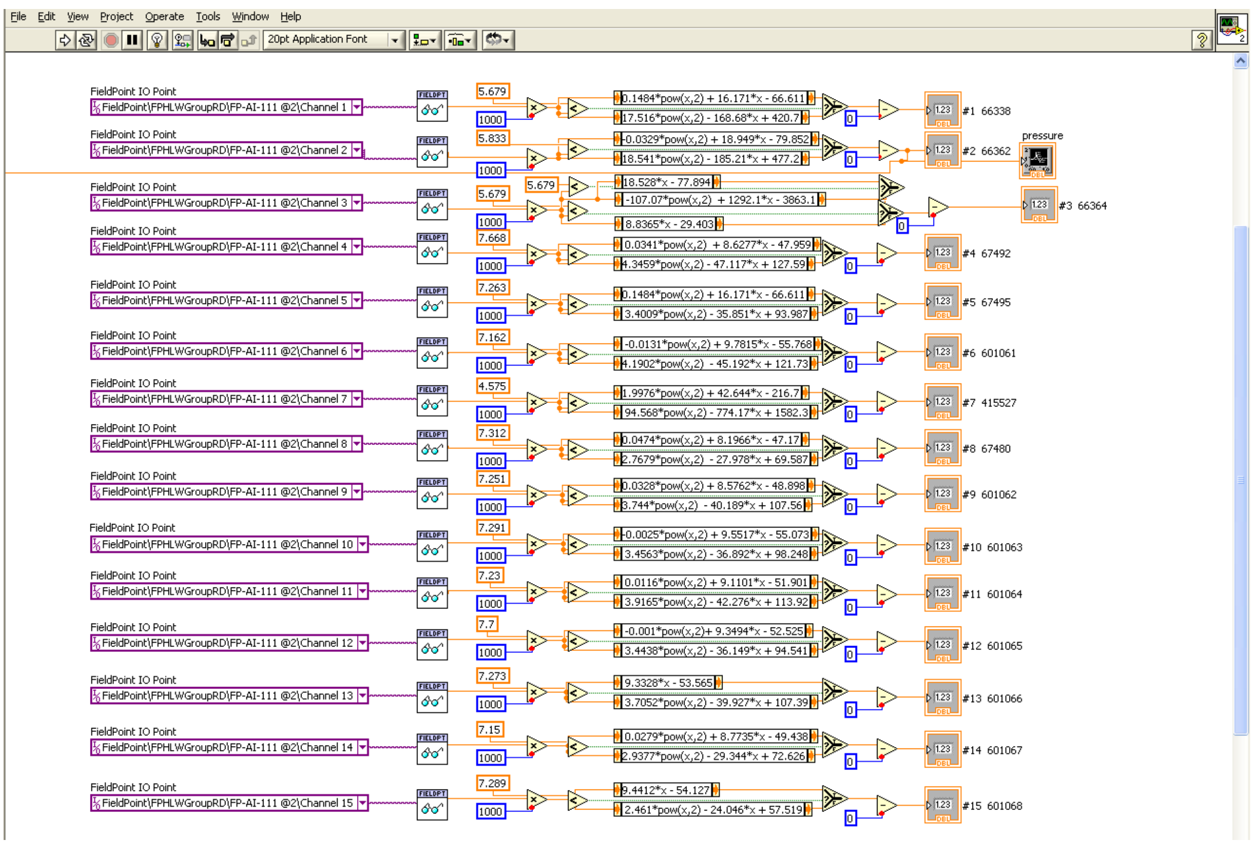

**Figure Ap. 20. Schematic of the designed VI for the CFB, equation of curve fitting for each pressure transducer and filed point modules**

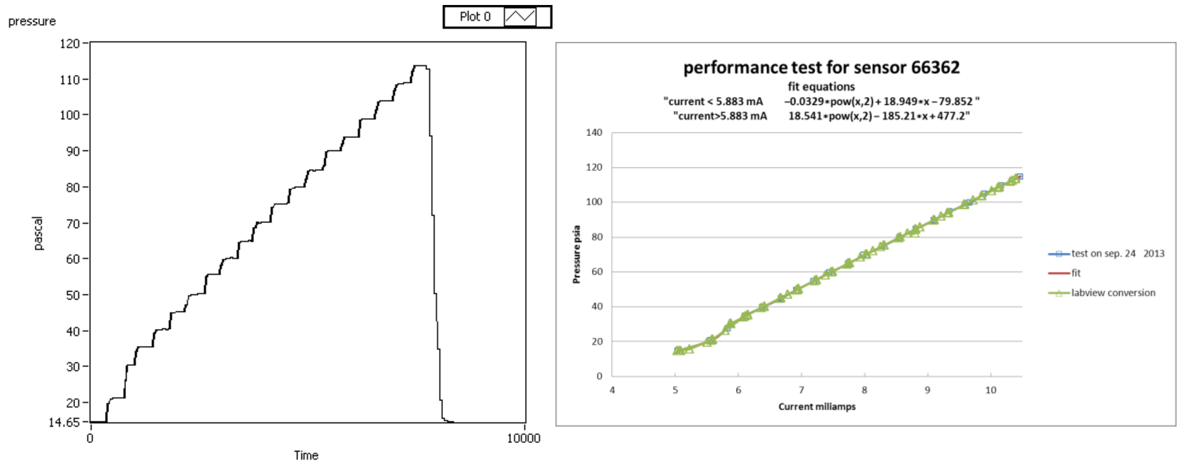


**Figure Ap. 21. Precise regeneration of pressure data through current-to-pressure conversion using the Labview VI for the sensor 66362 using the Field point AI-111**

# Construction of 3D particle configurations

The following four statistical quantities, i.e,

the solid volume fraction,

$$\phi = \frac{n\pi}{6} d_p^{\,3}, \qquad \textbf{Equation Ap. 1}$$

the radial distribution function,

$$g(r) = \frac{N(r,\delta r)}{N_p\left(N_p - 1\right)/2} \times \frac{V}{V_r(r,\delta r)}, \qquad \textbf{Equation Ap. 2}$$

The covariance of the indicator field,

$$C(r) = \left\langle I^{(\beta)}(\mathbf{x}) I^{(\beta)}(\mathbf{x}+\mathbf{r}) \right\rangle, \qquad \textbf{Equation Ap. 3}$$

$$I^{(\beta)}(\mathbf{x}) = \begin{cases} 1, & \mathbf{x} \text{ in phase } \beta \\ 0, & \text{otherwise} \end{cases} \qquad \textbf{Equation Ap. 4}$$

The radius of gyration tensor

$$\frac{R_{g,ij}^{2}}{R_g^{2}} = \frac{1}{N_c} \sum_{k=1}^{N_c} \left(x_{k,i} - r_i\right)\left(x_{k,j} - r_j\right) \qquad \textbf{Equation Ap. 5}$$

were used in the collaborator's computer modeling. In these relations, n is the number of particles in a unit volume of a fluid-particle suspension, $d_p$ is the particle diameter, $N(r, \delta r)$ is the total number of particle pairs separated by $r$ in a spherical shell with thickness $\delta r$, $V_r(r, \delta r)$ represents the volume of the spherical shell. Figure Ap. displays the spherical shell and the separation radius. The $N_c$ is the number of particles in the cluster, $\mathbf{r}$ is the cluster center of mass, $\mathbf{x}$ is the location of each particle in the cluster, and $R_g = \left(R_{g,ii}^2\right)^{1/2}$ is the radius of gyration, respectively.

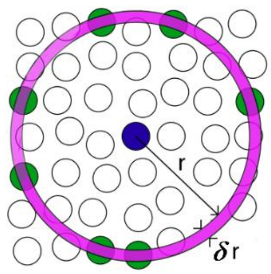


**Figure Ap. 22. Computational Space discretization for the evaluation of the radial distribution function**

The radial distribution function is defined as the probability of finding a particle at separation $r$ given that a test particle is at the coordinate origin. The covariance of indicator function is another second-order statistic that is used to characterize structures in multi-phase media, and provides information about local solid-phase volume fraction at separation *r*. The radius of gyration tensor is a mesoscale quantity that describes the isotropy/anisotropy of clusters.

To reproduce a particle configuration representing the same characteristics as shown experimental data, the following procedure was followed:

1. Statistical quantities measured from ensemble of 2D experimental images were chosen as benchmarks.
2. A 3D particle configuration was created.
3. For consistency between numerical and experimental data, 2D projected images from the 3D particle configuration were created, followed by computations of statistical quantities from these images.
4. The quantities from generated particle configuration were compared with the experimental counterparts. If the errors were relatively small, then the 3D particle configuration was a good representation for the experimental data. Otherwise, steps 2-4 were repeated until a desired configuration was obtained. This step involved an optimization problem which tried to minimize the difference between a created 3D ensemble and its real experimental configurations.
5. 

In this study, the *simulated annealing method* (Kirkpatrick, 1983) was selected to minimize the objective function. The simulated annealing method is a generic probabilistic method for locating a good approximation to the global optimum of a given function in a large variable space. The method is inspired from annealing in metallurgy, a technique involving heating and controlled cooling of a material to increase the size of its crystals and reduce their defects. The heat causes the atoms to become unstuck from their initial positions and randomly move through states of higher energy. The slow cooling gives them more chances of finding configurations with lower internal energy than the initial one.

## Numerical approach of the collaborators

In our problem, an initial particle configuration was generated and a relatively high temperature $T$ was assigned to it. At each time step of the cooling process, particle positions were modified slightly by the following expression

$$\mathbf{x}^{n+1} = \mathbf{x}^{n} + \beta(T)\ d_p\ \mathbf{e}, \qquad \textbf{Equation Ap. 6}$$

where $\mathbf{e}$ is a random unit vector, and $\beta(T)$ is a temperature-dependent coefficient always being less than 1 ($\beta(T) < 1$). This definition implies that particles are not allowed to move more than a particle diameter, preventing the particle configuration from a substantial change.

The probability of accepting the transition to the new particle configuration is specified by an *acceptance probability* $P(T, \Delta F)$ given by

$$P(T, \Delta F) = \begin{cases} 1, & \Delta F \le 0 \\ e^{-\Delta F / T}, & \Delta F > 0 \end{cases} \qquad \textbf{Equation Ap. 7}$$

where $\Delta F$ is the objective function increment from the previous state to the current one. According to the above expression, objective function decrease is always accepted, while increase of objective function is accepted with a probability given by the Boltzmann factor. This definition for the acceptance probability allows the algorithm to escape from local minima. Upon the acceptance of particle configuration, the temperature of the system decreases through a cooling schedule. Several cooling schedules have been proposed for simulated annealing (Wong et al, 1988; Aart and Korst, 1989; Otten et al, 1989). In our method, we assume that the temperature decreases as $T^{n+1} = \alpha T^{n}$ with $\alpha \approx 0.95$. The cooling process continues until the temperature decreases to a minimum value, or the objective function increments become relatively small.

## Grid independence study in DNS simulations for clustered particles

These results indicate the mean drag force is converged with $L / d_p = 10$ and $D_m = d_p / \Delta x = 20$. Where, L, $d_p$, and Δx are the length of the cubical ensemble, particle diameter, and the length of the computation cell, respectively.

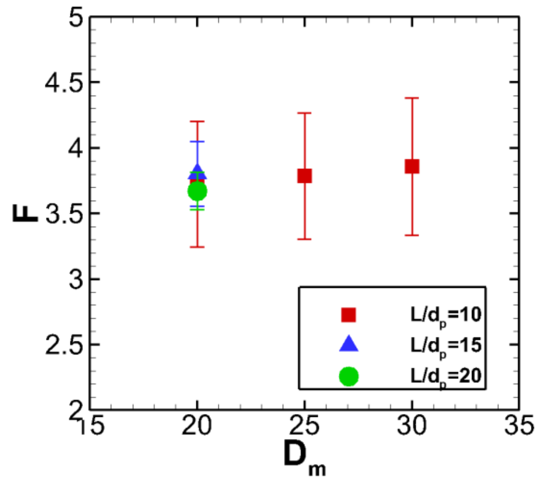


**Figure Ap. 23. Grid convergence study for particle configurations at $Re_m = 50$, L, and $d_p$ are the length of the cubical ensemble and particle diameter , respectively.**

# Derivation of equations governing the particle motion

**Relative equation of motion of particles:**

According to Ye et al. (2005b), the translational state of the particulate phase is described by the Newtonian equations of motion for each individual particle in the system.

For particle i :

$$m_i \frac{d^2\vec{x}_i}{dt^2} = \vec{F}_{c,i} + \vec{F}_{vdw,i} + \vec{F}_{drag,i} - V_i \nabla p + m_i \vec{g} \quad \textbf{Equation Ap. 8}$$

For particle j:

$$m_j \frac{d^2\vec{x}_j}{dt^2} = \vec{F}_{c,j} + \vec{F}_{vdw,j} + \vec{F}_{drag,j} - V_j \nabla p + m_j \vec{g} \quad \textbf{Equation Ap. 9}$$

$$\vec{F}_{c,i} = \vec{F}_{c,j} = 0 \quad \textbf{Equation Ap. 10}$$

and

$$\vec{F}_{drag,i} = \vec{F}_{drag,j} \quad \textbf{Equation Ap. 11}$$

$$V_i \nabla p = V_j \nabla p \quad \textbf{Equation Ap. 12}$$

$$m_i \vec{g} = m_i \vec{g} \quad \textbf{Equation Ap. 13}$$

$$\vec{F}_{vdw,i} = - \vec{F}_{vdw,j} \quad \textbf{Equation Ap. 14}$$

Figure Ap. shows the schematic of the particles with small separation distance from each other under the effect of the van der Waals force, the gas-particle drag force, the pressure gradient in the fluid, and the gravitational force. Subtraction of the Equation Ap. 9 from the Equation Ap. 8 results in cancellation of some of the terms and the following expression is obtained:

$$\frac{d^2(\vec{X}_i-\vec{X}_j)}{dt^2} = (\frac{1}{m_i}\vec{F}_{vdw,i} - \frac{1}{m_j}\vec{F}_{vdw,j})$$ **Equation Ap. 15**

where for the cohesive inter-particle force, we adopt the Hamaker expression (Chu, B. 1967) for two spheres, given by the following equation :

$$\left|\vec{F}_{vdw,ij}\ (d)\right| = \frac{A}{3}\ \frac{2R_iR_j(d+R_i+R_j)}{[d(d+2R_i+2R_j)]^2} \times \left[\frac{d(d+2R_i+2R_j)}{(d+2R_i+2R_j)^2 - (R_i-R_j)^2} - 1\right]^2$$ **Equation Ap. 16**

In this equation, A is the Hamaker constant, R is the radius of the particle and d is the surface-to-surface distance between the two particles, i and j. This expression simplifies to $\vec{F}_{vdw,ij}(d) = (AR/6d_{ij}^2)\ \vec{n}_{ij}$ for two sphere of the same diameter (as used by Ye et al. , 2005). Later, by placing the frame of reference on the particle j, and replacing the $d_{ij}$ with the distance d, in Figure Ap. , the Equation Ap. 17 can be reformatted as

$$(\frac{m_i m_j}{m_i + m_j})\frac{d\vec{V}_{rel.}^{(i)}}{dt} + \frac{AR}{6d^2} = 0.$$ **Equation Ap. 17**

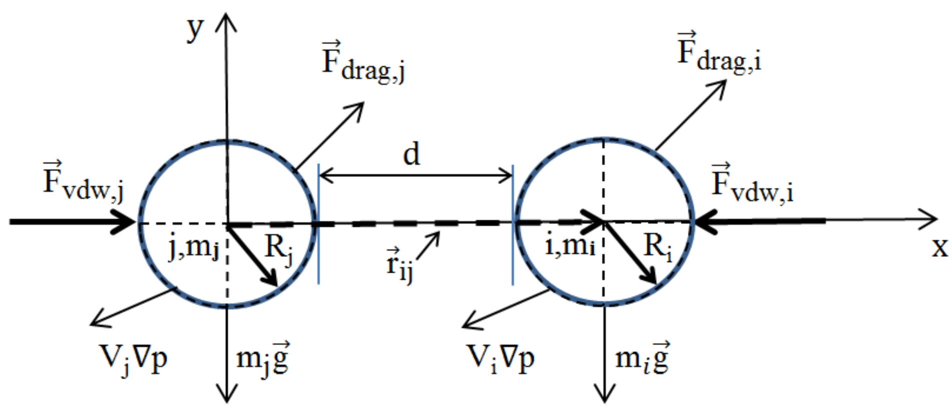


**Figure Ap. 24. Two spherical particles with equal radius (R), representation of the van der Waals force, the gas-particle drag force, the force due to pressure gradient in the fluid, and the gravitational force acting on particles.**

In these terms, m is the mass of the particle, V is the particle volume, $\vec{x}$ is the position vector pointing from the center of the particle j to the center of the particle i, and $\vec{g}$ is the vector of acceleration of gravity. $\vec{x}_{ij}$ is the vector of instantaneous relative position of the particle i with respect to the particle j.

Later, definition of the granular temperature, $\Theta$=1/3 ⟨particle velocity fluctuation$^2$⟩ (Lun et al., 1984 and Gidaspow, 1994), and a short range separation distance within which attractive forces are dominant (Ye et al. (2005a)), $d_0$, are used to create dimensionless parameters, such as $\tilde{t} = t\sqrt{\Theta_s}/ d_0$ and $\tilde{\vec{x}}_{ij}= \vec{x}_{ij} /d_0$, respectively. By defining the vector of relative velocity as $\vec{V}^{(ij)}= d\vec{x}^{(ij)}/dt$ , we obtain

$$Ha^{-1} \left[\frac{d_0}{d_p}\right]^2 \frac{d\tilde{\vec{V}}_{ij}}{d\tilde{t}}+1= 0 ,$$ **Equation Ap. 18**

where, $\tilde{\vec{V}}^{(i)}=\vec{V}^{(i)}/\sqrt{\Theta_s}$ and the Ha parameter is defined as

$$Ha = \frac{A}{\pi \rho d_p^2 d_0\Theta_s} .$$ **Equation Ap. 19**

## Equations governing the TFM

In the TFM, both the gas and the particulate phases are considered as interpenetrating continuous mediums. Complete derivations of the equations governing the two-fluid model can be found in the work of Gidaspow (1994). Here, the equations of the TFM model for flow without phase change and chemical reactions are given by Samuelsberg and Hjertager (1996) as

$$\frac{\partial(\rho_k\varepsilon_k)}{\partial t}+ \nabla. (\rho_k\varepsilon_k\vec{u}_k) = 0 ,$$ **Equation Ap. 20**

$$\frac{\partial(\rho_k\varepsilon_k\vec{u}_k)}{\partial t}+ \nabla. (\rho_k\varepsilon_k\vec{u}_k\vec{u}_k) = -\varepsilon_k\nabla p_k + \varepsilon_k\rho_k\vec{g} +\nabla. (\varepsilon_k\bar{\bar{\tau}}_k) + \beta(\vec{u}_l-\vec{u}_k) ,$$ **Equation Ap. 21**

$$\bar{\bar{\tau}}_k= \left[\lambda_k\nabla. \vec{u}_k\right]\bar{\bar{I}}+2 \mu_k \left[\frac{1}{2} \left[\nabla\vec{u}_k+\left(\nabla\vec{u}_k\right)^T\right]-\frac{1}{3}\nabla. \vec{u}_k\bar{\bar{I}}\right].$$ **Equation Ap. 22**

Equation Ap. **20** to Equation Ap. **22** show the equations for continuity, momentum balance, **and** the stress tensor for the phases in TFM, respectively. In these equations, $\rho$, $\vec{u}$ , $\varepsilon$, g, $\bar{\bar{\tau}}_k$ , $\beta$ , p, $\lambda$ and $\mu$ represent density, velocity vector, volume fraction, acceleration of gravity, shear stress tensor, momentum exchange coefficient, thermodynamic pressure, second coefficient of viscosity (or bulk viscosity), and the dynamic viscosity of the phases. In addition, k and l serve as identifiers for gas and solid phases. However, in Equation Ap. 21, identifiers are phase specific, where if k refers to one of the phases (e.g., fluid), then l can only refer to the solid, and vice versa. In this work, the second coefficient of viscosity for the gas phase is set to zero, as suggested by Lu et al. (2009).
The pressure term for the solid phase, $p_s$, is obtained by grouping the gas pressure and the solid phase pressure together, as displayed by Equation Ap. 23

$$p_s= p_g+P_s .$$ **Equation Ap. 23**

The solid phase pressure is obtained from the granular kinetic model of Ding and Gidaspow (1990, completed later by Gidaspow, 1991), as $P_S = \Theta_S[1+2(1+e_{SS})\,\boldsymbol{\varepsilon}_S\, g_{0SS}]$. Where, $\Theta_S$ and $e_{SS}$ represent the granular temperature of the solid phase and particle-particle restitution coefficient, respectively. Here, the $e_{ss}$ is set to 0.9 according to Jenkins and Zhang (2012) and Benyahia (2012). In addition, the solid bulk viscosity, solid shear viscosity, and radial distribution function are given by Samuelsberg and Hjertager (1996) as

$$\lambda_S = \rho_S\, d_p(e_{SS}+1)\, \frac{4\,\varepsilon_S^2\sqrt{\Theta_s}\, g_0}{3\sqrt{\pi}} \quad , \qquad \textbf{Equation Ap. 24}$$

$$= \frac{5\sqrt{(\pi\Theta_s)}\,\rho_S\, d_p}{48\,(e_{SS}+1)g_0}\left[(1+\frac{4}{5}\,(e_{SS}+1)\varepsilon_S g_0\right]^2 + \left(\frac{4\varepsilon_S^2\,\rho_S\, d_p\, g_0\,(1+e_{SS})\sqrt{\Theta_s}}{5\sqrt{\pi}}\right) \ , \qquad \textbf{Equation Ap. 25}$$

$$g_0 = \frac{3}{5}\left[1-\left[\frac{\varepsilon_S}{\varepsilon_{S_{max}}}\right]^{1/3}\right]^{-1} , \qquad \textbf{Equation Ap. 26}$$

respectively. The transport equation for the granular energy is originally derived by Ding and Gidaspow, (1990). However, a more complete version is given by Lu et al. (2009) as

## Algebraic and transport equations for the granular temperature

Transport equation of the granular temperature (Lu et al., 2009)

$$\frac{3}{2}\left[\frac{\partial}{\partial t}\left(\rho_s\varepsilon_S\Theta_S\right)+\nabla.\left(\rho_s\varepsilon_S\vec{v}_S\Theta_S\right)\right]=\left(-\varepsilon_S P_S\bar{\bar{I}}+\varepsilon_S\bar{\bar{\tau}}_S\right):\nabla\,\vec{u}_S-\nabla.\left(k_{\theta_S}\nabla\,\Theta_S\right)-\gamma_{\theta_S}-3\beta\Theta_S \ .$$

**Equation Ap. 27**

The diffusion coefficient of the granular temperature and the collisional energy dissipation are defined by Eq. (9) and Eq. (10), respectively (Samuelsberg and Hjertager, 1996).

$$k_{\boldsymbol{\theta}_S} = \frac{150\,\rho_S\, d_S\sqrt{(\Theta_s\pi)}}{384\,(1+e_{SS})g_0}\left[1+\frac{6}{5}\varepsilon_S g_0\,(1+e_{SS})\right]^2 + 2\rho_S\boldsymbol{\varepsilon}_S^2 d_S(1+e_{SS})g_0\sqrt{\frac{\Theta_s}{\pi}} \ , \qquad \textbf{Equation Ap. 28}$$

$$\gamma_{\theta_S} = 3(1-e_{SS}^2)\rho_S\varepsilon_S^2\Theta_S g_0\left(\frac{4\sqrt{\Theta_S}}{d_S\sqrt{\pi}} - \nabla.\,\vec{u}_S\right) \ . \qquad \textbf{Equation Ap. 29}$$

Algebraic equation of the granular temperature (Syamlal M. & O'Brien, 2003)

$$\Theta = \left(-k_1 \varepsilon_s tr(\bar{\bar{D}}_s) + \left[k_1^{2} \varepsilon_s^{2} tr^{2}(\bar{\bar{D}}_s) + 4k_4 \varepsilon_s [k_2 tr^{2}(\bar{\bar{D}}_s) + 2k_3 tr(\bar{\bar{D}}_s^{\ 2})]\right]^{0.5}\right)^{2} / (2k_4 \varepsilon_s)^{2}$$

**Equation Ap. 30**

$$k_1 = 2(1+e_{ss})\rho_s g_{0ss}$$

**Equation Ap. 31**

$$k_2 = \frac{4d_p \rho_s (1+e_{ss}) \varepsilon_s g_{0ss}}{(3\sqrt{\pi})} - \frac{2}{3} k_3$$

**Equation Ap. 32**

$$k_3 = \frac{d_p \rho_s}{2} \left\{ \frac{\sqrt{\pi}}{3(3-e_{ss})} \left[0.5(1+3e_{ss}) + 0.4(1+e_{ss})(3e_{ss}-1)\varepsilon_s g_{0ss}\right] + \frac{8(1+e_{ss})\varepsilon_s g_{0ss}}{(5\sqrt{\pi})} \right\}$$

**Equation Ap. 33**

$$k_4 = \frac{12 d_p \rho_s (1-e_{ss}^{\ 2}) \varepsilon_s g_{0ss}}{(d_p \sqrt{\pi})}$$

**Equation Ap. 34**

$$g_{0ss} = \frac{1}{\varepsilon_s} + \frac{3\ d_{pl}\ d_{pm}}{\varepsilon_s^{2}\ (d_{lp} + d_{pm})} \sum_{\lambda=1}^{M} \frac{\varepsilon_{s\lambda}}{d_{p\lambda}}$$

**Equation Ap. 35**

## Standard drag models

**Table Ap. 3 Governing equations for the existing drag models used for switching procedure**

**O'Brien-Syamlal** Drag Model (Syamlal et al., 1993, and Syamlal and O'Brien, 2003)

$$\beta = \frac{3\,\varepsilon_g\,\varepsilon_s\,\rho_g}{4\,V_{rs}^2\,d_p}\,C_{d0}\left(\frac{Re_p}{V_{rs}}\right)$$ **Equation Ap. 36**

$$V_{rs} = 0.5\left(A - 0.06\,Re_p + \sqrt{(0.06\,Re_p)^2 + 0.12\,Re_p\,(2B-A) + A^2}\right)$$ **Equation Ap. 37**

$$A = \varepsilon_g^{4.14}$$ **Equation Ap. 38**

$$B = \begin{cases} 0.8\,\varepsilon_g^{1.28} & \text{for} \quad \varepsilon_g \le 0.85 \\ \varepsilon_g^{2.65} & \text{for} \quad \varepsilon_g > 0.85 \end{cases}$$ **Equation Ap. 39**

$$C_{d0} = \left(0.63\sqrt{Re_p} + 4.8\right)^2$$ **Equation Ap. 40**

**Gidaspow** Drag Model (Gidaspow (1994))

$$\beta = \begin{cases} 50\,\dfrac{\varepsilon_s^2\,\mu_g}{d_p^2\,\varepsilon_g} + 1.75\,\varepsilon_s\,\dfrac{\rho_g}{d_p}\,|V_g - V_s| & \text{for} \quad \varepsilon_g \le 0.8 \\ 0.75\,C_{d0}\,\dfrac{\varepsilon_s\,\varepsilon_g\,\rho_g}{d_p}\,|V_g - V_s|\,\varepsilon_g^{-2.65} & \text{for} \quad \varepsilon_g > 0.8 \end{cases}$$ **Equation Ap. 41**

$$C_{d0} = \begin{cases} 0.44 & \text{for} \quad Re \ge 1000 \\ \dfrac{24}{Re_p}\left(1 + 0.15\,Re_p^{0.687}\right) & \text{for} \quad Re < 1000 \end{cases}$$ **Equation Ap. 42**

**Wen-Yu** Drag Model (Wen and Yu,1966 and Xu et al., 2012)

$$\beta = 0.75\,C_{d0}\,\frac{\varepsilon_s\,\varepsilon_g\,\rho_g}{d_p}\,|V_g - V_s|\,\varepsilon_g^{-2.65}$$ **Equation Ap. 43**

$$C_{d0} = \begin{cases} 0.44 & \text{for} \quad Re \ge 1000 \\ \dfrac{24}{Re_p}\left(1 + 0.15\,Re_p^{0.687}\right) & \text{for} \quad Re < 1000 \end{cases}$$ **Equation Ap. 44**

## TGS drag model

The TGS drag model was developed by Tenneti and Subramaniam (2011) based on their analysis of the flow around fixed assemblies of particles, obtained from the Immersed Boundary method (IBM). TGS model with its improved correlation for the gas-solid drag force generates more accurate results for the same ranges of the flow Reynolds number and solid volume fraction compared to its succeeding particle resolved-DNS models. Moreover, TGS model extends the accuracy in DNS modeling of the gas-solid flows to include wider ranges of $\varepsilon_S$ and $Re_m$. Theoretically, The TGS model, displayed by Eq. (15), adds two modifications to the single particle-based drag law of Schiller and Naumann (1935), which is displayed by Eq. (16). These terms, defined as $F_{\varepsilon_S}$ and $F_{\varepsilon_S,Re_p}$, include the pure effect of the solid volume fraction (Eq.17), and, the combined effect of the Reynolds number and solid volume fraction (Eq. 18), respectively. The outcome from this model is the exchange coefficient defined by Eq. 19.

$$F(\varepsilon_S, Re_p) = \frac{F_{isol}\left(Re_p\right)}{(1-\varepsilon_S)^3} + F_{\varepsilon_S}(\varepsilon_S) + F_{\varepsilon_S,Re_p}\left(\varepsilon_S, Re_p\right), \qquad \textbf{Equation Ap. 45}$$

$$F_{isol}\left(Re_p\right) = 1 + 0.15\, Re_p^{\,0.687}, \qquad \textbf{Equation Ap. 46}$$

$$F_{\varepsilon_S}(\varepsilon_S) = \frac{5.81\varepsilon_S}{(1-\varepsilon_S)^3} + 0.48\frac{\varepsilon_S^{\,1/3}}{(1-\varepsilon_S)^4}, \qquad \textbf{Equation Ap. 47}$$

$$F_{\varepsilon_S\,,\,Re_p}\left(\varepsilon_S, Re_p\right) = \varepsilon_S^{\,3} Re_p\,(0.95 + \frac{0.61\,\varepsilon_S^{\,1/3}}{(1-\varepsilon_S)^2}), \qquad \textbf{Equation Ap. 48}$$

$$\beta = 18\,\mu_g\,\varepsilon_g\,\varepsilon_S\frac{F(\varepsilon_S\,,\,Re_p)}{d_p^{\,2}}. \qquad \textbf{Equation Ap. 49}$$

## Principle simulation

### Simulation set up

```
DESCRIPTION          = 'fluid bed with jet'
COORDINATES          = 'cylindrical'
Gas-phase Section
  MU_g0              = 1.8E-4            !constant gas viscosity
  RO_g0              = 1.2E-3            !constant gas density
Solids-phase Section
  RO_s               = 2.0               !solids density
  D_p0               = 0.04              !particle diameter
  e                  = 0.8               !restitution coefficient
  Phi                =30.0               !angle of internal friction
  EP_star            = 0.42              !void fraction at minimum
fluidization
Initial Conditions Section ! 1. bed
  IC_X_w(1)          =  0.0              !lower half of the domain
  IC_X_e(1)          =  7.0              ! 0 < x < 7, 0 < y < 50
```

```
  IC_Y_s(1)           =  0.0
  IC                                                !initial values in the region
  IC_EP_g(1)          =  0.42                       !void fraction
  IC_U_g(1)           =  0.0                        !radial gas velocity
  IC_V_g(1)           = 61.7                        !axial gas velocity
  IC_U_s(1,1)         =  0.0                        !radial solids velocity
  IC_V_s(1,1)         =  0.0                        !axial solids velocity
 !  2. Freeboard
  IC_X_w(2)           =   0.0                       !upper half of the domain
  IC_X_e(2)           =   7.0                       ! 0 < x < 7, 50 < y < 100
  IC_Y_s(2)           =  50.0
  IC_Y_n(2)           = 100.0
  IC_EP_g(2)          =   1.0
  IC_U_g(2)           =   0.0
  IC_V_g(2)           =  25.9
  IC_U_s(2,1)         =   0.0
  IC_V_s(2,1)         =   0.0
!  Boundary Conditions Section
! 1. Central jet
  BC_X_w(1)           =  0.0                        !central jet
  BC_X_e(1)           =  1.0                        ! 0 < x < 1, y = 0
  BC_Y_s(1)           =  0.0
  BC_Y_n(1)           =  0.0
  BC_TYPE(1)          = 'MI'                        !specified mass inflow
  BC_EP_g(1)          =  1.0
  BC_U_g(1)           =  0.0
  BC_V_g(1)           =124.6
  BC_P_g(1)           =  0.0
! 2. Distributor flow
  BC_X_w(2)           =  1.0                        !gas distributor plate
  BC_X_e(2)           =  7.0                        ! 1 < x < 7, y = 0
  BC_Y_s(2)           =  0.0
  BC_Y_n(2)           =  0.0
  BC_TYPE(2)          = 'MI'                        !specified mass  inflow
  BC_EP_g(2)          =  1.0
  BC_U_g(2)           =  0.0
  BC_V_g(2)           = 25.9
  BC_P_g(2)           =  0.0
! 3. Exit
  BC_X_w(3)           =   0.0                       !top exit
  BC_X_e(3)           =   7.0                       ! 0 < x < 7, y = 100
  BC_Y_s(3)           =  100.0
  BC_Y_n(3)           =  100.0
  BC_TYPE(3)          =  'PO'                       !specified pressure outflow
  BC_P_g(3)           =  0.0
```

**Domain**

X : -1 :1: 8

8 internal points

$X_{int}$= 0:1:7

2 boundary points (-1 and 8 are on the boundary)

Y : -1:1: 101

101 internal points

$Y_{int}$= 0:1:100

2 boundary point (-1 and 101 are on the boundary)

**Number of internal cells** :
# of internal intervals in the X direction: 7 (internal nodes -1)
# of internal intervals in the Y direction: 100 (internal nodes -1)
# of internal cells : 7x100 =700

**Number of points**
(8+2)x(101+2) =1030

**Number of data points**
number of grid cells = 700
Array for data points (cell centroids)
data points on the X direction : 0.5:1:6.5
data points on the Y direction : 0.5:1:99.5.5

# TFM simulation cases of the standard, PR_DNS, and Hybrid models

## Simulation set up

**Table Ap. 4 Physical and geometrical properties used in the experiment of Hong et al. (2012) and in our simulations**

| Property | symbol | value | unit |
|---|---|---|---|
| Material | | air and FCC | |
| Particle diameter | $d_p$ | 54 | µm |
| Particle density | $Ro_s$ | 930 | $kg/m^3$ |
| Air viscosity | $\mu_g$ | $1.887 {*} 10^{-5}$ | Pa.s |
| Superficial gas velocity | $U_g$ | 1.52 | m/s |
| Solids mass flux | $G_s$ | 14.3 | $kg/(m^2s)$ |
| Single particle terminal velocity | $u_t$ | 0.077 | m/s |
| Minimum fluidization voidage | $\varepsilon_{mf}$ | 0.4 | - |
| Packing limit | $\varepsilon\_s_{max}$ | 0.63 | - |
| Particle-particle coefficient restitution | $e_s$ | 0.9 | - |
| Particle-wall coefficient restitution | $e_w$ | 0.99 | - |
| Specularity coefficient | $\varphi$ | 0.0001 | - |
| Initial solids concentration | $\varepsilon\_s_{init}$ | 0.106 | - |
| Riser diameter | $D_t$ | 0.09 | m |
| Riser height | h | 10.5 | m |
| Overall simulation time | T_stop | 20 | s |
| Grid size, radial × axial | 20×150, 40×300, 60×450 | | |